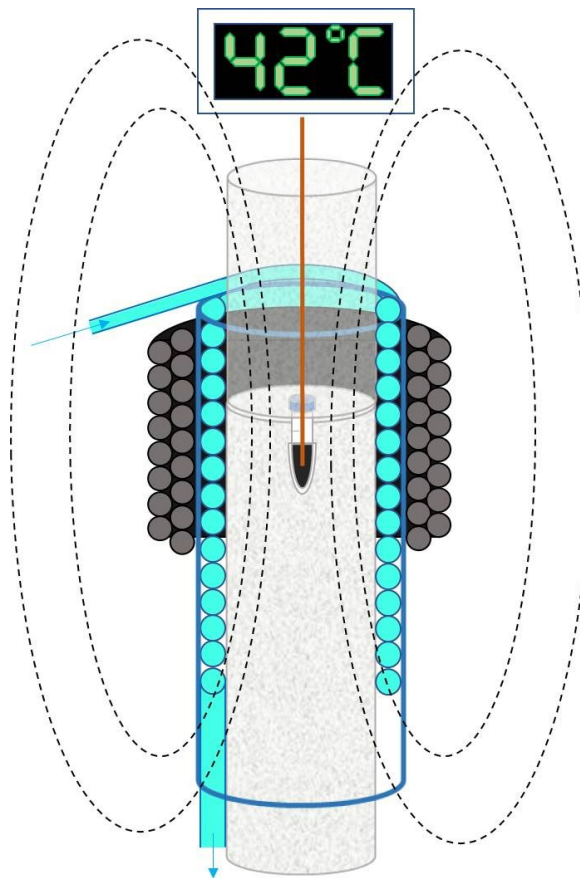# Effects of Iron Oxide Nanoparticles Size and Coating on Hyperthermic Efficiency

Marco Cobianchi

Tesi per il conseguimento del titolo

Full title:
Effects of Iron Oxide Nanoparticles Size and Coating on Hyperthermic Efficiency

Marco Cobianchi

2018

Università degli Studi di Pavia
Dipartimento di Fisica

Università di Pavia

A. Volta

DOTTORATO DI RICERCA IN FISICA – XXX CICLO

Effects of Iron Oxide Nanoparticles Size and Coating on Hyperthermic Efficiency

Marco Cobianchi

Submitted to the Graduate School of Physics in partial

fulfilment of the requirements for the degree of

DOTTORE DI RICERCA IN FISICA

DOCTOR OF PHILOSOPHY IN PHYSICS

at the

University of Pavia

Supervisor: Prof. Maurizio Corti, Prof. Alessandro Lascialfari

Cover: Schematic illustration of hyperthermia setup

Effects of Iron Oxide Nanoparticles Size and Coating on Hyperthermic Efficiency
Marco Cobianchi
PhD thesis - University of Pavia
Pavia, Italy, January 2018

Ho provato, ho fallito.
Non importa, riproverò.
Fallirò ancora.
Fallirò meglio.
Molloy, Samuel Beckett

Contents

Abbreviation	Meaning
NP	Nanoparticles
SP	Superparamagnetism
FM	Ferromagnetism
FiM	Ferrimagnetism
D_c	Critical Diameter
M_s	Magnetic Saturation
H_c	Coercive Field
K_{eff}	Effective Anisotropy Constant
H_{inv}	Inversion Field
E_b	Energy Barrier
τ_0	Attempt Time
τ_N	Néel Relaxation Time
τ_B	Brown Relaxation Time
τ_{eff}	Effective Relaxation Time
TEM	Transmission Electron Microscopy
XRD	X-ray Powder Diffraction
AFM	Atomic Force Microscope
ZFC-FC	Zero field cooled - Field Cooled
MFH	Magnetic Fluid Hyperthermia
SLP	Specific Loss Power
LRT	Linear Response Theory
SWT	Stoner-Wohlfarth Theory
FEM	Free Exponent Model
RMG	Roch-Muller-Gillis

The table describes the significance of various abbreviations and acronyms used throughout the thesis.

Overview

The research about magnetic nanoparticles (NPs) for biomedical applications is nowadays very active: they are applied as drug delivery vehicles [1, 2], for tissue repair [3], cellular therapy [4], as contrast agent for MRI [5, 6, 7, 8, 9] or heating mediators for hyperthermia.

Iron oxides, such as magnetite (Fe_3O_4) or maghemite (Fe_2O_3), are generally used as magnetic core and, in many case, these cores are doped with other metals, like cobalt, nickel or zinc, able to modify their characteristics. However, the pure iron-oxide-based cores are the only ones which have been already approved by US Food and Drug Administration (FDA) and European Medicines Agency (EMA) [10]. In order to reduce the possible toxicity of metals [11, 12] in the human body and allow NPs to bind to particular molecules or markers (e.g. antigen expressed by tumours, peptides), is necessary to coat them with a biocompatible organic moiety.

Hyperthermia therapy is the process of treating cancer with the application of heat to the diseased tissue. Usually this is used in conjunction with other methods of treatment, and, in the form of mild hyperthermia, induces a temperature increase of the cells until 40-43 °C [13], thus generating their death for apoptosis. As isolated therapy, if the temperature is increased above 43 °C and maintained for 30-60 minutes, the heated cells undergo a necrosis, causing shrinkage in tumour size [14]. Usually, the hyperthermia is not strong enough to completely remove the tumour, so it is used in conjunction with classical medical treatments as radiotherapy and chemotherapy [15]. However, for certain types of cancer these methods are very difficult to use because the tumour is located close to vital organs or is drug resistant. In these cases hyperthermia is a good complementary technique. As complementary therapy, the hyperthermia treatment doesn't cause death directly but increase (or add to) the effectiveness of the standard treatments. Chemotherapy drugs kill cells in different ways, depending on type of drug, and consequently hyperthermia may interact with the killing process.

NPs used for tumour treatment ideally must be small enough to pass through the cell membrane barrier, and consequently they should have a diameter 10-100 nm [16]. In this thesis we present an investigation of the hy-

perthermic and relaxometric properties of different nanoparticles, focusing on the physical model of the heat release and related spin dynamics and their possible use in biomedical area. Particularly we focus on the effect of core size and coating on the NMR contrast efficiency (relaxivity) and the heat release (Specific Loss Power).

In the first chapter the physical properties of NPs, in particular the main features of ferromagnetism and superparamagnetism, are reported.

The second chapter contains the heuristic and theoretical models available in literature to study the hyperthermic and relaxometric properties of the NPs; a discussion about their limits of validity is also presented. Since the common models for hyperthermia don't explain the behaviour in the transition zone between small and big NPs, a heuristic model is proposed.

The third chapter is devoted to the effect of the core size on the physical properties of NPs. The morphological characterization (XRD, TEM images, AFM images and size distributions) of the investigated samples together with the magnetic characterization as a function of temperature (ZFC/FC curves) and of the external magnetic field (hysteresis), are presented. The NPs have been investigated for their hyperthermia properties in the frequency range 100-900 kHz and in the magnetic field range 4-17 kA/m; the results were fitted with the models present in literature and with a heuristic model in the transition zone. For NMR profiles, the transverse and longitudinal relaxivities have been recorded over a wide range of frequency, i.e. 10 kHz - 60 MHz, which corresponds to 0.2 mT - 1.5 T for the hydrogen nucleus (protons), in order to investigate the nuclear relaxation mechanisms in presence of magnetic nanoparticles.

In the fourth chapter the effects of different coatings on the release of heat (namely the Specific Loss of Power, SLP) are reported : NPs with the same size and shape have been synthesized and covered with different organic compounds. The coating modifies the SLP and the relaxometric efficiency of NPs, affecting the static and dynamic magnetic properties.

Chapter 1

Ferromagnetism and Superparamagnetism

This chapter introduces the microscopic physical properties of the magnetic nanoparticles that will be analysed in the next chapters. Particular attention will be given to the superparamagnetic and ferromagnetic nanoparticles. The distinction between superparamagnetic and ferromagnetic state plays a fundamental role in the part of the thesis dedicated to the biomedical applications of the NPs.

1.1 Nanomagnetism and Nanoparticles

The behaviour of the magnetic materials is strongly influenced by their microscopic structure, in particular when subjected to an external magnetic field. Diamagnetism, which is always present in the matter, is due to the reaction of the electrons to the external magnetic field and it is manifested by the insurgence of a local field opposite to the external one. Paramagnetism arises from identical, uncoupled atomic moments. Hence, in a paramagnetic material, there is no long range order and the magnetic moments tend to align under an external magnetic field. When the magnetic moments strongly interact spontaneously, a magnetic order occurs. Here below we analyse the different origin of this interaction. The magnetic properties can be understood in terms of the different magnetic couplings that are closely related also to the chemical composition and crystalline structure of the material.

1.1.1 Exchange Interaction

The exchange interaction is generally the dominating term of the system Hamiltonian that allows to create a magnetic order between magnetic moment and usually is the dominant one. We can distinguish two different exchange interactions between moments of nanoparticles: *direct* and *indirect/superexchange*.

5

In the first case the wave functions of atoms are close enough to overlap and the resulting interaction competes with the thermal energy for the reversal of magnetic moments; in the second case the atoms aren't so close to allow an overlap of the wave functions and the orientation is mediated by a nonmagnetic ion that is placed in between the magnetic ions (e.g., oxygen atoms in oxides). The Hamiltonian which describes this interaction, considering a multi-atom system, is the Heisenberg one:

$$H_{exc} = -2 \sum_{ij} J_{ij} \mathbf{s}_i \cdot \mathbf{s}_j \qquad (1.1)$$

where J_{ij} is the exchange integral describing the magnitude of coupling between the spins $\mathbf{s}_i$ and $\mathbf{s}_j$. The exchange integral determines the magnetic behaviour of the system.

For a positive value of J (triplet state favourable) the magnetic moments in a bulk compounds are aligned parallel and the material has a ferromagnetic (FM) nature below a critical temperature, named Curie temperature T_C. If $T > T_C$ the system is in the paramagnetic regime, where the thermal energy becomes higher than the exchange energy and destroys the magnetic order.

If J is negative the spins are antiparallel and the critical temperature is called Néel temperature (T_N): when $T < T_N$ one has an antiferromagnetic system (AFM) with total magnetic moment equal to zero ($\sum_i \mathbf{m}_i = 0$); on the other hand if there isn't compensation between the individual moments ($\sum_i \mathbf{m}_i \neq 0$) the system results ferrimagnetic (FiM). For $T > T_N$ the system is paramagnetic.

1.1.2   MultiDomain Ferromagnetic Order

In order to minimize the internal energy, a system of spins can organize itself in a certain number of small regions, with different sizes and shapes, called domains: these uniform magnetized regions have atomic magnetic moments oriented in the same direction. Each magnetic domain is composed by $10^{12} - 10^{18}$ atoms with a dimension variable between about 0.1 and some tens of μm, depending on the material. The domains are separated by a transition region (*Bloch wall*) where the spins gradually rotate coherently or incoherently from one domain to the other. In an unmagnetized FM or FiM material, magnetic domains have random directions and the sum of the overall domain moments is zero.

In each domain the spins are oriented along a particular axis (*easy axis*) due to the spin-orbit interaction. When an external magnetic field $\mathbf{H}$ is applied, the domains with the orientation along the magnetic field increase and compress the other domains while the spins tend to align with $\mathbf{H}$; as a consequence the magnetization of the system reaches a saturation state when the bigger domains are aligned along the field direction; its value is called magnetic saturation (M_S). In this situation, if the external field is turned off,

unlike what happens in paramagnetic state where magnetization has a linear proportionality with field, the magnetization decreases but for a zero-applied field one observes a residual magnetization (M_R). For zeroing the residual magnetization it is necessary to apply a magnetic field opposite to the initial field called coercive field (H_C). The full curve of M vs H for positive and negative values of H is called hysteresis (see fig. (1.1)).
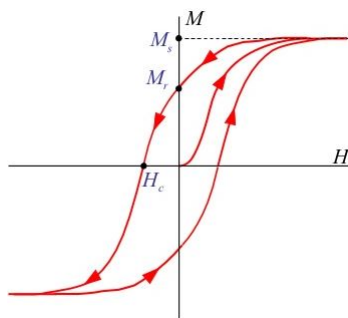

Figure 1.1: Magnetization versus magnetic field curves (M vs H) for ferromagnet.

1.1.3   SingleDomain Ferromagnetic Order

When the dimensions of ideal spherical ferromagnetic nanoparticles are below a specific size (critical radius, r_c), a magnetic multidomain structure is not energetically favourable (the energy needed to create the Bloch domains is higher than the demagnetization energy) and the particles with dimensions below r_c present a single magnetic domain.

The critical radius for a generic nanoparticle can be evaluated by using of the expression:

$$r_c = \frac{0.135\mu\gamma}{M_S^2} \tag{1.2}$$

where μ is a single magnetic moment, γ is the density energy of a single domain wall and M_S is the magnetic saturation.

Typical critical diameter (D_c) values for magnetic iron oxides are ~ 82 nm for $\gamma - Fe_2O_3$, ~ 85 nm for Fe_3O_4 and the values for common materials used in nanomedicine are reported in Table (1.1).

In Fig. (1.2) is reported a diagram that shows the variation of structure for different diameters: when the NP presents a completely closed hysteresis it has a superparamagnetic behaviour. When the hysteresis begins to open, the NP presents a single domain ferromagnetic order but, when the diameter overcomes a critical value, the single domain structure is not energetically favoured and the formation of different domains begins.

A magnetic monodomain nanoparticle can be represented with a single moment (*superspin*) with magnetic moment proportional to its volume and
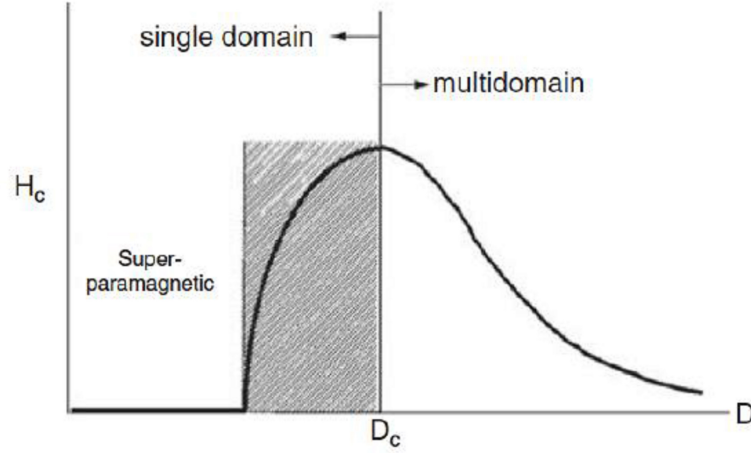
Figure 1.2: Coercive field as a function of the particle diameter. The grey zone represents the single domain ferromagnetic zone: when the coercive field is zero the NP is in the superparamagnetic zone; on the other hand, when the diameter exceeds a critical value, the NP presents a multi domain structure.

to the magnetic saturation value. As explained in next sections, iron oxide nanoparticles are characterized by a strong magnetic anisotropy, due to ions arrangement in the crystalline lattice and to spin-orbit interaction, and, below a certain temperature or above a specific field, the magnetization is oriented along the *easy axis*[17].

The direction of the easy axis and the strength of anisotropy in bulk material is a function of the crystal structure. One has uniaxial anisotropy when there is only one easy axis; this occurs in hexagonal or tetragonal crystals where anisotropy is along the c-axis. Consequently the energy of anisotropy can be expressed as a series of expansions of cosines with the angle θ between the direction of the saturation magnetization and the crystal axes direction.

The form of the energy equation is normally converted to use sines, as in eq. (1.3):

$$E_{uniaxial} = K_0 + K_1 \sin^2(\theta) + K_2 \sin^4(\theta) + ... \tag{1.3}$$

The important information for reversal is the change in energy with angle, and as K_0 is not dependent on the angle it can be neglected. When K_1 and K_2 are both positive the energy minimum is located at $\theta=0$ and the easy axis lies along the c-axis [18]. The K_2 term, as it is multiplied by the fourth power of $\sin\theta$, is often so small that it can be neglected.

Cubic anisotropic materials usually have easy axes along the [100] and other symmetric directions. The energy can be written as:

Sample	D_{SPM} (nm)	D_{FM} (nm)
$CoFe_2O_4$	10	100
Fe_2O_3	30	82
Fe_3O_4	28	85
$FeCo$	15	50
$FePt$	7	52
$CoPt$	5	55
Ni	30	85
Co	10	80

Table 1.1: Critical diameters for superparamagnetic and ferromagnetic structures for different classes of nanoparticles.

$$E_{cubic} = K_0 + K_1(\alpha_1^2\alpha_2^2 + \alpha_2^2\alpha_3^2 + \alpha_3^2\alpha_1^2) + K_2(\alpha_1^2\alpha_2^2\alpha_3^2) + ... \qquad (1.4)$$

In eq. (1.4) α_1, α_2 and α_3 are the cosines of the three angles that the direction of magnetization forms with the crystal axes a, b and c.

For a uniaxial approximation nanoparticles the most used expression is:

$$E(\theta) = K_{eff}V\sin^2\theta \qquad (1.5)$$

where K_{eff} is the effective anisotropy constant (energy density per volume unity), V is the volume of magnetic core of nanoparticles and θ is the angle between the magnetization vector and the anisotropy axis. When the magnetization forms an angle with the anisotropy axis equal to zero or π, the nanoparticle is in an equilibrium configuration, the two distinct states are separated by energy barrier $E_b = K_{eff}V$ and the system is in a blocked regime [19].

The application of an external magnetic field modifies the eq. (1.5) and then the energy barrier. If we call δ the angle between magnetic field and the anisotropy axis the equation becomes:

$$E_b(\theta, \delta, \phi) = K_{eff}V\sin^2\theta - HM \cdot (\cos\theta\cos\delta + \sin\theta\sin\delta\cos\phi) \qquad (1.6)$$

where M and ϕ are respectively the modulus and the third spherical coordinate of the magnetization vector [19]. The minimum value of eq. (1.6) is reached when M is at an angle equal to $\delta - \theta$ with respect to the field H (Fig. 1.3).

Therefore the energy barrier depends on mutual orientation of H and the easy axis: when $\delta = 0$ the energy separation between the two equilibrium states is given by:
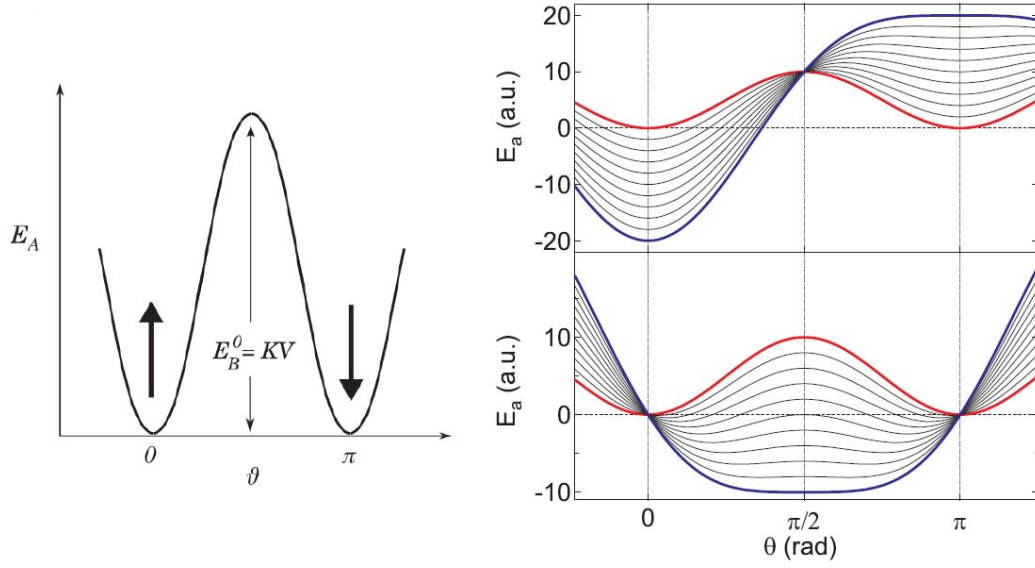
Figure 1.3: Anisotropy energy versus θ, the angle between the anisotropy axis and the magnetization in the case of uniaxial anisotropy (left). The two minima correspond to the two possible configuration of the magnetization along the anisotropy axis. The right figure represents the angular dependence of the anisotropy energy in the case of applied magnetic field parallel (top) and perpendicular (bottom) to the easy-axis. Red and blue thick lines correspond to H = 0 and H = H_{inv} field values, where H_{inv} is the inversion field.

$$E_b = K_{eff} V \left(1 - \frac{H}{H_k} \right)^{\beta} \tag{1.7}$$

which represents a phenomenological expression where β is a phenomenologic constant depending to δ. At $T = 0$ for $H = H_k$ the energy barrier vanishes and the magnetization inverts its orientation.

Below a specific temperature value, called blocking temperature (see next section), the particle's moment is blocked and unable to overcome the barrier in the time of a measurement; the system preserves a ferromagnetic behaviour and an open hysteresis is observed. The height of the energy barrier can be written as:

$$E_b = K_{eff} \left(1 \pm \frac{H}{H_k} \right)^2 \quad where \quad H_k = \frac{2K_{eff}}{M_S} \tag{1.8}$$

Many characteristics of nanoparticles can affect the constant K_{eff}. The sources of anisotropy are summarized below.

Shape Anisotropy

The shape anisotropy is due to the presence of free magnetic poles on the surface of a magnetized body: they generate a demagnetizing field in the nanoparticle which is responsible for an additional contribution to the magnetostatic energy. For an asymmetric structural shape of the nanoparticles there is only one predominant direction (where the energy of the demagnetizing field is low) for the magnetization and one or more secondary directions (*hard axis*, where magnetizing field energy is high)[20]. The anisotropy constant can be written as:

$$K_s = \frac{1}{2}M_S^2(N_c - N_a) \tag{1.9}$$

where N_c and N_a are the intensity of the demagnetizing field along major (c) and minor (a) axis of the nanoparticle. When the ratio $c/a > 1.1$ the shape anisotropy dominates on the crystalline anisotropy[21, 22, 23].

Surface Anisotropy

The surface anisotropy is strictly related to the chemical and/or physical interactions between surface atoms and other chemical species. The coating and functionalization of the nanoparticle surface can induce important modifications in its magnetic properties, which are mainly due to the surface spin canting induced by the coating ligands. Both surface and bulk anisotropy give a contribution to K_{eff}: when the ratio surface-volume increases the surface anisotropy becomes important over bulk anisotropy. For a spherical nanoparticle the total anisotropy is:

$$K_{eff} = K_B + \frac{6}{d}K_s \tag{1.10}$$

where K_B is the bulk anisotropy, K_s is the surface anisotropy and d the diameter [24].

1.1.4   Stoner-Wohlfarth Model and Spin Relaxation

From (1.7) H_k is the minimum field needed to invert the magnetization direction. When $H > H_k$ the hysteresis loop of the nanoparticles depends on the angle δ between field and anisotropy axis: this condition is explained by the Stoner-Wohlfarth model. In order to evaluate the angle δ for the minimum energy configurations we should equal to zero the double derivative of eq. (1.6) with respect to δ. The equation has analytical results only when $\delta = 0$ and $\delta = \pi/2$. When the magnetic field is parallel to easy axis the hysteresis is closed (as a paramagnetic material), when $H \perp$ at easy axis the hysteresis has a squared (open) shape.

In the intermediate cases, for $0 < \delta < \pi/2$, hysteresis cycles feature a coercive field and residual magnetization that are between these two extreme

positions. Also, for an assembly of randomly oriented non interacting particles all the discontinuities in the hysteresis curve are smoothed out.

The original model assumes only a uniaxial anisotropy structure for the nanoparticles; however in the real systems the anisotropy is a sum of all the sources explained in the previous section, i.e. shape, magnetocrystalline and surface. A new model, including all nanoparticles anisotropy variables, was proposed in 1998 by Thiaville [25, 26]. The initial hypothesis is the superspin arrangement in the system, where all spins are coupled by the exchange interaction, a situation described by the unit vector $\mathbf{m}$; and the potential energy is:

$$E_0(\mathbf{m}, \mathbf{H}) = E_0(\mathbf{m}) - V M_s \mathbf{m} \cdot \mathbf{H} \tag{1.11}$$

where V is the nanoparticle volume, M_s is the magnetic saturation and H the magnetic field. $E_0(\mathbf{m})$ is a sum of different anisotropy energies given by [19]:

$$E_0(\mathbf{m}, \mathbf{H}) = E_{shape}(\mathbf{m}) + E_{magnetocry}(\mathbf{m}) + E_{surf}(\mathbf{m}) \tag{1.12}$$

1.1.5 Superparamagnetism

As explained in the section (1.2) the magnetization vector $\mathbf{M}$ is oriented along a particular axis due to intrinsic properties of the nanoparticles. This condition can be considered true when the energy barrier $E_b = K_{eff}V$ is higher than the thermal energy $k_B T$; on the other hand, when $E_b < k_b T$ the thermal energy is enough to allow the magnetization to overcome the anisotropy barrier. For an ensemble of nanoparticles where this condition is valid, the total magnetization at $H = 0$ is zero because the orientation of the magnetization of each particle is random: considering the magnetization the system is *superparamagnetic*. The superparamagnetic system is characterized by a closed hysteresis (coercive field $H_c = 0$), as a paramagnetic one, but with a higher magnetization at the same field.

If we consider an ideal system, where the nanoparticles are non-interacting, the characteristic reversal time is the Néel time and is given by the Arrenius expression:

$$\tau_N = \tau_0 \exp\left(\frac{E_b}{k_B T}\right) \tag{1.13}$$

where τ_0 is an attempt time that depends on several parameters, like temperature, gyromagnetic ratio, saturation magnetization, energy barrier and direction of the applied field. The attempt time, in most cases, is assumed constant in the range $10^{-12} \div 10^{-9} s$, but its value depends on the energy barrier $E_b = KV$ and M_S by the expression:

$$\tau_0(E_b) = \frac{\sqrt{\pi}}{4} \frac{M_S(0)V}{E_b \gamma_S} \left[\frac{1}{\eta_f} + \eta_f \left(\frac{M_S(T)}{M_S(0)} \right)^2 \right] \sqrt{\frac{k_B T}{E_b}} \left(1 + \frac{k_B T}{E_b} \right) \qquad (1.14)$$

where V is the volume of magnetic core, $M_S(0)$ is the magnetic saturation at 0 K, $M_S(T)$ at room temperature, γ_S the gyromagnetic ratio of electron and η_f is a dimensionless constant, equal to $\eta_f = \eta \gamma_S M_S(0)$ (η the damping constant [27]).

In $E_b \ll k_B T$ case, the exponential term of eq. (1.13) tends to 1 and so the relaxation time is due only to τ_0. On the other hand, if $E_b \gg k_B T$ the exponential term becomes dominant and the result is a competition between the exponential (that increase with E_b) and τ_0 (it is inversely proportional to energy barrier).

When the interactions between nanoparticles aren't negligible, for example when in the sample the concentration is very high, they modify the physical behaviour of the system. The most relevant interaction are:

(I) Dipolar-Dipolar Interaction

Interparticle interactions can be due to dipole-dipole interactions between nanoparticles. When a coated surfactant is used, the increased spacing between particles results in negligible exchange interactions and thus the primary interaction is considered from the dipole-dipole coupling.

(II) Exchange Interaction

As already cited the exchange interaction is an effect due to the electronic orbitals superposition. When the electrons on neighbouring magnetic atoms inside the nanoparticles undergo exchange interaction, one has a direct exchange.

(III) RKKY Interaction

The RKKY (Rudermann-Kittel-Kasuya-Yosida) is an indirect exchange that couples moments over relatively large distances though the moment of the conduction electrons. It is the dominant exchange interaction in metals where there is little or no direct overlap between neighbouring (magnetic) electrons.

In all these cases the previous expressions for the relaxation time are not correct and eq. (1.13) is heuristically modified introducing the phenomenological quantity T_0:

$$\tau_N = \tau_0 \exp \left(\frac{E_b}{k_B (T - T_0)} \right) \qquad (1.15)$$

This equation is the Vogel-Fulcher equation. When τ_N from (1.13) or (1.15) is comparable with the measuring time τ_m, the magnetizations of the nanoparticles appears blocked parallel or antiparallel to the external magnetic field with respect to the measurements time of the specific "probe" used. The critical temperature separating the superparamagnetic and blocked states is defined as the temperature where $\tau_N = \tau_m$ given by (blocking temperature):

$$T_B = \frac{E_b}{k_B \ln(\frac{\tau_m}{\tau_0})} \tag{1.16}$$

This equation is valid for individual particles or for a system of non-interacting particles with the same size and anisotropy, and assuming the basic Stoner-Wohlfarth theory (all spins of nanoparticles rotate coherently below T_B). The measuring frequencies for the common techniques are: $10^{-8} - 10^{-3}$ s for NMR, $10^{-10} - 10^{-7}$ s for Mössbauer spectroscopy and $10^{-5} - 10^{-1}$ s for AC susceptibility. The blocking temperature is proportional to the volume of the nanoparticle and decreases when the external magnetic field increases:

$$T_B(H) = T_B(0)\left(1 - \frac{H}{H_c}\right)^k \tag{1.17}$$

where $T_B(0)$ is the blocking temperature at zero field, k is 2 for low field ($H < H_C$) and 2/3 at high field ($H > H_C$).

The magnetization of superparamagnetic particles is given by the same expression valid for paramagnets. The Langevin $L(x)$ function (eq. (1.18)) treats the particle's magnetization through an integral over the energy of all individual magnetic moments, which are in thermal equilibrium with an energy distribution given by Boltzmann law.

$$L(x) = \left(\coth(x) - \frac{1}{x}\right) = \left[\coth\left(\frac{\mu H}{k_B T}\right) - \frac{k_B T}{\mu H}\right] \tag{1.18}$$

It has been shown (eq. (1.6)) that the energy barrier depends on the applied field, the volume and the anisotropy constant; so the distribution of energy barriers is a complex function. Figure 1.4 shows the shape of the distribution function. The following equation describes the three regions of the energy distribution $f(\Delta E)$ [28].

$$\int_{\Delta E_c(H_c)}^{\infty} f(\Delta E)d(\Delta E) = \int_0^{\Delta E_c(0)} L(x)f(\Delta E)d(\Delta E) + \int_{\Delta E_c(0)}^{\Delta E_c H_c} f(\Delta E)d(\Delta E) \tag{1.19}$$

Each value of ΔE has an exponential decay. The time dependence of M is given by the energy barrier ΔE_c which is active for the chosen measuring time, but many discrete values of ΔE (around ΔE_c) contribute as well.

The other dominant mechanism of magnetization relaxation is the Brownian rotation, that occurs when particles are in a fluid (physical rotation of
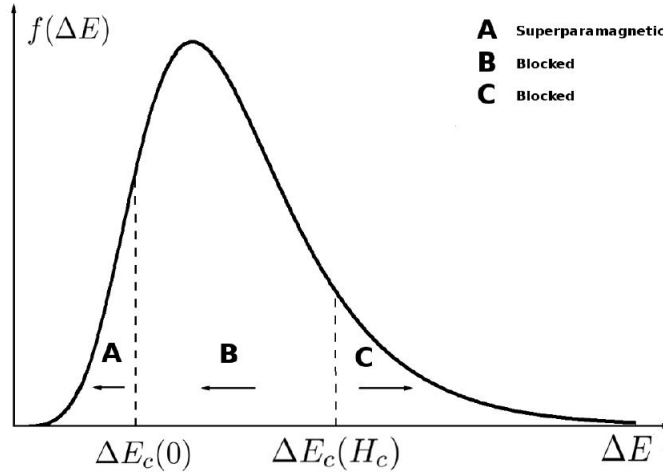
Figure 1.4: The distribution of energy barriers.

the particles). The Brownian process depends on the hydrodynamic properties of the fluid, while τ_N for the Néel process is determined by the magnetic anisotropy energy of the superparamagnetic particles. As concerns the Brownian relaxation mechanism, if a suspension of magnetic particles with viscosity η is considered, the characteristic relaxation time is given by:

$$\tau_B = \frac{3V_H \eta}{k_B T} \tag{1.20}$$

where V_H is the hydrodynamic volume. As model for the hydrodynamic volume is assumed:

$$V_H = \left(1 + \frac{\delta}{r}\right)^2 V_M \tag{1.21}$$

where r is the radius of particle, V_M the magnetic volume ($V_M = 4\pi r^3/3$) and δ the thickness of the surfactant layer [29]. In the general case, the faster relaxation mechanism is the dominant one and the effective relaxation time τ_{eff} is given by:

$$\frac{1}{\tau_{eff}} = \frac{1}{\tau_N} + \frac{1}{\tau_B} \tag{1.22}$$

In Fig. (1.5) the behaviour of τ_{eff} as a function of the particle radius is displayed. At high values of the particle radius R τ_B dominates, while for $R < 7$ nm the Néel mechanism is predominant.

1.1.6   NPs magnetization

In the previous paragraphs we have introduced two fundamental parameters which allow to characterize the nanoparticles: the blocking temperature and
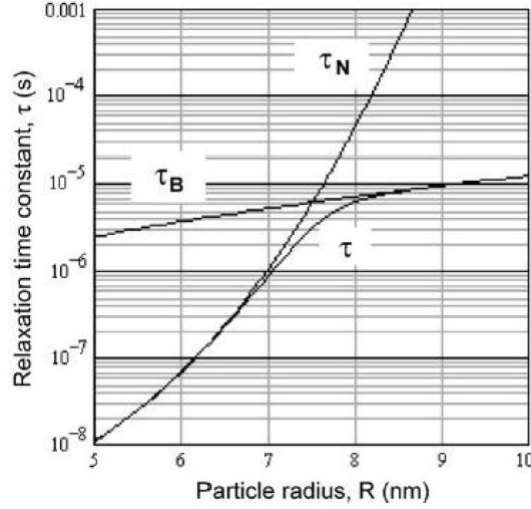
Figure 1.5: Contribution of the Néel and Brown relaxation times. The particles considered are magnetite particles in water medium. The crossover between Néel and Brownian regimes of relaxation occurs at 7.5 nm.

the anisotropy constant. The equation used to describe them are simplified because the rigorous ones are complicated by the number of relationships between the parameters that come into play when a magnetic measurement is performed. These are the following:

- The blocking temperature and the temperature of the ZFC peak (T_{max}), proportional to K_{eff} and V.

- The width of the ZFC peak which increases linearly with T_{max} and T_B and is then proportional to both K_{eff} and V.

- The amplitude of the ZFC peak which is proportional to V and inversely proportional to K_{eff}.

- the initial moment $M_{ZFC}(0)$ which is proportional to V and inversely proportional to K_{eff}

A quantitative estimation of these parameters can be obtained through the analysis of the magnetic curves based on the assumption that the magnetic moment at temperature T follows this approximate expression [30]:

$$M_{ZFC}(T) = M_b \exp(-\nu \Delta t) + M_{eq}[1 - \exp(-\nu \Delta t)] \qquad (1.23)$$

Where ν is the macrospin relaxation frequency of the nanoparticles at temperature T, Δt is the effective measurement time related to the temperature sweeping rate selected for the experimental acquisition, M_b is the magnetization in the blocked regime (low temperature) and M_{eq} the magnetization in superparamagnetic regime (high temperature). M_b and M_{eq} are given by:

$$M_b = \frac{\mu_0 H M_S^2 V}{3K_{eff}} \quad M_{eq} = \frac{\mu_0 H M_S^2 V^2}{3k_B T} \tag{1.24}$$

The model shown in eq. (1.23), as previously cited, is an approximation: a real sample presents a distribution of sizes and the separation between ferromagnetic and superparamagnetic state is not so clear. In order to extend (1.23) one needs to introduce a limit volume V_{lim}: for $V < V_{lim}$ the particles are blocked, conversely they are in the superparamagnetic state. The equation for limit volume is:

$$V_{lim} = \frac{\gamma k_B T}{K_{eff}} \quad \gamma \simeq 0.9609 \ln\left(\frac{\nu_0 T}{\nu_\Gamma}\right) \tag{1.25}$$

with ν_0 attempt frequency and $\nu_{\Gamma is}$ experimental temperature sweeping rate.

Taking into account the separation between states and the volume limit, eq. (1.23) can be written as:

$$M_{ZFC} = \frac{\mu_0 H M_S^2 V}{3K_{eff}} \int_0^{V_{lim}} V^2 \rho(V) dV + \frac{\mu_0 H M_S^2 V^2}{3k_B T} \int_{V_{lim}}^\infty V \rho(V) dV \tag{1.26}$$

From the expression of the energy barrier ($E_b = K_{eff} V$) the above equation becomes:

$$M_{ZFC} = \frac{\mu_0 H M_S^2 V}{3K_{eff}} \left(\frac{1}{T} \int_0^{E_{lim}} E_b^2 \rho(E_b) dE_b + \int_{E_{lim}}^\infty E_b \rho(E_b) dE_b \right) \tag{1.27}$$

The applicability condition is satisfied when the measurements are performed at low field, i.e. the ZFC curves collected at $H = 50 Oe$ or lower fields.

1.1.7 Maghemite ($\gamma - Fe_2O_3$) and Magnetite (Fe_3O_4) nanoparticles

Magnetite has a cubic crystal structure with the space group of Fd3m [31]. The unit cell is made up of eight cubic units with a lattice d-spacing of 8.396 Å. It contains 56 atoms, including 32 oxygen atoms, 16 Fe^{3+} and 8 Fe^{2+} and may be denoted as $(Fe^{3+})_8^{tetr}[Fe^{3+}Fe^{2+}]_8^{oct}O_{32}$. In its unit cell the oxygen anions form a closed-packed FCC lattice. There are also 32 octahedral (B site) and 64 tetrahedral (A site) sites in the unit cell. The Fe^{2+} cations occupy 1/4 of the octahedral interstitial sites (i.e. 8 Fe^{2+}) and Fe^{3+} 1/4 of the octahedral (i.e. 8 Fe^{3+}) and 1/8 of the tetrahedral (i.e. 8 Fe^{3+}) sites. This crystallographic configuration is denoted inverse spinel. From the magnetic moment configuration point of view, magnetite is classified as ferrimagnetic materials. The orbitals are split into two subsets due to the influence of oxide ligands, implying that

all Fe^{3+} and Fe^{2+} ions have five and four unpaired electrons, respectively. As can be seen, in the octahedral coordination, Fe^{3+} and Fe^{2+} ions are coupled ferromagnetically through a so-called double exchange mechanism. The electron whose spin is directed in the opposite direction with respect to the others and coloured red, can be exchanged between two octahedral coordination. On the other hand, the Fe^{3+} ions in tetrahedral and octahedral sites are coupled antiferromagnetically via the oxygen atom, implying that the Fe^{3+} spins cancel out each other and thus merely unpaired spins of Fe^{2+} in octahedral coordination contribute to the magnetization. This magnetic moment configuration accounts for the ferrimagnetism seen in magnetite. Maghemite, likewise magnetite, has a cubic crystal structure with the lattice d-spacing of 8.33 Å. As it can be deduced from its chemical formula $\gamma - Fe_2O_3$, there are only Fe^{3+} cations which are arbitrarily distributed in 16 octahedral and 8 tetrahedral interstitial sites in the FCC packing of oxygen anions. The Fe^{2+} cation vacancies are located in the octahedral sites and their arrangement in the maghemite structure plays a preponderant role in the magnetic response of maghemite. When the vacancies are randomly distributed, its space group is Fd3m and its formula unit may be written as $(Fe^{3+})_8^{tetr}[Fe^{3+}Fe^{2+}]_8^{oct}O_{32}$. The described crystal arrangement is known as normal spinel. Since the spins in the octrahedral and tetrahedral sites are oriented anti-parallel, maghemite is ferrimagnetic. The magnetic response of an ensemble of maghemite/magnetite NPs is a combination of surface effects, finite size effects (i.e.truncation of the magnetic correlation length), and collective behaviour due to interparticle dipolar and/or exchange interactions. The primary exchange mechanism in ferrite compounds is an antiferromagnetic super-exchange interaction between metal cations mediated by an intervening oxygen ion. Because of the indirect nature of the coupling, the super-exchange interaction is sensitive to modified bond lengths, angles at a surface, and a variation in coordination of surface cations produces a distribution of net exchange fields [32].
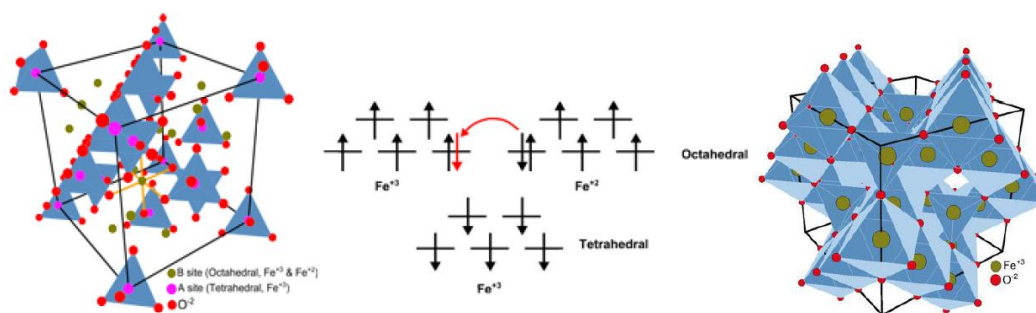

Figure 1.6: Crystalline structure of magnetite (a) and (b) electronic configuration of maghemite; (c) crystalline structure of maghemite.

Chapter 2

Techniques and Models

In this chapter the models and the techniques which were used to analyse the data sets of Maghemite nanoparticles are reported. The thesis in fact is focused on the possible use of magnetic nanoparticles in medical area, as mediator for Magnetic Fluid Hyperthermia (MFH) and for contrast agent in MRI. The hyperthermia is a tumoral therapy, developed in the last 20 years, which takes advantage of alternating magnetic field to produce heat by means of NPs. The great advantage of this technique, if compared to standard anti-tumoral therapy as chemo and radio therapy, is the very well localized effects generated from NPs: the heat (and then the induced cells apoptosis) is released only in the tissues where they are injected. This fact enables to operate only in the unhealthy areas.

In combination to hyperthermia, the MNPs are developed to improve the image contrast by altering the dynamic properties of the water hydrogen nuclei used for acquiring MRI images as diagnostic tool for studying disease of human tissues and organs. The most common NPs currently utilized present characteristics that fit well with MFH, in particular the high biocompatibility of the shell (composed of a sugar or a polymer, for instance) and a very high magnetization; the synthesis route can be adjusted to obtain very small nanocrystals, with controllable shape and dispersive index. The combination of the two effects (heat and contrast), allows to have multi-functional nanoparticles to be applied for diagnostic and therapy (theranostics) [33, 34, 35].

2.1 Magnetic Fluid Hyperthermia

Many types of therapies that are used to treat cancer, like chemotherapy, radiotherapy and hyperthermia, cause damage to cancer cells that results in cell death. Therefore, the combination of treatments to achieve a complementary and synergistic effect is often used in clinics, as e.g. radiotherapy in combination with hyperthermia. Hyperthermia is defined as a temperature increase by several degrees above the normal physiological level. The effectiveness of

19

hyperthermia, i.e. the amount of cell death, depends both on the temperature and the duration of the temperature increase as well as on the susceptibility of cells to undergo apoptosis, determined by endogenous factors.

As introduced in Chapter 1, the physical mechanism of spin reversal is dependent on the particle volume V, but it is not known "a priori" which mechanism is characteristic of any particle of specific size. It can be shown that the spin dynamics is responsible for the heat release. In this chapter the theory behind the heat release is illustrated.

2.1.1 Specific Loss of Power (SLP)

From a thermodynamic point of view, an ensemble of nanoparticles in an alternating magnetic field has an internal energy $dU = HdB$, where H is the magnetic field and B is the magnetic induction. This is the starting point to obtain the power dissipated by the sample for each cycle of magnetic field at a certain field frequency:

$$P = f \cdot \mu_0 \oint MdH \tag{2.1}$$

where the integral gives the internal energy per cycle. The SLP is expressed as the dissipated power (A_{hyst}, the area of hysteresis loop) multiplies by frequency of the field f divided by the concentration (ρ) of the nanoparticles and it can be written as:

$$P = \frac{A_{hyst}f}{\rho} \tag{2.2}$$

From equation (2.2) is clear that the SLP depends to experimental conditions, in particular on frequency and intensity of the magnetic field. To compare the heat release efficiency of nanoparticles a standard parameter named Intrinsic Loss Power (ILP), which normalize the Specific Loss Power (SLP) per frequency and square of magnetic field is introduced:

$$ILP = \frac{SLP}{fH^2} \tag{2.3}$$

To extract the values of SLP from increments of temperature we can use two methods depending on the value of temperature increase: the differential method or the Box-Lucas fitting method.

Differential Method

This is the best method when the temperature increment, generated by energy dissipation, is relatively high (over 5° in five minutes)[36]. Introducing the volume fraction of the ferrofluid $\phi = V_{MNP}/V_f$ (where V_{MNP} is the maghemite volume and V_f the volume of the ferrofluid) we can write the energy conservation as:

$$\frac{P\phi}{\rho_f} - \frac{q}{\rho_f V_f} = \frac{\Delta T}{\Delta t} c_f \tag{2.4}$$

where q is the heat exchanged with the environment, ρ_f the density of ferrofluid, c_f its specific heat and $\Delta T/\Delta t$ is the temperature increment in function of time. At zero time the value q is negligible because the vial and ferrofluid are in thermal equilibrium with environment. If we divide the right side of eq. (2.4) by the mass fraction of the nanoparticles (m_{MNP}) in the sample, we obtain the SLP value:

$$SLP = \left.\frac{\Delta T}{\Delta t}\right|_{t=0} \frac{c_f}{m_{MNP}} \tag{2.5}$$

The specific heat of the ferrofluid is a combination of the specific heat of all the different parts of the sample:

$$c_f = \frac{M_{MNP}c_{MNP} + M_{H_2O}c_{H_2O}}{\rho_f V_f} \tag{2.6}$$

Box-Lucas Fitting

This model is useful when the measurement time is long and the temperature increment is not so high. The Box-Lucas curve has the formula [37]:

$$y(T) = \frac{B}{A}(1 - \exp^{-Ax}) + C \tag{2.7}$$

where A describes heat exchange with the surrounding environment, B the heat produced by nanoparticles and C the starting temperature. The parameter of interest is B and measurements of this type are performed in a range of time between 5 and 10 minutes or more.

2.1.2 Rayleigh Model

For dimensions of nanoparticles over the critical diameter, a multi-domain structure is observed: in this condition the energy losses are due to the motion of the Weiss domains and were described by Rayleigh [38]. Obviously, for a single domain ferromagnetic particles, the energy release can't be interpreted with domain motion; however Hergt *et al* [39] discovered a similar mechanism that starts when the diameter is around the critical value. During this transition the nanoparticles create a particular spin state, named *vortex state*, where the particle has a pseudo-single domain behaviour.

Hergt proposed a semi-empirical approach where the area of hysteresis is strongly related to the applied field:

$$A = \alpha D H^3 \quad if \quad H \leq H^3 \tag{2.8}$$

where α is the friction parameter and D the core diameter. Therefore the SLP is strongly related, for ferromagnetic particles, to the diameter and the applied field (as report in Fig. (2.1)). As one can see in Fig. 2.1, in the superparamagnetic state ($D < 20$nm) the losses are very low and increase when the dimension increases, with a maximum exactly in the middle of the transition zone.
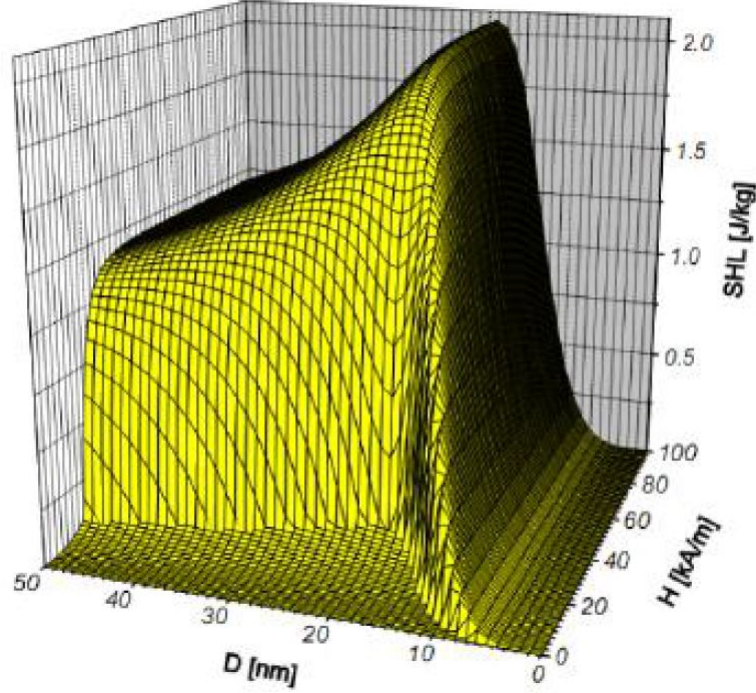

Figure 2.1: Specific Heat Loss (SHL, equivalent to SLP) dependence from NPs core diameter and applied field.

2.1.3 Linear Response Theory Model

As introduced in Chapter 1, the application of an external field (see equation (1.6)) introduces a correlation between anisotropy axes, direction of magnetization and magnetic field. The starting model for analytical description is the Stoner-Wohlfarth (SWT) and, when the magnetic field is aligned along to the easy axis the hysteresis loop presents a rectangular shape with area:

$$A = 4\mu_0 H_C M_S = 4\mu_0 H_K M_S = 8K_{eff} \tag{2.9}$$

The above equation is obtained by considering that $H_C = H_K$ for $\delta = 0$. When δ increases from 0 the hysteresis tends to decrease till it disappears when $\delta = \pi$. In a real system the easy axis is randomly oriented in the fluid and the M_S results one-half compared to perfect case ($H_0 \parallel easyaxis$) with the coercive field equal to $0.48H_K$. As conclusion, the area of hysteresis becomes:

$$A = 4\mu_0(0.48H_K)(0.5M_S) = 1.92K_{eff} \tag{2.10}$$

When the dimension of the nanoparticle decreases, the thermal energy allows the magnetization to overcome the barrier ($KV \sim k_BT$); similarly, when the temperature of the system increases we can have the transition to the superparamagnetism with coercive field results equal to 0. A constant κ was introduced by Usov [40] to describe the variation of coercive field:

$$\kappa = \frac{k_BT}{K_{eff}V} \ln\left(\frac{k_BT}{4\mu_0 H_{max} M_S V f \tau_0}\right) \tag{2.11}$$

where H_{max} is the maximum applied field and τ_0 the attempt time.

Nowadays, a general tendency in the hyperthermia studies considers two type of relaxation mechanisms: the loss via Néel relaxation (in the superparamagnetic regime, with the *Linear Response Theory*, LRT) and the losses via hysteresis (in the ferromagnetic state). This subdivision was criticized by Carrey [41]: he asserts that all the losses are due to hysteresis, the problem is just the simulation of its shape.

The LRT is a good model which allows to evaluate the area of hysteresis when the magnetization response is linear with the field; the ellipsoidal area can be written as:

$$A = \pi H_{max}^2 \chi_0 \frac{\omega\tau_{eff}}{1 + \omega^2\tau_{eff}^2} \tag{2.12}$$

where ω is the system frequency multiplied by 2π and τ_{eff} is the effective relaxation time of nanoparticles. χ_0 is the static susceptibility which, for particles with low anisotropy (or easy axis along the field), is given by Langevin expression:

$$\chi_0 = \frac{\mu_0 M_S^2 V}{3k_BT} \tag{2.13}$$

For particles with high anisotropy (or with easy axis oriented randomly) χ_0 must be divided by a factor 3 and more generally, for particles randomly oriented as the usual cases, the area is:

$$A = \frac{\pi\mu_0 H_{max}^2 M_S^2 V}{3k_BT} \frac{\omega\tau_{eff}}{(1 + \omega^2\tau_{eff}^2)} \tag{2.14}$$

This value of hysteresis can be inserted into eq. (2.2) to obtain the SLP value. The problem about the LRT model is to establish when it can be used. For this purpose it was introduced the constant ξ which, with κ, places the limit for the LRT model. ξ is given by:

$$\xi = \frac{\mu_0 M_S V H_{max}}{k_BT} \tag{2.15}$$

In Fig. (2.2) the different zones for the validity of the different models are summarized. As one can see in Fig. (2.2), the formal transition between the superparamagnetic regime ($\omega\tau_N < 1$) and the ferromagnetic regime ($\omega\tau_N > 1$) occurs at $\omega\tau_N = 1$. For this condition, the hysteresis loop area for small magnetic fields displays a maximum. However, the coercive field starts to grow well before the transition and it increases again after the transition. This means that the area of the hysteresis loop at high magnetic fields does not display a maximum but continues to increase with increasing the volume.

When $\omega\tau_N > 1$ the hysteresis continues to increase with volume. In the ferromagnetic regime the Stoner-Wolhfarth is the most suitable model to describe the nanoparticles hysteresis loops if they are not closed in the transition zone ($\kappa < 0.7$). The model can be used (if $\mu_0 H_{max} > 2\mu_0 H_C$) in the random orientation case. If the last condition is not respected, the LRT is still valid in this region and can be used to calculate the minor hysteresis loop area at very low fields.

In larger MNPs, incoherent reversal modes start to occur, which lead to a decrease of the coercive field. This is why for large MNPs the LRT model is not good to explain the SLP behaviour.

The large MNPs are composed of a vortex [42] or of several magnetic domains separated by magnetic walls. In this last mentioned case, the process leading to their magnetization is the growth of one or several domains in the direction of the field at the expense of the others. As a consequence, their hysteresis loops at very small magnetic fields are described by "Rayleigh loops" (SLP proportional to H^3)[43].
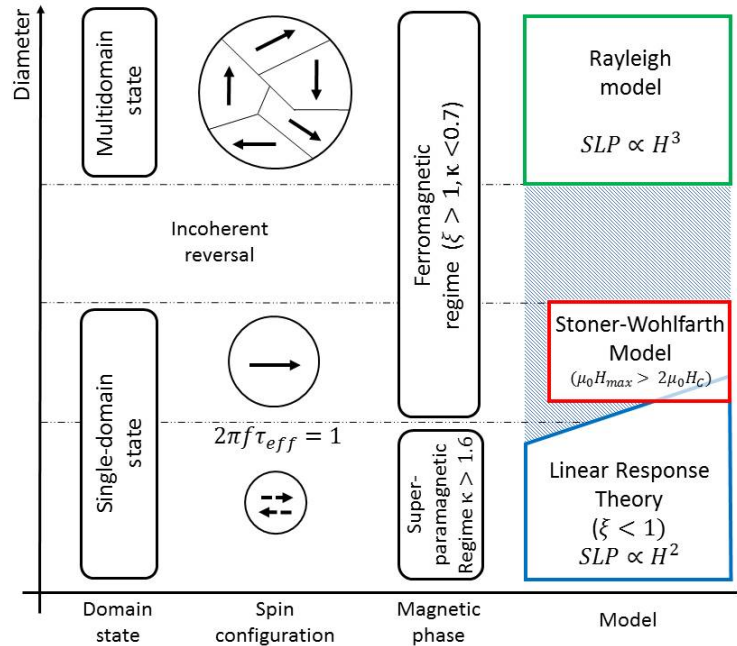

Figure 2.2: Evolution of the magnetic properties, and appropriate models to describe nanoparticles behaviour when the diameter increases.
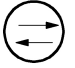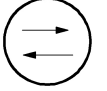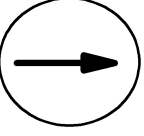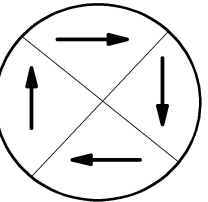
		H_C	Hyst. Area	Model	Validity conditions
Superparamagnetic State		0	0	/	Null hysteresis Null interest
		>0	$\alpha\ H^2$	Linear Response Thoery	Ellyptical hysteresis Low applied field
Single-Domain		>>0	$2\mu_0 H_C M_S$	Stoner Wohlfarth Theory	NPs saturated by magnetic field Rectangular hysteresis
Multi-Domain		>0	$\alpha\ H^3$	Rayleigh Theory	Reduction of H_C

Figure 2.3: Summary of SLP models and conditions of applicability.

The LRT model is not valid in all measurement conditions. From SLP and imaginary susceptibility expressions, it can be seen that the energy losses depend on frequency (combination of eq. (2.2) and eq. (2.14)): at low frequency ($\omega\tau \ll 1$) the SLP is proportional to the square of frequency, instead at high frequency ($\omega\tau \gg 1$) the SLP becomes independent from frequency. In the last case, the LRT model is not valid anymore because the MNPs aren't in the superparamagnetic state ($\tau_M \gg \tau$). In Fig. (2.3) the region of applicability of the different SLP models are summarized.

The fundamental point for LRT model is the superparamagnetic condition: from Chapter 1 this condition is verified when the energy barrier is less than the thermal energy, but it is not valid at high field [44]. Another condition requires that in the presence of a magnetic field applied along the axis of anisotropy, the relation $H < 3k_B T/(\mu_0 M_S V)$ should hold. This means that the field amplitude is within the linear range of the Langevin curve. In particular the last condition is of particular relevance for the hyperthermia magnetic particles [45]. As a consequence, the range of validity of the linear relaxation theory is restricted to small values of field amplitude and diameter of the particles, a condition shown in figure (2.4) by the area below the dashed line. Clearly, the optimal particle diameter for the linear theory decreases with increasing the field amplitude. For instance, for maghemite ($M_S \sim 400$ kAm^{-1}) a value of the magnetic field amplitude of 10 kAm^{-1} appropriate for hyperthermia, limits the validity of the relaxation model to $d < 16$ nm.
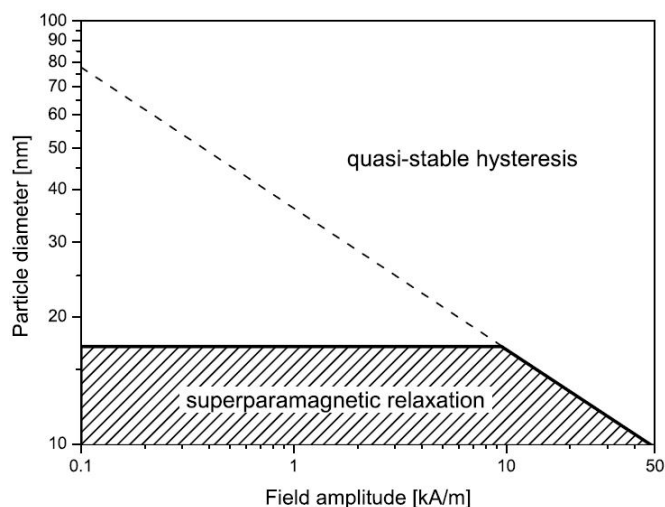
Figure 2.4: Critical diameter above which the linear theory ceases to be dependent on magnetic field amplitude (for magnetite particles with an effective anisotropy of 10 kJm^{-3} at a frequency of 400 kHz).

2.2 Nuclear Magnetic Resonance

The NMR relaxometric characterization of the samples has been performed at room temperature by measuring the longitudinal and the transverse nuclear relaxation times (T_1 and T_2) in the frequency range $0.01 \div 60$ MHz. The sequences used are the conventional Echo-inversion-recovery for T_1, and the CPMG for T_2 (for more details see Appendix). For $f < 7.2$ MHz, sequences typical of Fast Field Cycling (FFC) technique have been used.

2.2.1 NMR Basis

The ^1H NMR technique is based on the existence of an intrinsic magnetic moment of the hydrogen nucleus $\boldsymbol{\mu} = \gamma\hbar\mathbf{I}$, where $\mathbf{I}$ is the nuclear spin and $\gamma/2\pi$ is the gyromagnetic ratio for ^1H equal to 42.576 MHz/T. When a magnetic field (H_0) is applied, for example along the z axis, this magnetic moment precesses around the direction of field and his motion is described by the equation:

$$\frac{d\boldsymbol{\mu}}{dt} = \boldsymbol{\mu} \times \gamma\boldsymbol{H}_0 \qquad (2.16)$$

The magnetic moment precesses around H_0 with a specific frequency $\omega_L = \gamma H$, named Larmor frequency. For an ensemble of nuclei the total magnetization, composed by the sum of the moments in the direction of the static field, follows an equation similar to eq. (2.16).

If the magnetization along z axis is M_z, at equilibrium $M_z = M_0$, where M_0 is the maximum of magnetization: the NMR analysis is based on the study of the evolution of this vector during time. If one passes from laboratory frame to
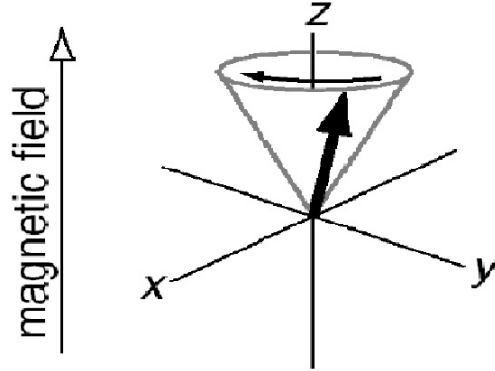
Figure 2.5: Magnetic moment precession in a magnetic field.

rotating frame and the additional resonating field (H_1) is applied, the equation (2.16) becomes:

$$\frac{d\boldsymbol{M}}{dt} = \boldsymbol{M} \times \gamma \left[k \left(\boldsymbol{H}_0 - \frac{\omega}{\gamma} \right) + \boldsymbol{H}_1 \right] = \boldsymbol{M} \times \gamma \boldsymbol{H}_{eff} \qquad (2.17)$$

In this frame the magnetization precesses around a new field (H_{eff}). If the rotating frame has a particular frequency, equal to the Larmor frequency, and H_1 is perpendicular to H_0, the magnetization vector precesses around H_1 in the x-y plane, without any perturbation from static field.

In the laboratory frame, the radio frequency pulse tends to dephase the magnetization (initially aligned along the static magnetic field) and the return to equilibrium of the nuclear magnetization is characterized by two different times: the longitudinal relaxation time (T_1), which is determined by the interaction of the nuclei with the lattice, and the transverse relaxation time (T_2), which is determined by the nuclear spin-spin interactions. At microscopic level, the longitudinal time is connected to the variation of the population on the Zeeman levels after the exchange of energy with the lattice excitations. On the other hand, the transversal time is determined by the interactions between nuclear spins in x-y plane.

The evolution of the magnetization is described by Bloch equations [46], which state the time evolution of the components of the nuclear magnetization; in a magnetic field they are written as:

$$\frac{dM_z}{dt} = \gamma (M \times H_0)_z + \frac{M_0 - M_z}{T_1} \qquad (2.18)$$

$$\frac{dM_{xy}}{dt} = \gamma (M \times H_0)_{xy} - \frac{M_{xy}}{T_2} \qquad (2.19)$$

The equations can be solved and the solutions depend on the initial conditions. In the rotating frame at $\omega_0 = \gamma_0 H_0$, the first term of the equations can

27

be neglected as the static magnetic field is cancelled by the opposite magnetic field $\omega_0/\gamma_0 = -H_0$. The solutions when the magnetization is in the plane are:

$$M_z(t) = M_0 \left[1 - \exp\left(-\frac{t}{T_1} \right) \right] \tag{2.20}$$

$$M_{xy}(t) = M_0 \exp\left(-\frac{t}{T_2} \right) \tag{2.21}$$

In the laboratory frame they are:

$$M_z(t) = M_z(0) \exp\left(-\frac{t}{T_1} \right) + M_0 \left[1 - \exp\left(-\frac{t}{T_1} \right) \right] \tag{2.22}$$

$$M_{xy}(t) = M_{xy}(0) \exp\left(-\frac{t}{T_2} \right) \exp(-i\omega_0 t) \tag{2.23}$$

These equations describes the return of the magnetization to the equilibrium position. In the modern spectrometers the NMR signal is detected by the same coil that generates the radio frequency pulse: the rotation of the magnetization in the xy plane generates an electromotive force (emf) on the coil that is called Free Induction Decay (FID), in according with the Faraday law. By the Fourier Transform of the FID signal, it's possible to evaluate the susceptibility that can be separated in two parts: real and imaginary. The equations for susceptibility are:

$$\chi'(\omega) = \frac{M_0}{H_0} \frac{\omega_0(\omega_0 - \omega)T_2^2}{1 + (\omega_0 - \omega)^2 T_2^2} \tag{2.24}$$

$$\chi''(\omega) = \frac{M_0}{H_0} \frac{\omega_0 T_2}{1 + (\omega_0 - \omega)^2 T_2^2} \tag{2.25}$$

The dissipative part of the nuclear spin susceptibility has a Lorentzian shape of width $1/T_2$ centered at the resonance frequency. In this way, the resonance is defined as a peak in the absorption spectrum at the Larmor frequency which is spread over a width due to the nuclear spin-spin relaxation.

2.2.2 Nuclear Relaxation Theory in Presence of Super-paramagnetic NPs

The presence of MNPs in the water modifies the proton relaxation. This type of interaction can be expressed by separating the relaxation mechanism into two parts: the *inner sphere* model and the *outer sphere* model [47].

The *inner sphere* (see Fig. (2.6)) contribution is related to three different mechanisms and their correlation times:

(i) the chemical exchange of the water molecules of the first coordination sphere with bulk water molecules: the dipole-dipole interaction (hyperfine interaction) between the molecules is mediated by electronic spins. In fact, the water molecule is replaced by another molecule in a characteristic correlation time τ_M. The continuous substitution of the water molecules in the first coordination sphere allows to diffuse the paramagnetic effect in all the sample.

(ii) the electronic spin relaxation, characterized by the correlation times τ_{S_i}, $i = 1, 2$;

(iii) the Brownian relaxation of the molecule characterized by τ_B, as already seen.

The inner sphere model is described by the Solomon Bloembergen-Morgan theory (SBM) [48, 49]:

$$\frac{1}{T_1^{IS}} = fq\frac{1}{T_1^M + \tau_M} \tag{2.26}$$

where f is the relative concentration of the paramagnetic complex, q is the number of water molecules in the first coordination sphere, T_1^M is the nuclear longitudinal relaxation time of the water proton nuclei of the first coordination sphere and τ_M is the water permanence time.

On the other hand, the *outer sphere* (see Fig. (2.6)) model predicts the nuclear relaxation due to long distance interactions between the spin of the paramagnetic substance and the nuclear spin of bulk water protons. This mechanism is modulated by the translational correlation time (τ_D) that takes into account the relative diffusion (D) of the paramagnetic center and the solvent molecule, and the distance of closest approach(d). This model was described by Freed [50], assuming that the diffusion time is given by:

$$\tau_D = \frac{d^2}{D} \tag{2.27}$$

where D is the relative diffusion coefficient.

Due to different mechanisms involved in outer and/or inner sphere models, the relaxation times T_1 and T_2 shorten and the different contrast agent (CA) made of (water) solutions of Gd-chelates MNPs can behave differently. They' re generally divided into positive (e.g. T_1-relaxing) and negative (e.g. T_2-relaxing) CA. T_1 agents increase the MRI signal intensity and the images result bright, so they are called positive contrast agents. An example of positive contrast agent is Gd-DTPA, that enhances the T_1 relaxation rate of protons mainly through the inner sphere relaxation [51].

On the other hand, T_2 agents largely increase $1/T_2$ of tissue, hence leading to a decrease of the signal intensity and are classified as negative contrast agents (the zone with contrast agent results dark). Paramagnetic materials increase $1/T_1$ and $1/T_2$ approximately equally, whereas superparamagnetic agents predominantly increase $1/T_2$. These agents include different types of inorganic iron particles which contain iron in different valence states, vary in their chem-
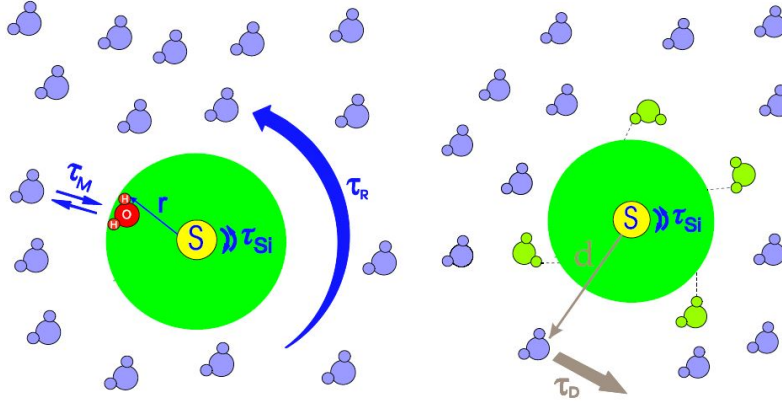
Figure 2.6: Scheme of Inner Sphere Model (left) and Outer Sphere Model (right); the blue spheres represent water molecules, while the bigger green sphere is the paramagnetic center. The first coordination sphere, with radius R, are coloured light-green.

ical composition, crystal structure, size, coating and have a strong effect on the transverse (spin-spin) relaxation process of the nearby protons.

The *inner* and *outer sphere* model gives a good model for relaxation but it allows to predict the relaxation only for some crystals with diameter larger than 15 nm, but fails for lower sizes (because the lower values for the anisotropy energy do not allow to assume that at any time the particle magnetization is parallel to the anisotropy axis).

In these cases, when the particles are superparamagnetic, model was implemented by Roch, Muller and Gillis [47, 52]. This model is the based of a number of assumption, which simplify the structure of nanoparticles anisotropy, listed below:

- The anisotropy is assumed uniaxial.

- Each superparamagnetic particle presents a single magnetic moment due to the superspin; the exchange interaction between NPs is supposed to be largest energy term.

- The rotation correlation time τ_R is assumed larger than the Néel relaxation time ($\tau_R \gg \tau_N$): this assumption gives a limitation to the anisotropy barrier height and to the angle θ between the anisotropy axis and the external field (this can be considered as a fixed parameter). τ_R depends on the diameter of nanoparticles while τ_N presents an exponential dependence on the volume: as a consequence, the model for ferrites is limited to a maximum diameter of ~ 20 nm.

- τ_N is the same for all the nanoparticles in the sample (all energy multiplets have the same probability of occupation).

Considering these assumptions, the Hamiltonian for single NP can be written as:

$$\mathbf{H} = \mathbf{H}_{ex} + \mathbf{H}_Z + \mathbf{H}_A \tag{2.28}$$

where $\mathbf{H}_{ex}$ is the exchange Hamiltonian, $\mathbf{H}_Z$ the Zeeman-coupling and $\mathbf{H}_A$ the magnetic anisotropy. By assumption, the exchange interaction is dominant and the superspin can be considered as a sum of all the single magnetic moments of the single ions. In this way, excluding the exchange Hamiltonian and rewriting the Zeeman and the anisotropy terms, the eq. (2.28) results:

$$H = -\gamma_S \hbar \mathbf{H}_0 \cdot \mathbf{S} - E_A(\mathbf{u}_S \cdot \mathbf{u}_A)^2 \tag{2.29}$$

where $\mathbf{S}$ is the crystal superspin of NP, γ_S is the electron gyromagnetic ratio, $\mathbf{H}_0$ is the external magnetic field, $\mathbf{u}_S$ is the unitary vector aligned along $\mathbf{S}$ and $\mathbf{u}_A$ is a unitary vector pointing in the direction of the anisotropy axis of the crystal.

The equations describing the longitudinal and transverse (T_1 and T_2) relaxivity between the superspin particles and the magnetic moment of the water hydrogen nuclei are:

$$
\begin{aligned}
\frac{1}{T_1} =& \frac{32\pi}{135000}\hbar^2\gamma_S^2\gamma_I^2\left(\frac{N_A C}{r_d D}\right)\Bigg\langle \sum_{i,j}\frac{\exp(-\beta E_i)}{Z}\Bigg\{\frac{(S_{-,ij}S_{+,ji} + S_{+,ij}S_{-,ji})}{2}\cdot \\
&\cdot\left[\frac{1}{2}J^F(\omega_I - \omega_{i,j}, \tau_D, \tau_N) + 3J^F(\omega_I - \omega_{i,j}\tau_D, \tau_N)\right] + \\
&+ 3|S_{z,ij}|^2\frac{(J^F(\omega_I - \omega_{ij}, \tau_D, \tau_N) + J^F(\omega_I + \omega_{ij}, \tau_D, \tau_N))}{2}\Bigg\} + \\
&- 3\langle S_z\rangle^2[J^F(\omega_I, \tau_D, \tau_N) - J^A(\sqrt{2\omega_I\tau_D})]\Bigg\rangle
\end{aligned}
\tag{2.30}
$$

$$\frac{1}{T_2} = \frac{32\pi}{135000}\hbar^2\gamma_S^2\gamma_I^2\left(\frac{N_A C}{r_d D}\right)\left\langle\sum_{i,j}\frac{\exp(-\beta E_i)}{Z}\left\{\frac{(S_{-,ij}S_{+,ji} + S_{+,ij}S_{-,ji})}{2}\cdot\right.\right.$$

$$\cdot\left[\frac{1}{4}J^F(\omega_I - \omega_{i,j}, \tau_D, \tau_N) + \frac{3}{2}J^F(\omega_I + \omega_{i,j}\tau_D, \tau_N)\right] +$$

$$+ 3|S_{z,ij}|^2\left[2J^F(\omega_{ij}, \tau\tau_D, \tau_N) + \frac{3}{4}(J^F(\omega_I - \omega_{ij}, \tau_D, \tau_N) +\right.$$

$$J^F(\omega_I + \omega_{ij}, \tau_D, \tau_N))\right]\left.\right\} - 2\langle S_z\rangle^2\left\{\left[J^F(0, \tau_D, \tau_N) + \frac{3}{4}J^F(\omega_I, \tau_D, \tau_N)\right] +\right.$$

$$\left.\left.- \left[J^A(0) + \frac{3}{4}J^A(\sqrt{2\omega_I\tau_D})\right]\right\}\right\rangle$$

(2.31)

The angle θ between the anisotropy axes and the magnetic field is included in the operators $S_{+,ij}$ and $S_{-,ij}$. The different parameters are:

- γ_S, γ_I the gyromagnetic ratios of electron and proton, respectively.

- N_A, the Avogadro number.

- C, the iron concentration.

- D, the water self diffusion coefficient.

- r_d, the minimum approach distance of the protons with respect to the center of the nanoparticle; if the nanoparticles are naked, r_d is equal to radius of magnetic core.

- $\exp(\frac{-\beta E_i}{Z})$, the Boltzmann occupation probability.

- S, the spin operator.

- τ_N, the Néel relaxation time.

- τ_D, the characteristic diffusion time (see eq. (2.27)).

- ω_I, the proton Larmor frequency.

- J^F and J^A, the spectral densities (Freed spectral density and the Ayant spectral density, respectively) which considers the different relaxation times of different NPs.

These expressions take into account the contribution of different relaxation processes (Curie and Néel relaxation) and the intensity of magnetic field. At low frequency the dominant component is the Freed density function which assumes the formula:

$$J^F(\omega, \tau_D, \tau_N) = Re\left[\frac{1 + \Omega^{1/2}/4}{1 + \Omega^{1/2} + 4\Omega/9 + \Omega^{3/2}/9}\right] \quad (2.32)$$

where $\Omega = (i\omega + 1/\tau_N)\tau_D$. In particular the total correlation time results from the competition between τ_D and τ_N. At intermediate field the relaxation rates are a combination of the high and low frequencies contribution, "weighted" by the Langevin function, which gives the M vs H curves of the sample. At high frequency the Curie relaxation (magnetization blocked along magnetic field, $\tau_N = 0$) dominates and the spectral density is given by the Ayant term:

$$J^A(z) = \frac{1 + 5z/8 + z^2/8}{1 + z + z^2/2 + z^3/6 + 4z^4/81 + z^5/81 + z^6/648} \quad (2.33)$$

where $z = \sqrt{2\omega_I\tau_D}$ depends on the proton Larmor frequency (see Fig. 2.7).

For core diameters greater than 7-8 nm, the equations (2.30) and (2.31) require, however, too long computational times. In order to solve this problem, the authors proposed another model, where the relaxation rates are modelized as linear combination of the limit expressions for $E_A \to \infty$ and $E_A = 0$:

$$\frac{1}{T_1} = \frac{32\pi}{135000}\mu_{SP}^2\gamma_I^2\left(\frac{N_A C}{r_d D}\right)\left\{7P\frac{L(x)}{x}J^F[\Omega(\omega_S, \omega_0), \tau_D, \tau_N]+\right.$$

$$+ \left[7Q\frac{L(x)}{x} + 3(P+Q)\left(1 - L^2(x) - 2\frac{L(x)}{x}\right)\right]J^F(\omega_I, \tau_D, \tau_N)+ \quad (2.34)$$

$$\left. + 3L^2(x)J^A(\sqrt{2\omega_I\tau_D})\right\}$$

$$\frac{1}{T_2} = \frac{32\pi}{135000}\mu_{SP}^2\gamma_I^2\left(\frac{N_A C}{r_d D}\right)\left\{13P\frac{L(x)}{x}J^F[\Omega(\omega_S, \omega_0), \tau_D, \tau_N]+\right.$$

$$+ 6Q\frac{L(x)}{x}J^F(0, \tau_D, \tau_N) + \left[1 - L^2(x) - 2\frac{L(x)}{x}\right][3J^F(\omega_I, \tau_D, \tau_N) \quad (2.35)$$

$$\left. + 4J^F(0, \tau_D, \tau_N)] + L^2(x)[3J^A(\sqrt{2\omega_I\tau_D}) + 4J^A(0)]\right\}$$

The factor P varies in the range 0-1 and represents the coefficient of the linear combination; in particular, for $P = 0$ one obtains the infinite anisotropy
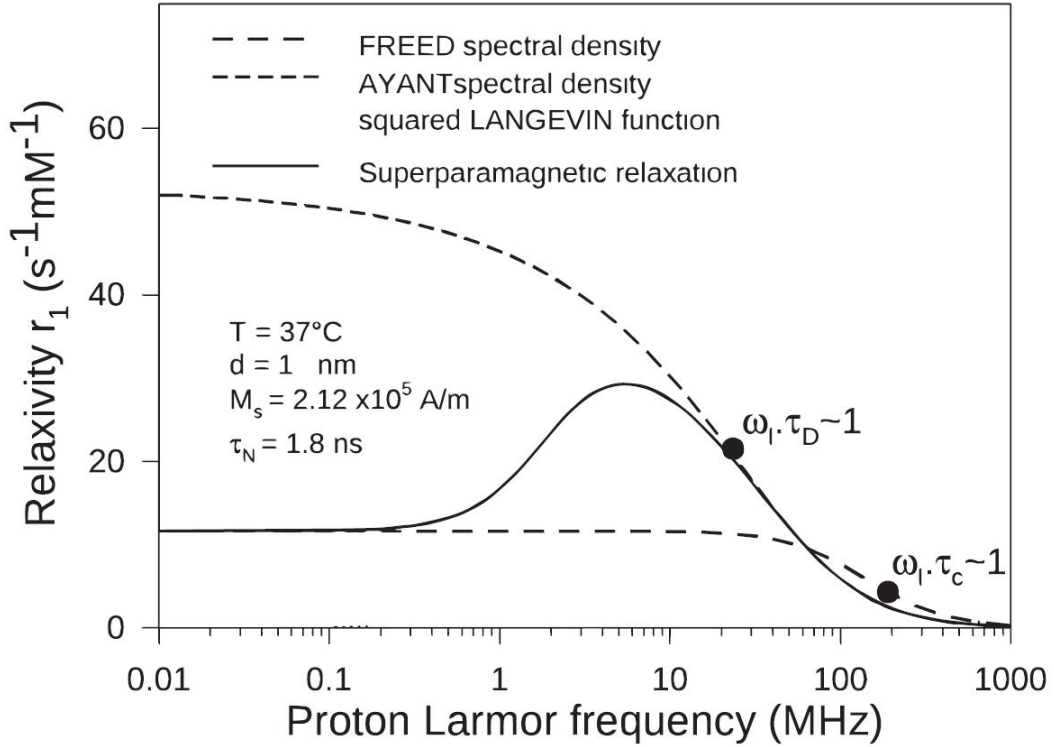
Figure 2.7: Simulated longitudinal relaxivity curves for a superparamagnetic material from Roch's model. The various contributions to the relaxivity are reported: in the low frequency region the relaxation process is dominated by the Freed spectral density but at high frequency Freed's contribution falls (it is not visible, since the Ayant spectral density describe relaxivity in such frequency range).

case and for $P = 1$ the zero anisotropy one. The value x is equal to $\mu_{SP}H/k_B T$ and is the coefficient of the Langevin function $L(x) = \coth(x) - 1/x$. The factors P and Q, in other words, weight the contribution of Zeeman and anisotropy energy. At high anisotropy energy (P equal to 0) the two expressions result simplified:

$$\frac{1}{T_1} = \frac{16\pi}{135000}\mu_{SP}^2\gamma_I^2\left(\frac{N_A C}{r_d D}\right)\left\{\left[\frac{L(x)}{x} + 3\left(1 - L^2(x) - \frac{2L(x)}{x}\right)\right]\cdot \right.$$
$$\left. \cdot J^F(\gamma_I, \tau_D, \tau_N) + 3L^2(x)J^A(\sqrt{2\gamma_I\tau_2})\right\} \tag{2.36}$$

34

$$\frac{1}{T_2} = \frac{16\pi}{135000}\mu_{SP}^2\gamma_I^2\left(\frac{N_AC}{r_dD}\right)\left\{7\frac{L(x)}{x}J^F\left[\gamma_I,\tau_D,\tau_N + 6\frac{L(x)}{x}(0,\tau_D,\tau_N)\right]+\right.$$

$$+\left[1 - L^2(x) - \frac{2L(x)}{x}\right]\cdot[3J^F(\omega_I,\tau_D,\tau_N) + 4J^F(0,\tau_D,\tau_N)]+$$

$$\left.+ L^2(x)[3J^A(\sqrt{2\omega_I\tau_D}) + 4J^A(0)]\right\}$$

$$(2.37)$$

Within the used approximated model, it can be evinced that (see Figure 2.8) at low frequency the value of T_1 and T_2 of the two types of relaxation curves is the same (superspins distributed randomly, no preferential anisotropy direction). The difference among T_1 and T_2 becomes evident when the frequency increase: this is due to $4L^2(x)J^A(0)$, directly connected to the magnetization of the nanoparticles.
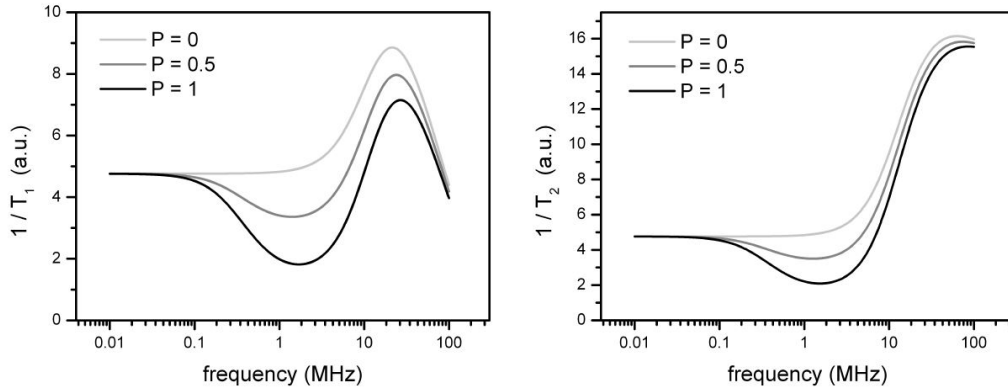

Figure 2.8: Theoretical relaxation rate curves for different values of P (eq. 2.35).

2.2.3   D-NMR curves

Through the fitting of the T_1 and T_2 functions as a function of frequency one can extract interesting parameters able to give other information about magnetic structure and coating effects on nanoparticles:

- The average distance of minimum approach (d): this is the distance between water molecules and nanoparticles. From $\omega_I\tau_D \sim 1$ (correct at high field, see Fig. 2.9) it is possible to estimate τ_D, and so d ($\tau_D = d^2/D$).

- τ_N: Néel relaxation time.

- The average magnetic volume: the part of magnetic volume that contributes to relaxation.

- P and Q: these parameters give an idea of the importance of the energy barrier contribution to the relaxation rates.
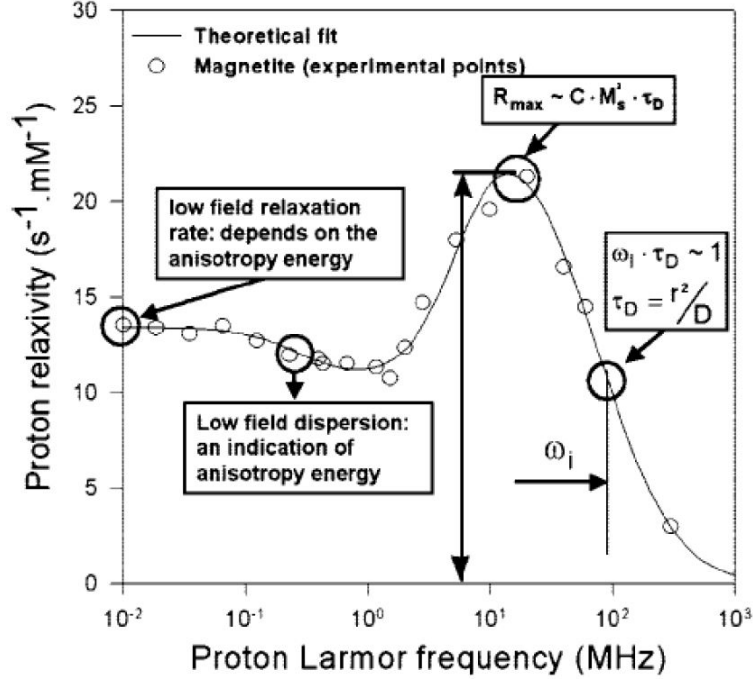

Figure 2.9: Longitudinal relaxation simulated at room temperature for a particle with radius $r=4$ nm and $M_S=53$ Am^2/kg in colloidal solution.

2.2.4 MAR and SDR Models

As will be seen in the next two chapters, the RMG model is useful and suitable for longitudinal relaxivity profile analysis, but present many difficulties when it is used to fit the transversal relaxivity profile, appearing poor in the explanation of the strong increase of the exponential transverse relaxivity at high frequencies with respect to the predicted one (see Fig. 2.8).

Starting from the *outer* sphere theory, which deals with the fluctuations of the local magnetic field around a (para- or superpara-) magnetic center, a simple model was proposed [53]. This model derives the T_2 expression in the limits of motional averaging regime (MAR), i.e. fast motion $\omega\tau \gg 1$, and the static dephasing regime (SDR), i.e. $\omega\tau \ll 1$, slow motions [54, 55, 56].

Within the MAR regime ($\omega\tau \gg 1$), the contribution of the transverse relaxation, from eq. (2.37), can be written as:

$$\frac{1}{T_2} = \frac{64\pi}{135000}\gamma^2 N_A C \mu_{SP}^2 \frac{\tau_D}{r_d^3} \qquad (2.38)$$

Defining the value $\Delta\omega = \gamma\mu_0 M_V/3$ as the difference between Larmor proton frequency on the surface and the same frequency in the bulk, the equation can be simplified as follow:

$$\frac{1}{T_2} = \frac{4}{9}V_f\tau_D(\Delta\omega)^2 \qquad (2.39)$$

where V_f is the volume fraction of magnetic material in the sample.

Normalizing this volume over the molar concentration of Fe or Ferrite, one has the relation $(V_f/C) = (m_{mol}/\rho_{mol})$. In the case of Maghemite, the molar volume v_{mol} is:

$$v_{mol} = \frac{M_{\gamma-Fe_2O_3}}{3\rho_{\gamma-Fe_2O_3}} \simeq 1.5 \cdot 10^{-5} \qquad (2.40)$$

Considering v_{mol} and introducing the approximate expression of the relaxivity $r_2 = \frac{1}{cT_2}$, the equation (2.39) can be rearranged in order to explicit the dependence of r_2 on the diameter:

$$\frac{r_2}{M_V^2} = \frac{4\gamma^2\mu_0^2 v_{mol}d^2}{405D} = 5.9 \cdot 10^{-12}d \qquad (2.41)$$

Where d is the diameter of the outer sphere (which includes the coating, assumed equal to the minimum approach distance) and D is the self diffusion constant of the water.

Vuong and coworkers [53] collected a large quantity of data about the structural and the relaxometric properties of several magnetic nanostructures, trying to verify experimentally and in a systematic way the validity of the MAR model over a wide range of diameters. The quadratic dependence on the diameter was verified, but the curve which fits the data was slightly different from the above equation, being $r_2/M_V^2 = 11.6 \cdot 10^{-12}d^2$.

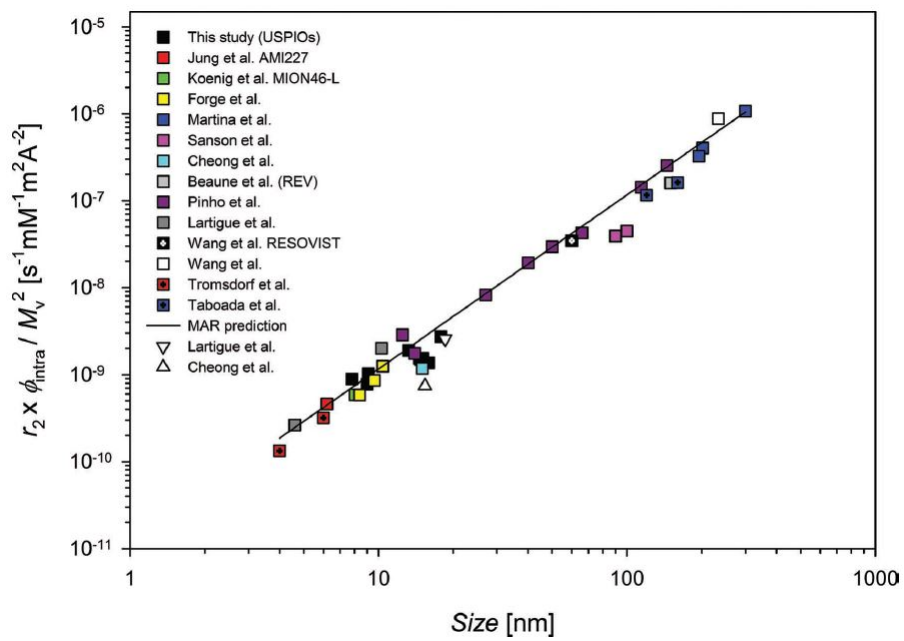The mutual dependence between relaxivity and diameter is reported in Fig. (2.10).

Figure 2.10: Samples transversal relaxivity vs NPs diameter in the motional averaging regime (MAR).

Chapter 3

Core Size Effects in Nanoparticles

3.1 Overview

A crucial role to develop nanoparticles with high hyperthermic efficiency, is played by the study of the intrinsic properties and the correct estimation of the parameters that can influence the heat release. In this direction, there are main parameters that can be optimized to change the physical properties of the NPs: the saturation magnetization M_S (since the maximum SLP is directly proportional to the square of M_S) and the anisotropy. These two parameters depend strongly on the kind and size of magnetic core of the NPs, in addition to the coating (see next chapter) [57].

Three samples of different size in the SP regime have been synthesized in the chemical laboratory in Florence and, in this chapter, their morphological, magnetic and hyperthermic properties are investigated.

These NPs are in the superparamagnetic region and have been studied for different fields to deduce the optimal model to explain the SLP increase.

The microscopic structure has been studied in Florence with a standard transmission electron microscopy (TEM, CM12 PHILIPS microscope operating at 100 kV) and in Milan with an Atomic Force Microscopic (AFM, Bruker Nanoscope Multimode IIId system operating in air, in tapping-mode), in order to characterize the dimensions of the core and of the coating layer of the particles. The information extracted from the analysis of the magnetic measurements, such as the saturation magnetizations (M_s), the coercive field (H_C) and other important parameters were obtained from ZFC-FC and hysteresis curves collected with Superconducting Quantum Interference Devices (SQUID, Quantum Design MPMS magnetometer) in Florence.

3.2 Synthesis Method

The three nanoparticles (A, B, C) have been synthesized at Chemistry Department of University of Florence (Dr. Andrea Guerrini) by thermal decomposition of metal-organic precursors in high boiling solvents, in the presence of surfactant.

The thermal decomposition can be divided in three different steps. In the first an organometallic precursor is decomposed in monomer that represents the base of the crystal. In the second step the concentration of the monomer is increased over the saturation level and start the formation of the first crystal seeds. In the last part, the reaction proceeds with addition of other monomers to have a crystal growth.

Iron(III) acetylacetonate (2 mmol), Oleylamine (2,5 mmol) and Oleic Acid (2 mmol) were dissolved in Benzylether (40 mL) and stirred under nitrogen flow for 15 min at room temperature; the mixture was heated at 200 C for 30 min and then maintained at 300 C for a variable duration to obtain MNPs of three different sizes. Then, the mixture was cooled down to room temperature, the black MNPs precipitate was magnetically separated, cleaned with ethanol and suspended in toluene. Finally, in order to exchange the Oleic Acid coating and suspend the MNPs in water, 4 mL of each sample, with MNPs concentration 10 mg/mL, was reacted with 40 mg of PolyAcrylic Acid (PAA) in TetraHydroFuran (THF).

3.3 Morphological Structure

In order to evaluate the core sizes of the maghemite nanoparticles, measurements have been performed by mean of Transmission Electron Microscopy (TEM). The dimensions of the nanoparticles were calculated from the analysis of more than 300 nanoparticles with the hypothesis of a LogNormal distribution for the diameters:

$$\rho(D) = \frac{1}{< D_{TEM} > \sigma\sqrt{2\pi}} \exp\left[-\left(\frac{\ln^2(D/< D_{TEM} >)}{2\sigma^2}\right)\right] \qquad (3.1)$$

where $< D_{TEM} >$ is the mean particle diameter The mean diameter and the standard deviation were obtained with the expression:

$$\mu = < D > \exp\left(\frac{\sigma^2}{2}\right) \qquad \sigma_\mu = < D > \sqrt{exp^{\sigma^2} - 1} \qquad (3.2)$$

The TEM images, the size distributions and their fit curves for all samples are shown in Fig. (3.1) and the results of the fits are reported in TAB. 3.1.

To define the crystalline structure (the internal structure of the maghemite) XRD measurements were performed and the data were fitted with a PseudoVoigt function to estimate the peaks position and the FWHM (Full Width
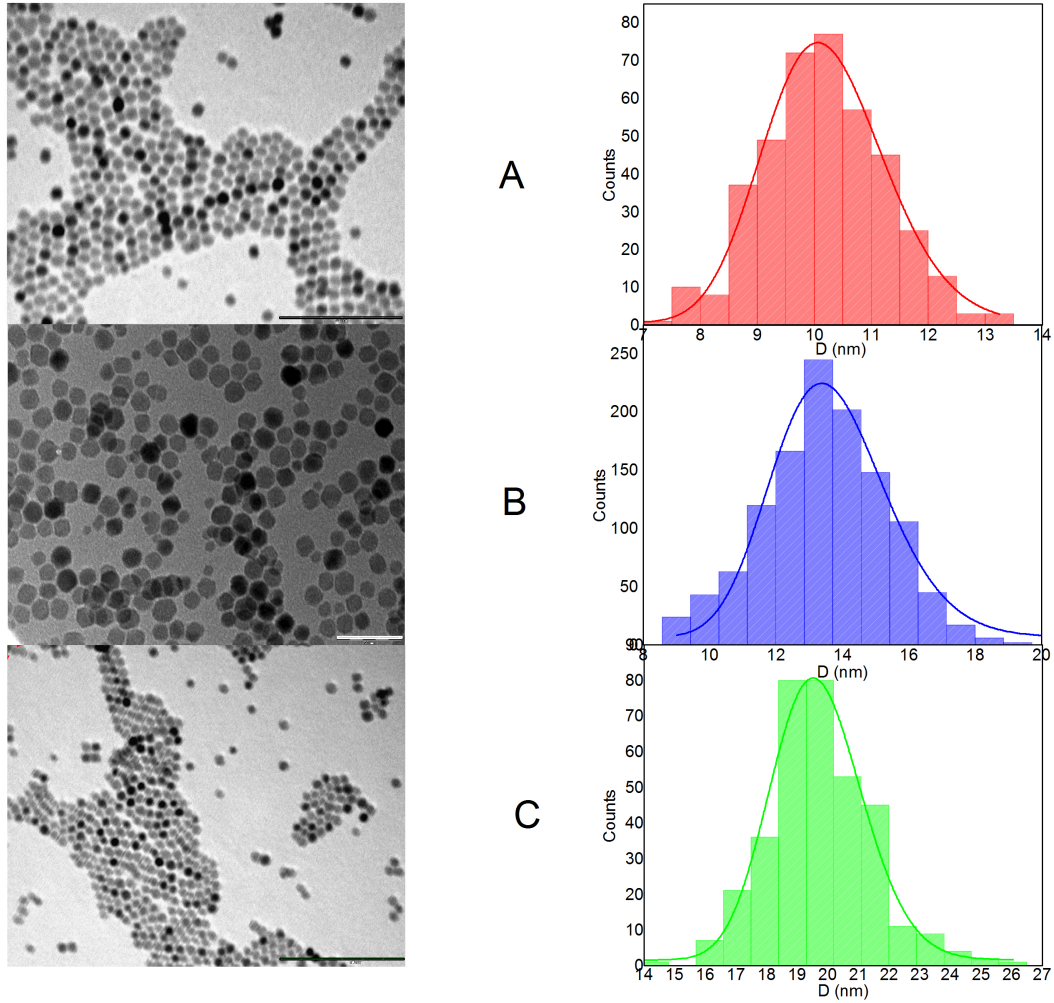
Figure 3.1: TEM images of the nanoparticles (scale bar is 100 nm for A and C, 50 nm for B) and the size measurements fitted with LogNormal distribution (solid lines).

at Half Maximum): the mean dimension of the crystalline coherent domain (i.e., crystallite) was obtained by the Scherrer's equation:

$$< D_{XRD} >= \frac{K\lambda}{\beta \cos\theta} \qquad (3.3)$$

where K is a constant related to the crystallite shape (0.9) and β is the line broadening at the half maximum intensity (FWHM). The XRD patterns of the nanoparticles (Fig. (3.2)) show the presence of nanocrystalline iron oxide spinel phase: in particular the patterns can be ascribed either to the polymorph of the ferric oxide ($\gamma - Fe_2O_3$) or the mixed valence iron oxide (Fe_3O_4). The particles size, determined by the peak broadening, is in agreement with the TEM observations.

In addition to the core properties, also the coating can influence the heat release. For this reason AFM measurements were performed. The samples
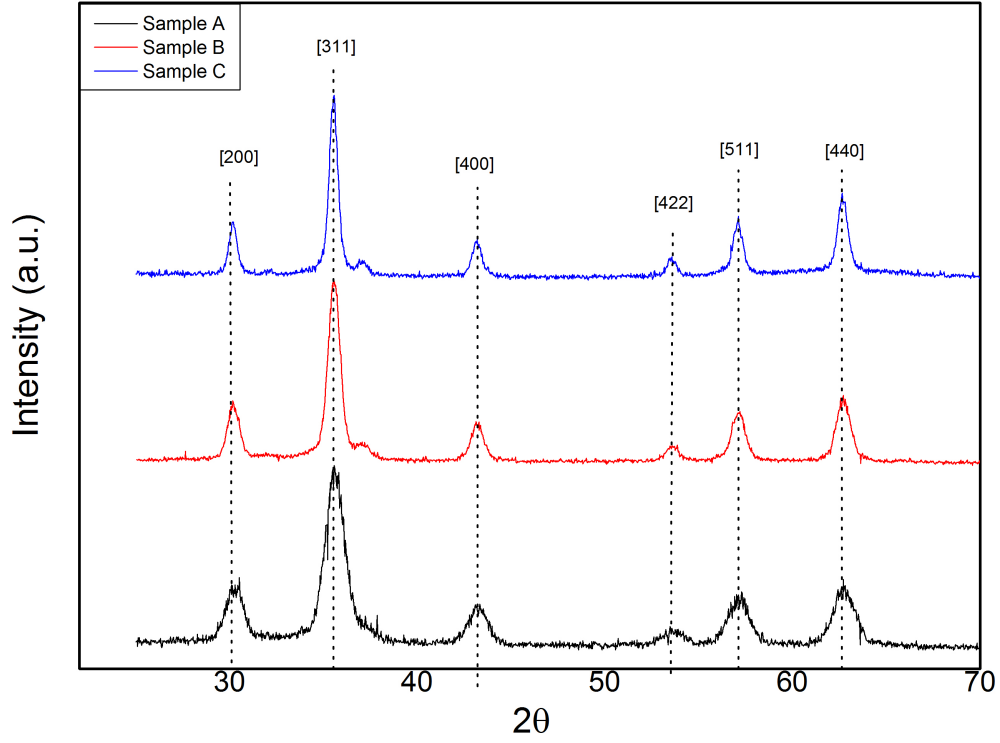
Figure 3.2: X-ray diffractograms of different nanoparticles.

Sample	D_{XRD} (nm)	D_{TEM} (nm)	D_{AFM} (nm)
A	7.4 ± 0.7	10.2 ± 1.1	11.4 ± 0.9
B	11.4 ± 0.5	14.6 ± 1.8	15.6 ± 0.8
C	14.9 ± 0.6	19.7 ± 1.7	20.5 ± 0.8

Table 3.1: Different size analysis for each samples: XRD for the crystalline structure, TEM for the ferrite core and AFM for core plus coating.

were diluted in ultra pure water (milliQ) and 3 μL have been used for the experiments. The images were recorded in an area 3x3 μm^2, with tapping mode, in air.

The coatings resulted very thin, with thickness below 2 nm. The main morphological features are summarized in Table 3.1.

3.4 Magnetic Properties

A static magnetic characterization was performed by means of a Superconducting Quantum Interference Device (SQUID) with a superconducting magnet ($H_{max} = 5.5$ T) in the temperature range 2-300 K. To avoid any displacement of the nanoparticles during the measurements, the samples, in the form of
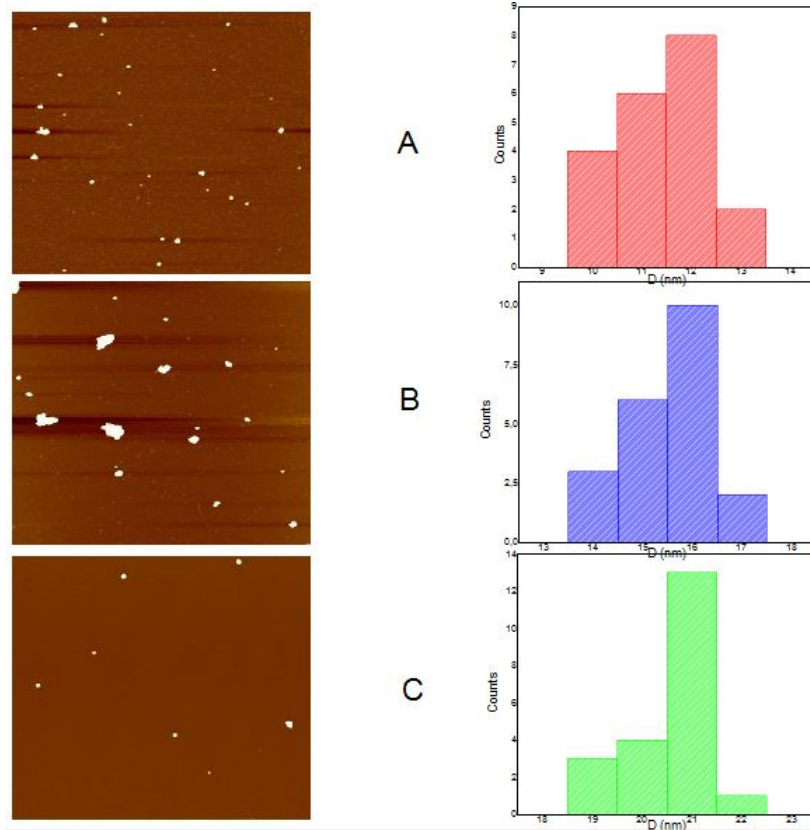
Figure 3.3: AFM images (left) and count values for 25 nanoparticles (right).

powders, were immobilized in an epoxy resin. We studied the dependence of the total magnetization from the static applied magnetic field and from the temperature. A collection of hysteresis cycles for the investigated samples is presented in Figure (3.4). At room temperatures only the first magnetization curves have been studied to determine M_S and H_C; no coercivity is observed, so we hypothesize that all samples are in a superparamagnetic state. On the other hands, at 2.5K the hysteresis loops present a small hysteresis area, indicating that the thermal energy is not enough to overcome the anisotropy barrier ($E_b \gg k_B T$) and the system is in ferromagnetic state (it is satisfied the Stoner-Wohlfarth model condition). In each case, the magnetic saturation at 2.5 K was estimated fitting the magnetization data at high field, with the empirical formula [58]:

$$M = M_0 \left(1 - \frac{A}{H} - \frac{B}{H^2} \right) \tag{3.4}$$

This equation is useful when the nanoparticles are close to superparamagnetic regime. The values of magnetic saturation at 2.5 K obtained from (3.4) are reported in table (3.2): as expected, the magnetic saturation increases with the diameter. The coercive field is higher for sample C while, the values of

H_C ($\mu_0 H_C$<300 Oe) for samples A and B are comparable. The coercive field observed at T=2.5 K implies that the available thermal energy is not enough to overcome the anisotropy barrier and the system is in a blocked ferrimagnetic state. On the other hand no coercivity is observed at T=300 K, so that it can be assumed that all samples are in superparamagnetic state.
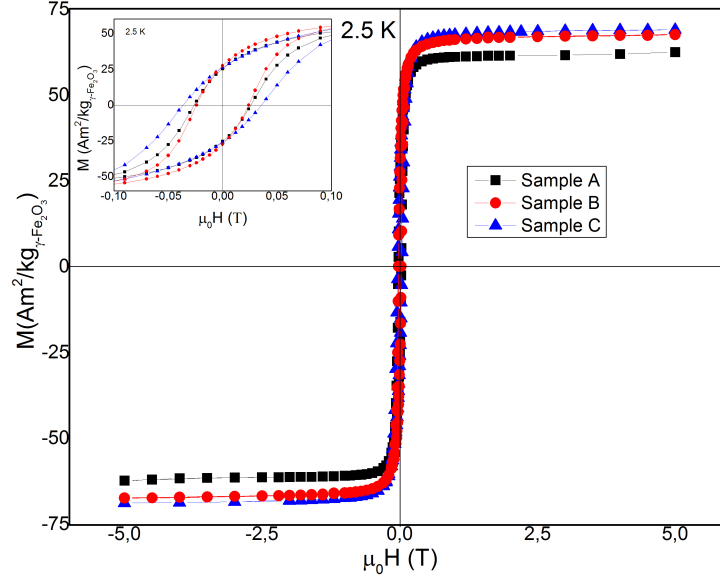

Figure 3.4: Magnetization as a function of magnetic field at T=2.5 K. The inset of the figure shows a particular on the coercive field at low temperature.

In the simplest approximation of Stoner and Wohlfarth, an estimation of K_{eff} can be obtained from:

$$K_{eff} = \frac{\mu_0 H_K M_S}{2} \tag{3.5}$$

From this equation, a roughly approximate value of the effective anisotropy constant can be obtained assuming negligible deviation from cubic anisotropy, negligible interparticle interactions and considering that $H_C = 0.48 H_K$.

The equation (3.5) is an approximation useful when the temperature of the hysteresis loops measurements is low compared to the blocking temperature of the nanoparticles. The non-approximate equation for nanoparticles with random orientation of the easy axis is [59]:

$$H_C = 0.48 H_K \left[1 - \left(\frac{T}{T_B} \right)^{0.77} \right] \tag{3.6}$$

In our case, the nanoparticles present a blocking temperatures higher than 2.5 K (as extracted from ZFC-FC).

At room temperature the hysteresis loops result completely closed indicating that the thermal energy is higher than the anisotropy energy and the

magnetization is free to move. In this case the curves were fitted to a Langevin function:

$$M(H) = M_S L\left(\frac{\mu H}{k_B T}\right) = M_S\left[\coth\left(\frac{\mu H}{k_B T}\right) - \frac{k_B T}{\mu H}\right] \quad (3.7)$$
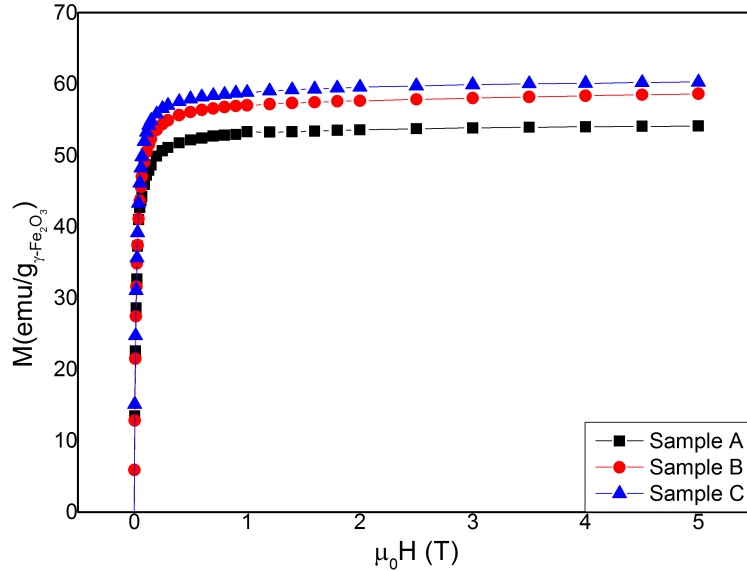

Figure 3.5: Magnetization at room temperature (300 K).

Sample	$M_S^{2.5}$ (emu/g)	$\mu_0 H_C^{2.5}$ (Oe)	M_S^{300} (emu/g)	$K_{eff} \cdot 10^4$ (J/m^3)
A	62.4 ± 3.4	265 ± 13	54.6 ± 3.0	1.65
B	65.6 ± 3.7	239 ± 15	58.3 ± 3.2	1.85
C	69.3 ± 3.8	360 ± 12	60.9 ± 3.3	2.56

Table 3.2: Saturation magnetization M_S and coercive field H_C at 2.5 K, M_S at room temperature and effective anisotropy constant K_{eff} obtained from hysteresis curves using Eq. (3.5).

In order to evaluate experimentally the blocking temperature, DC susceptibility measurements as a function of temperature were performed. In the zero-field cooled (ZFC) and field-cooled (FC) curves, the samples were cooled in zero field down to T=2 K; a magnetizing field H=25 Oe was then applied and the ZFC magnetization was measured. In the FC magnetization (M_{FC}) the samples were cooled in the presence of a field H=25 Oe down to T=2 K and the magnetization measured while increasing T. The ZFC magnetization curves present a maximum at a temperature (T_{max}) which is related to the average blocking temperature ($T_B \propto \beta T_{max}$), where β is a proportionality constant depending on the type of size distribution [60]. The temperature below

which the ZFC and FC curves show an irreversible behaviour (T_{irr}) is associated with the blocking of the biggest particles, assuming that the anisotropy energy barrier is determined by the magnetocrystalline anisotropy [61]. The continuous increase of M_{FC} with decreasing temperature indicates that interparticle interactions, if present, are weak [62].

The ZFC-FC curves for samples B and C present behaviours compatible with the iron oxide nanoparticles reported in literature having similar dimensions [63]; in particular in the sample B we can see a Verwey transition, ascribed to a slower oxidation rate towards oxidation of this sample, as compared to sample A and B. The sample A presents a polydispersion visible in the spread ZFC profile curve.

The temperature T_{max} of the maximum in the ZFC curve (i.e. the temperature at which the alignment of the spins with the external field is maximum) increases with the volume of the nanoparticles.

Sample	T_B (K)	T_{max} (K)	T_{irr} (K)
A	89 ± 12	230 ± 5	250 ± 5
B	61 ± 18	280 ± 5	>300
C	>300	>300	>300

Table 3.3: Blocking, maximum and irreversible temperatures obtained from ZFC-FC curves. The blocking temperatures were derived with differential method.
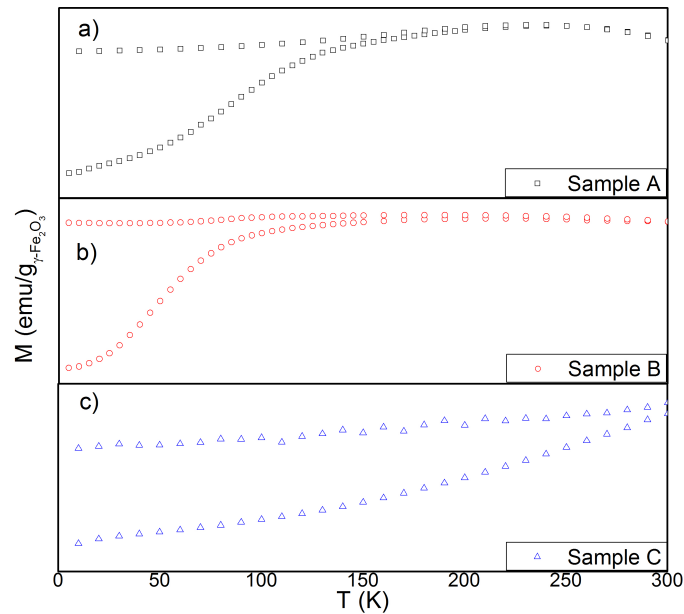

Figure 3.6: ZFC-FC magnetization curves for the samples studied.

3.5   Analysis of the Core Effect

The MFH measurements were performed with the MagneTherm system at University of Milan and complementary measurements have been done using a home-made calorimeter at University of Florence.

The concentration of the sample was 3.4-3.6 mg_{Fe}/mL for A and C, respectively, and 5.5 mg_{Fe}/mL for sample B: the differences of iron concentration don't influence the SLP results because, from eq. (2.4), the SLP were evaluated relatively to the concentration of the magnetic part. In Figure (3.7) the temperature increment at different field and frequency combination are reported: the measurements were performed for an irradiation (in alternating magnetic field) time of 300 s.

The results show a greater increment in temperature for sample C, as expected because made out of large nanocrystals, while A and B have an average increment around 5 °C. The initial temperature is the same for all the sample (21 °C), corresponding to the room temperature.

The fitting method used for the cases reported in figure and in all the other cases depends on the ΔT increment: if ΔT is of the order of few degrees the linear fit can overestimate the slope of the curves, in particular in the first part, where the increment from initial temperature can be affected by a non adiabatic condition of measure, or the slope is too flat to allow to extract a value. On the other hand, the use of Box-Lucas fit for curves with big temperature increment is not properly correct because can underestimate the initial slope of the curves being the fit extended to the whole curve.
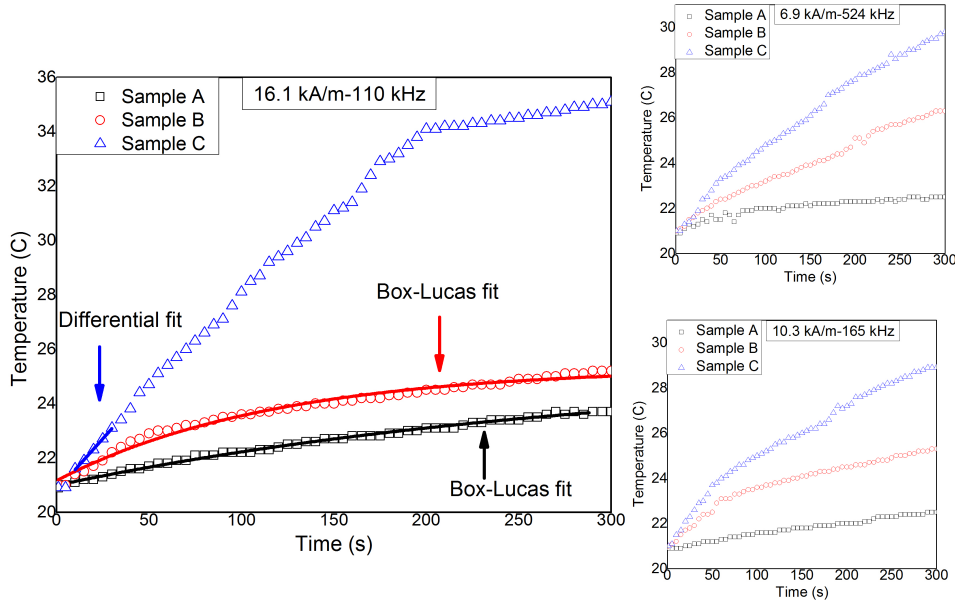

Figure 3.7: Increment of temperature at different fields and frequencies. In the left figure the fitting methods are reported: for sample A and B Box-Lucas (bold lines) fit were used, while for sample C the linear fit was utilized.
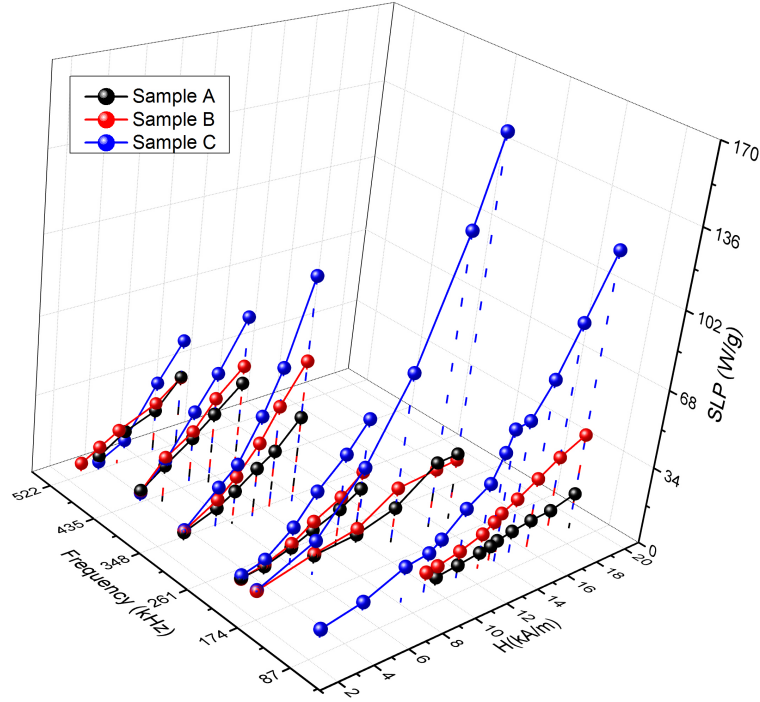
Figure 3.8: SLP as a function of field and frequency for samples A, B, C.

By using the equation (2.5) the SLP at different frequency and field were evaluated. The best SLP results are shown in Fig. 3.8. Sample C presents the higher values of SLP, as expected from high slope values, in particular at 207 kHz with a field of 14.8 kA/m.

As introduced in the previous Chapter, for the correct SLP interpolation is important to use the most appropriate model. For this reason a valid starting point is to calculate the maximum value of the applied field that satisfies the equation:

$$\xi = \frac{\mu_0 M_S V H_{max}}{k_B T} > 1 \tag{3.8}$$

When ξ becomes bigger than 1 we can apply the Stoner-Wolhfarth theory only if $H_{max} > 2H_C$. Our experimental conditions don't allow to use the Stoner-Wolhfarth theory because the maximum field is 16.1 kA/m and as reported in Table (3.4), the coercive field has a maximum value of 360 Oe (28 kA/m).

On the other hand, the value ξ doesn't depend on the frequency of the measurements but only on the field: so the calculated limit for H is valid for any measurement condition.

In addition to this parameter, in the previous chapter the adimensional parameter κ (eq. (2.11)) was introduced; κ is a function of core size and allows to establish the magnetic phase of the samples: if $\kappa > 1.6$ the nanoparticles are superparamgnetic and can be described with LRT model and if $0.7 <$

$\kappa < 1.6$ the only valid model is LRT, if $\kappa < 0.7$ the nanoparticles are in the ferromagnetic state described by the Rayleigh condition.

In order to evaluate the magnetic regime for nanoparticles, for each frequency H_{max} and H_{min} have been calculated. The sample A presents $\kappa > 1.6$ for all magnetic fields used in our analysis; this means that it is in a superparamagnetic condition. About sample B, instead, for some H values it has $\kappa < 1.6$ but always $\kappa > 0.7$. In this case the LRT seems applicable but ξ is greater than 1 and the model is not justified. The last sample (C) has $\kappa < 0.7$ for each field (as expected because its diameter exceeds the critical diameter for superparamagnetism) and it shows a ferromagnetic behaviour. In Table 3.4 the magnetic field limits are shown.

	110 kHz		146 kHz	
Sample	H_{min} (kA/m)	H_{max} (kA/m)	H_{min} (kA/m)	H_{max} (kA/m)
A	$8.6 \cdot 10^3$	$2.3 \cdot 10^4$	$6.5 \cdot 10^3$	$1.8 \cdot 10^4$
B	14	$6.1 \cdot 10^2$	11	$4.6 \cdot 10^2$
C	0	1	0	0.7

	179 kHz		207 kHz	
Sample	H_{min} (kA/m)	H_{max} (kA/m)	H_{min} (kA/m)	H_{max} (kA/m)
A	$5.3 \cdot 10^3$	$1.4 \cdot 10^4$	$4.6 \cdot 10^3$	$1.2 \cdot 10^4$
B	8.6	$3.8 \cdot 10^2$	7.5	$3.2 \cdot 10^2$
C	0	0.6	0	0.5

	237 kHz		340 kHz	
Sample	H_{min} (kA/m)	H_{max} (kA/m)	H_{min} (kA/m)	H_{max} (kA/m)
A	$4 \cdot 10^3$	$1.1 \cdot 10^4$	$2.8 \cdot 10^3$	$7.5 \cdot 10^3$
B	6.5	$2.8 \cdot 10^2$	4.5	$2 \cdot 10^2$
C	0	0.5	0	0.3

	423 kHz		524 kHz	
Sample	H_{min} (kA/m)	H_{max} (kA/m)	H_{min} (kA/m)	H_{max} (kA/m)
A	$2.2 \cdot 10^3$	$6 \cdot 10^3$	$1.8 \cdot 10^3$	$4.9 \cdot 10^3$
B	3.7	$1.6 \cdot 10^2$	3	$1.3 \cdot 10^2$
C	0	0.5	0	0.2

Table 3.4: Limit values for H at different frequencies, where the conditions $\kappa < 0.7$ and $\kappa > 1.6$ are verified.

The LRT model can be applied only for sample A and, only in few conditions, for sample B. The SLP data were fitted with a simple model $SLP = \alpha H^2$ to confirm the compatibility of LRT model for A and B (C is not in the LRT regime). If the conditions for ξ and κ are strictly respected, the fits with LRT equation can be performed for sample A but not for samples B and C. In Fig. (3.9) the SLP data fits as a function of the frequency are reported for sample A.

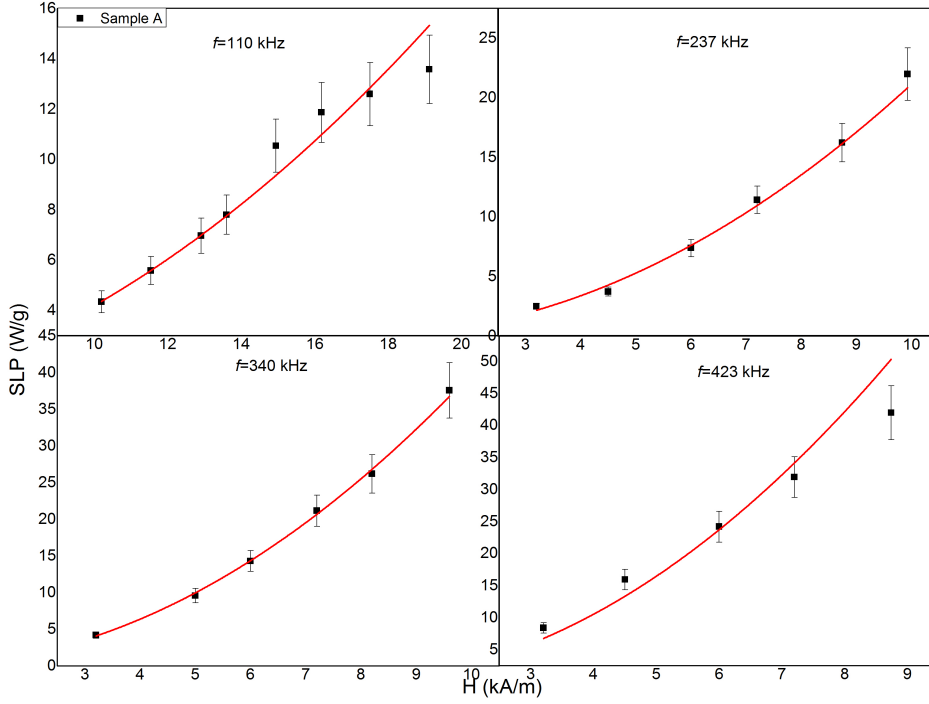For samples B and C, the LRT cannot be used as well as the Rayleigh ap-

Figure 3.9: SLP as a function of field and frequency for sample A; the fits were performed with the LRT model and show a good agreement with experimental data.

proximation because the diameters of nanoparticles are well below the critical value cited in the first chapter. Furthermore also the Stoner-Wohlfarth can't be used, because the maximum applied field (16.1 kA/m) is less than $2H_C$ for each sample.

Therefore, to modelize the behaviour of nanoparticles near the SPM-FM transition, we fitted the SLP data with a heuristic model (free exponential model), where $SLP \propto H^x$. The equation used are:

$$
\begin{aligned}
SLP &= \alpha H^2 & LRT \\
SLP &= \beta H^x & FEM
\end{aligned}
\tag{3.9}
$$

The comparison between the LRT and the free exponential model (FEM) is reported in Fig. (3.10). One can notice: (a) for sample A a perfect overlap between the LRT and FEM trend (proportional to H^2), meaning that sample A has a conventional superparamagnetic behaviour. (b) Different results were obtained by fitting the SLP curves for sample B and C: for B the curves present a similar trend at low field (under 12 kA/m). This means that B is in the transition SPM-FM zone, and the increase of magnetic field shifts the sample in the ferromagnetic zone. The sample C is a perfect ferromagnet because all points are out of the LRT model and the trends of the curves are very different;

in particular at high field the H^2 law cannot follow the experimental points.

As concerns the power law, for sample A x is equal to 2 (as expected), whereas for samples B and C one can observe $x>2$, increasing with frequency. This is understandable if we think that the nanoparticles for these two samples shift their behaviour toward ferromagnetic multi-domain structure, a condition for which heuristically SLP is proportional to H^3.

In table (3.5) the values of the exponent at different frequencies are reported.

Sample	Frequency (kHz)	x	Frequency (kHz)	x
A		2.0 ± 0.1		2.03 ± 0.05
B	110	2.23 ± 0.08	146	2.2 ± 0.1
C		2.3 ± 0.1		2.27 ± 0.1
A		2.09 ± 0.7		2.10 ± 0.05
B	179	2.19 ± 0.09	207	2.25± 0.12
C		2.37 ± 0.12		2.55 ± 0.05
A		2.03 ± 0.01		2.09 ± 0.09
B	237	2.30 ± 0.2	340	2.34 ± 0.03
C		2.47 ± 0.09		2.64 ± 0.06
A		2.05 ± 0.09		2.12 ± 0.1
B	423	2.43 ± 0.1	524	2.41± 0.15
C		2.53 ± 0.08		2.67 ± 0.08

Table 3.5: Exponent values for the law $SLP \propto H^x$. The values increases with the dimensions of nanoparticles.

In cases where the LRT model has been applied to fit the experimental results, an estimate of the value of the imaginary part of susceptibility of ferrofluid can be obtained, and from this an evaluation of the effective relaxation times of the nanoparticles.

For SLP, in the LRT model one can use the formula:

$$SLP = \frac{\mu_0 \pi f \chi''}{\rho} H^2 \qquad (3.10)$$

where the imaginary susceptibility is:

$$\chi'' = \chi_0 \frac{2\pi f \tau}{1 + (2\pi f \tau)^2} \qquad (3.11)$$

The susceptibility presents a maximum when the product between the frequency of the measuring field and the relaxation time of the system is equal to one, i.e. $\omega_m \tau = 1$; as a consequence for each frequency it's possible to evaluate the relaxation time. The effective relaxation time (τ_{eff}) is dominated by Néel relaxation for A and partially B but not for sample C, where the big dimensions cause the Brown relaxation to be the dominant time. At a first
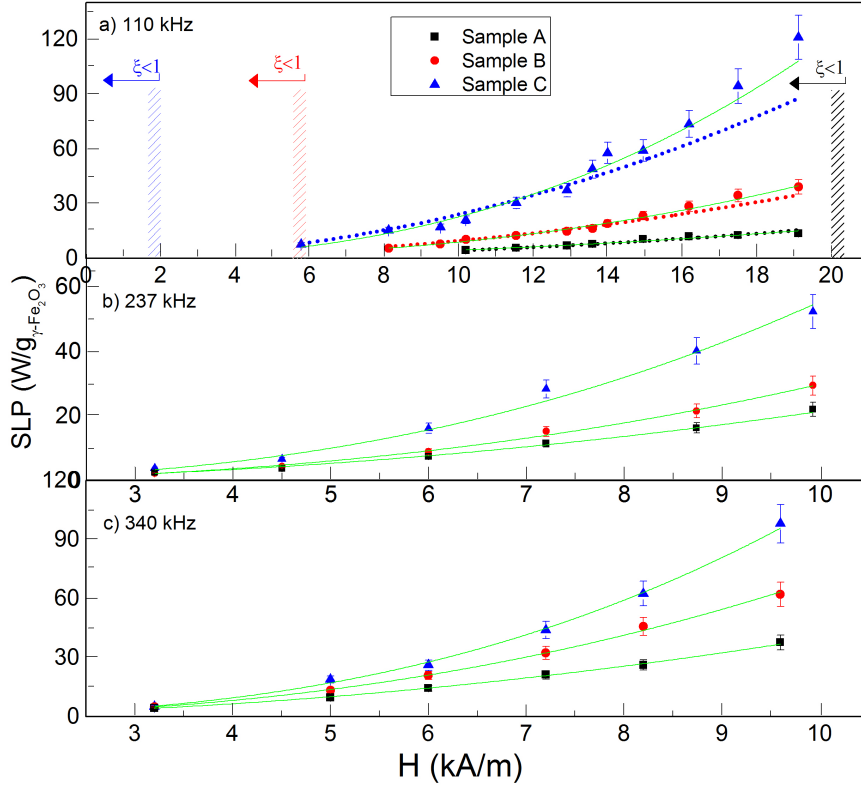
Figure 3.10: Fit of SLP for three different frequencies: the dotted lines are fits with LRT model, the continuous green line are fits with FEM and the dashed zones are the limit of validity for the LRT model ($\xi < 1$).

approximation, τ_B is independent from measurements condition (field and frequency) and is affected only by the properties of nanoparticles (anisotropy constant and volume).

For sample A, the estimated value of τ_{eff} from eq. (1.13) is $\tau_{eff} = 19.5 \pm 2.3$ ns while the experimental time obtained from eq. (3.11) is $\tau_{eff} = 17.6 \pm 2.5$ ns. The same argument and calculation can be used for sample B for the first point (under 6 kA/m), where the exponent of FEM model is $\simeq 2$. In these cases τ_{eff} is not dominated by Néel mechanism but has a relevant contribution from the Brown component. The τ_{eff} obtained is 340 ± 30 ns while from eq. (1.13) one extracts $\tau_{eff} = 470 \pm 20$.

The results present a good agreement of τ_{eff} obtained from eq. (1.13) and from eq. (3.11) for sample A, confirming the efficacy of LRT to describe the SLP for superparamagnetic nanoparticles. On the other hand, for sample B the two values have the same order of magnitude, a very good result considering that the LRT model is satisfied just in some cases.

For sample C, it was impossible to use the LRT model because the FEM exponent assumes an average value of 2.5.
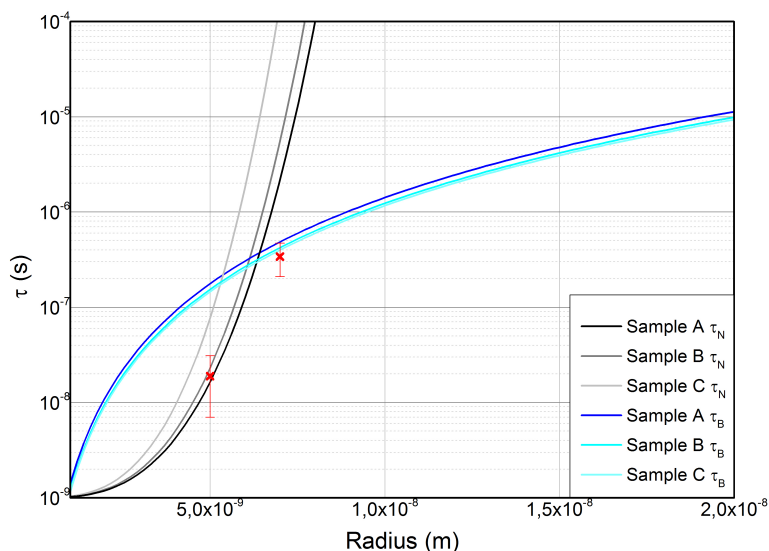
Figure 3.11: Characteristic times of magnetic moment dynamics as a function of particle radius. The Néel time depends exponentially on magnetic anisotropy and particle volume, whereas Brownian time varies linearly with particle volume and solvent viscosity. The red points are the values of relaxation time obtained from fits.

3.6 NMR Core Effect

The samples for NMR relaxivity experiment were diluted more than the ones for hyperthermia measurements and all the results were normalized to the concentration of iron oxide in order to compare different nanoparticles. The relaxivity (longitudinal and transversal) is defined by the formula:

$$r_i = \frac{(1/T_i)_{meas} - (1/T_i)_{ref}}{C} \quad i = 1, 2 \tag{3.12}$$

where C is the magnetic center concentration, $(1/T_i)_{meas}$ and $(1/T_i)_{ref}$ are, respectively, the characteristic the proton relaxation rate of a solution containing the nanoparticles and the relaxation rate of the reference pure water. The relaxivity is measured in $s^{-1}mM^{-1}$ (millimolar).

The analysis of the experimental data shows: (a) a relaxation efficiency increasing with the volume, as demonstrated in literature [19]; (b) the values of the transversal relaxivity overcome the commercial ENDOREM commonly used in hospital as MRI contrast agent; (c) moreover all samples present a r_1 comparable to r_2 at low field, as predicted by Roch's theory of superparamagnetic relaxation.

From r_1 fits, the values of r_D, τ_N, P (see par 2.2.2) listed in Table (3.6) were obtained. The Néel relaxation time increases with the dimensions but it was impossible to evaluate it for sample C (the value results too high, as expected from Fig. (3.11), where it can be noted that the dominant mechanism for C is
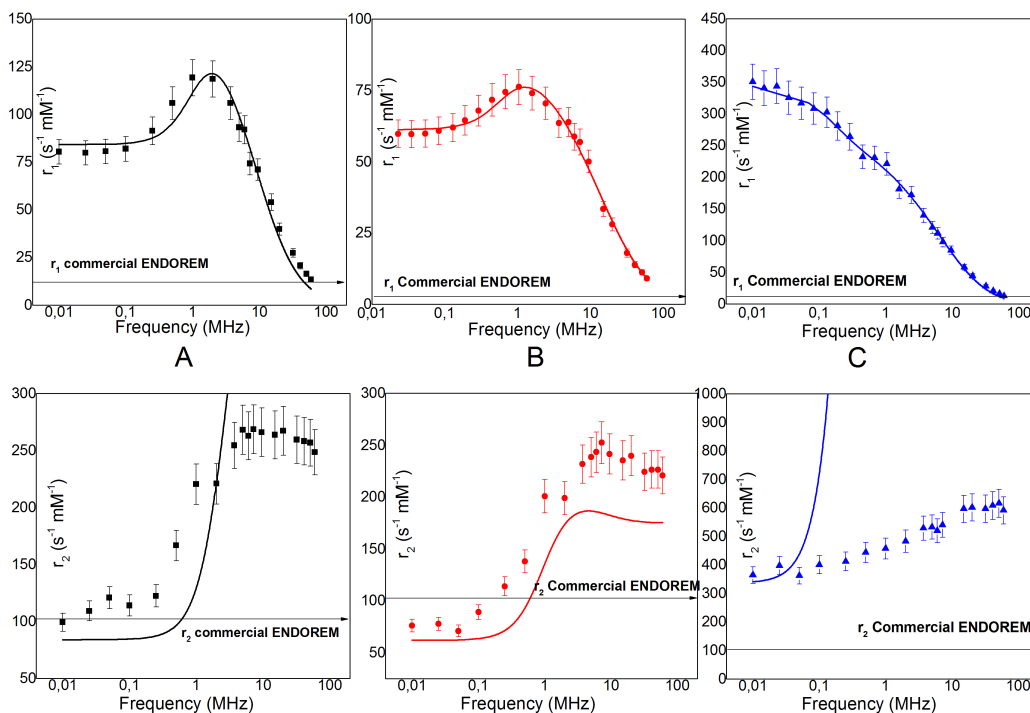
Figure 3.12: Longitudinal (top) and transversal (bottom) relaxivity experimental data of the nanoparticles used, fitted with RMG model (2.30); from left to right the results for samples A, B, C are displayed.

Brown).

The same trend is shown by the parameter P, meaning that the energy barrier is higher for C compare to the other two samples.

Regarding transversal relaxation, the experimental data show some discrepancies with the theoretical curves obtained by using the same fit parameters values extracted from the fitting of r_1: the r_2 theoretical curves do not reproduce the experimental data, except for sample B. The lack of efficiency of Roch model for r_2 is shown in different works [64, 65] and can be due to unknown physical mechanisms, as interaction between MNPs, chemical exchange with the water molecule of the bulk or dipole-dipole nuclear interaction.

3.7 Conclusions

The effect of the size of magnetic nanoparticles based on maghemite iron-oxide on SLP and NMR relaxivity was studied by investigating three distinct samples having 10, 14 and 20 nm of core diameter.

The magnetic properties of the particles were examined by means of DC susceptibility measurements. These measurements confirmed the superparamagnetic properties of all samples at room temperature and very narrow hysteresis loops at 5 K, in particular for the biggest NPs. The saturation magne-

Sample	r_D (nm)	τ_N (ns)	P
A	8.0 ± 2.0	1.9 ± 0.4	0.7 ± 0.1
B	7.6 ± 0.3	27.3 ± 0.1	0.1 ± 0.1
C	10.6 ± 0.9	$1 \cdot 10^{10}$	0 ± 0.1

Table 3.6: List of the parameters calculated from the fitting of the longitudinal curves with Roch's model.

tization and the anisotropy constant increase with NPs size, and are close to bulk values.

By differentiating the difference between FC and ZFC curves, the blocking temperature (which characterizes the blockage of the single particle magnetization) was estimated. The 20 nm sample have the blocking temperature above room temperature.

For measuring the MFH efficacy the NPs were located in a AC magnetic field of intensity from 17 to 4 kA/m, in a range of frequency from 100 to 900 kHz. Using the models nowadays present in literature, in particular the LRT model, the superparamagnetism of the smallest sample (10 nm) was confirmed, while for the other two samples the data acquired are out of the limit ($\lessgtr \xi$) of LRT model and also of the Stoner-Wolhfarth condition (H applied higher than coercive field). The model used to fit the data is similar to the Rayleigh model ($\propto H^3$) but with a free exponential, i.e. $SLP \propto H^x$.

The results show an exponent x that increases with the core dimension and field (from x=2 to 3), meaning that the samples are in a transition zone between superparamagnetic and ferromagnetic phases.

The dominant relaxation mechanism was estimated: for sample A τ_N dominates; for sample B τ_N dominates but it was impossible to compare the predicted value with experimental data as B does not follow the LRT model and consequently τ_N cannot be deduced from χ''; for sample C the Brownian motion dominates.

The NMR measurements show "good" values of the r_1 relaxivity rate and using the RMG model it was possible to evaluate the Néel relaxation times, that are of the same order of magnitude of theoretical predictions.

Chapter 4

Coating Effects in Nanoparticles

The superparamagnetic nanoparticles are highly useful in biomedicine for various applications, mainly therapy, diagnosis, tumour imaging and, in a near future, for drug delivery [66, 67]. The colloid stability and the biocompatibility of magnetic nanoparticles are greatly influenced by their surface properties. Thus the surface modification plays an essential role in determining the success of nanoparticles' application in biomedical area because it can improve the stability, the biocompatibility, can provide additional functionalities, increases the circulation in blood stream and the interactions with different cells, and influences their distribution in living tissues [68]. For these reasons, iron oxide nanoparticles need to have chemical and biological stability [69]: by means of an appropriate coating. Since the effect of the coating on the magnetic properties was not systematically analysed, in this chapter we report the coating effect on the magnetic and heat dissipation properties of surface-coated Fe_3O_4 nanoparticles. The organic coatings selected are the most commonly used for biomedical application.

4.1   Synthesis Methods

The MNPs synthesized for studying the coating effect, were developed according to the method of alkaline hydrolysis of Fe(II) and Fe(III) salts [70] by Dr. Erzsebeth Illes at the Vinca Institute of Nuclear Sciences in Belgrade. Since under atmospheric conditions the presence of oxygen enhances the oxidation processes, 10% excess of Fe(II) salt was used during the synthesis in order to maintain the stoichiometric Fe^{3+}/Fe^{2+} ratio for magnetite (Fe_3O_4) formation. The applied purification procedure (dialysis, hydrothermal ageing) involved magnetic separation as well, and resulted in moderate polydisperse iron oxide samples. The coated samples (PAA@MNP, PGA@MNP, OAOA@MNP and PEG-OAOA@MNP) were prepared by absorption/post-coating procedure using the calculated amount of the coating. During the studies 1 mmol PAA, 1 mmol PGA, 2 mmol OA and 5 mmol PEG was used to coat 1 g of MNP.

In the case of PEG-OAOA sample, the coating layer was prepared in two steps: first, oleate covered (surfacted) maghemite nanoparticles were synthesized, then PEG molecules were attached to the surfacted nanomagnets. After these steps, the oleic acid was added to the nanoparticles synthesis obtained after the precipitation of ferrite. The pH in this case is basic and the oleic acid dissociates forming oleate anions that cover the nanoparticles surface: however the resulting NPs are hydrophobic. The second OA layer was adsorbed via hydrophobic interaction and make the surface hydrophilic. The dissociated carboxylate groups of the oleate coating create a negative charge of the surface on the coated nanoparticles.

The PGA coated nanoparticles, instead, were prepared starting from maghemite dispersion adjusted with GA (Gallic Acid) to obtain a concentration of 0.6 mmol GalicAcid per gram of maghemite. The sample was stored for 5 week at 4 °C to obtain a layer of PolyGallyc Acid [71].
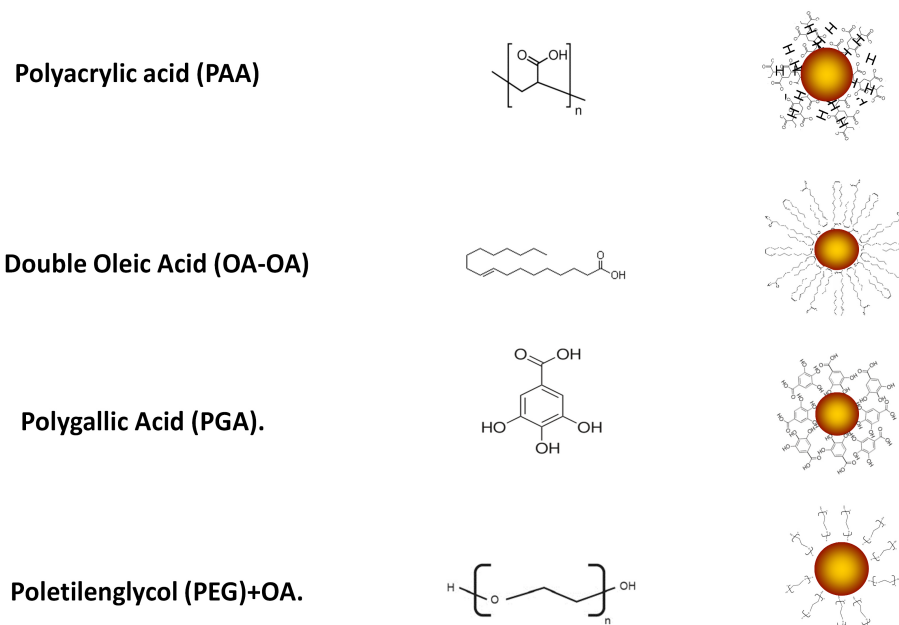
Polyacrylic acid (PAA)

Double Oleic Acid (OA-OA)

Polygallic Acid (PGA).

Poletilenglycol (PEG)+OA.

Figure 4.1: Schematic presentation of chemical moieties used to cover the nanoparticles.

4.2 Morphological structure

As in the previous chapter, where three samples of different diameters were studied, in this chapter five samples with different coatings are analysed. The starting procedure was a morphologically study to be sure that the magnetic part is the same and just the coating is changed. In fact, the aim of the work
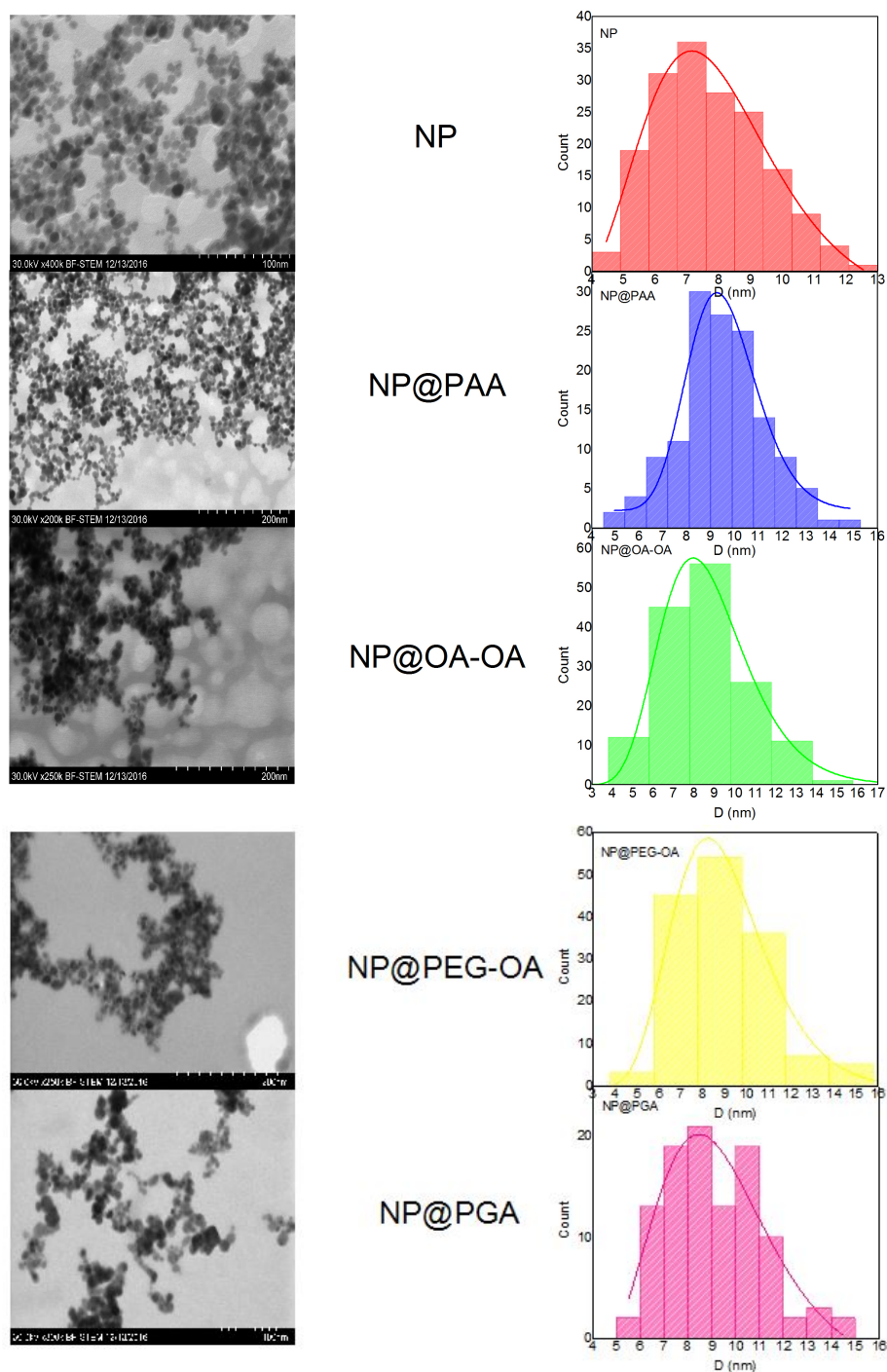
Figure 4.2: TEM images of nanoparticles with different coatings (left) and distribution of the size fitted with LogNormal distribution fit (right).

is to evaluate the variations in SLP for NPs with identical core but different coating.

All the particles have an average core size around 8.5 nm. The narrow distribution is shown in Fig. (4.2). The thickness of the different coatings has

been also evaluated, to be sure they have almost the same values.

The particles can be described in terms of circularity, by using the typical expression:

$$C = 4\pi \frac{A}{P^2} \tag{4.1}$$

A and P are the area and the perimeter of NPs given for spherical shape. This parameter is useful to define the deviation from a perfect spherical shape ($C = 1$). Lower values of C describe square, triangular or more complex shapes [72, 73]. The circularity distributions present peaks around 0.94 (see Fig. (4.3)), meaning that the samples present a very good spherical shape.
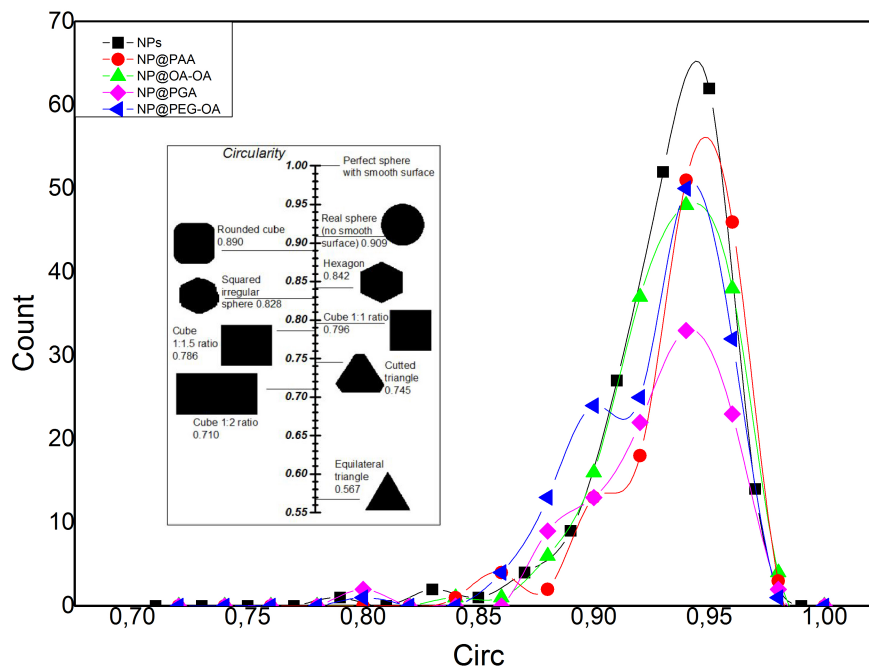

Figure 4.3: Circularity distributions. In the inset, some examples of shapes and the effective results obtained through analysis of the circularity are shown.

The crystal structure of bare NPs has been studied by X-ray diffractometry; the spectra are shown in fig. (4.4). The spectra are characteristic of maghemite.

Hydrodynamic mean size of the particles before and after coating/adsorption was evaluated at the Vincã Institute in Belgrade by dynamic light scattering method (DLS) using a Nano ZS apparatus (Malvern) equipped with a He-Ne laser ($\lambda = 633$ nm, max 5 mW) and operated at a scattering angle of 173°. In all measurements, 1 mL of particle suspension was employed and placed in a 10 mm per 10 mm quartz cuvette. The average particle size of bare maghemite and coated nanoparticles were determined at 25 ± 0.1℃. The aggregation state of the bare and the coated nanoparticles in the aqueous dispersions was characterized by changes in the intensity average values (Z-Ave) of the hydrodynamic
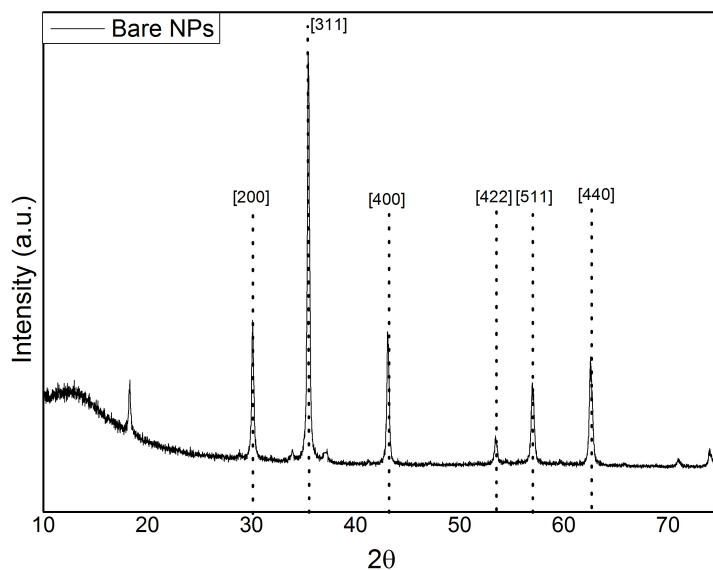
Figure 4.4: X-Ray diffractogram of bare NPs.

diameter. The dispersions were diluted (0.1 g/L) to give an optimal intensity of ∼105 counts per second. Measurements were performed in water, and 0.1 mL of HCl and NaOH were used to adjust the pH of the sample in the range from ∼2 up to ∼11. Before the measurements, the samples were homogenized in an ultrasonic bath for 10 s and the data recording started 2 min later to ensure the same kinetic state.

The DLS technique in some cases can overestimate the hydrodynamic sizes of the NPs because also the presence of aggregates are taken into account. On the other hand, one of the most accurate techniques to evaluate the thickness of coating is the Atomic Force Microscope (AFM). The instrument used is the same presented in the previous chapter and in the appendix.

For samples @PAA and @PGA the coating thickness results less than 1 nm while for @OA-OA and @PEG-OA the values is higher ($\simeq 2$) (Fig. (4.5)). The variability of the coating thickness is related to the different amount of material bound to the surface during the synthesis and to the possible influence of the pH of the suspension [74, 75, 76].

The ThermoGravimetric Analysis (TGA) for NPs (performed at University of Genoa) showed two different weight losses respectively in the range $100 - 550$ °C and $550 - 1000$ °C (see Fig. (4.6) and Fig. (4.7)). The global variation of the weight was of -6.23%. The contemporary mass spectrometry investigation revealed the release of molecules whose main peak corresponds to the fragment m/z = 44. The most reasonable species that can be associated is CO_2, even if the propane (C_3H_8) possesses the same molar mass. Indeed, the real origin of this decomposition step is still unclear, even if a possible correlation with some chemicals used during the synthesis, which remains entrapped or bonded to the nanoparticles, appears the most reasonable explanation.

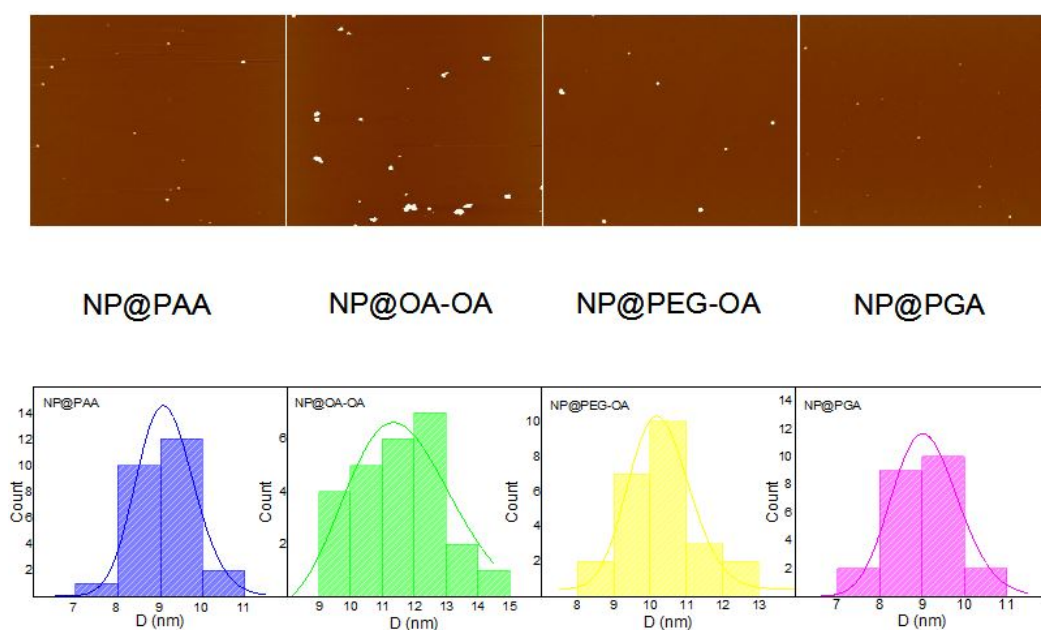The TGA curve for NP@PAA identified three different decomposition steps

Figure 4.5: AFM images (top) and size distributions (bottom).

at 50 – 450 ℃, 450 – 750 ℃, 750 – 1000 ℃ respectively. During the first mass loss the fragments respectively at m/z = 44, and in the range 10 – 42; 55 – 105 were identified. As previously reported for the PAA analysis, they are associated to the polymer which first releases CO_2 (m/z = 44) and then splits the long chain. It is note to worth that the same behaviour was measured for the PAA, demonstrating the presence of the polymer in the analysed sample. What occurs during the second and third step is more difficult to interpret even in the reasonable hypothesis that the organic ligand has a role. In fact, the pure nanoparticles don't present the same behaviour of NP@PAA. Hence, the m/z = 44 could be associated with the propane, probably strongly bonded on the NP surface. Another possible explanation is the detrapping of molecules confined by the formation of NP agglomerates.

The percentage of organic coating was calculated considering the mass variation of MNP and PAA. The value should be considered as an estimation due to the fact that PAA can possess a different behaviour if free of bonds.

In Table (4.1) the mass losses expressed as the variation with respect to the initial weights are reported, while in Table (4.2) the dimensions of the MNPs obtained with different methodologies are displayed.

4.3   Magnetic Properties

The magnetic properties of bare and coated NPs were investigated with a SQUID magnetometer, equipped with a superconducting coil which produces magnetic fields from -5 T up to +5 T, at The Vinca Institute of Nuclear Sciences in Belgrade. The ferrofluid samples were poured to the capsules and

Sample	Mass variation (%)	Initial weight (mg)	Coating (%)
NP	-6.23	6.0	/
$NP@PAA$	-16.6	5.9	20

Table 4.1: Variation in mass for naked NPs and coated nanoparticles obtained from TGA.

Sample	$< D_{TEM} >$ (nm)	$< D_{AFM} >$ (nm)	$Z - AVE$ (nm)	PDI
MNP	7.45 ± 0.19	/	100	0.15
$@OA-OA$	8.26 ± 0.15	11.6 ± 1.3	115-120	0.13
$@PAA$	8.71 ± 0.16	9.2 ± 0.6	140	<0.2
$@PEG-OA$	8.55 ± 0.18	10.4 ± 1.0	120-130	<0.2
$@PGA$	8.80 ± 0.22	9.0 ± 0.7	170	0.16

Table 4.2: Mean diameter obtained from TEM, AFM and DLS. The PDI correspond to the PolyDisperity Index: it is dimensionless value and scaled such that values smaller than 0.05 are rarely seen other than with highly monodisperse standards. Values greater than 0.7 indicate that the sample has a very broad size distribution.

Sample	T_{max} (K)	T_{irr} (K)	T_B (K)	E_B/k_B (K)
MNP	162	>250	63	1449±21
$@OA-OA$	232	>250	97.3	2238±35
$@PAA$	228	>250	98.8	2272±41
$@PEG-OA$	228	>250	97.8	2249±37
$@PGA$	221	>250	2176±28	

Table 4.3: Maximum, irreversible, blocking temperatures and barriers of nanoparticles obtained from analysis with different techniques and the same data obtained from differentiation of (ZFC-FC) data.
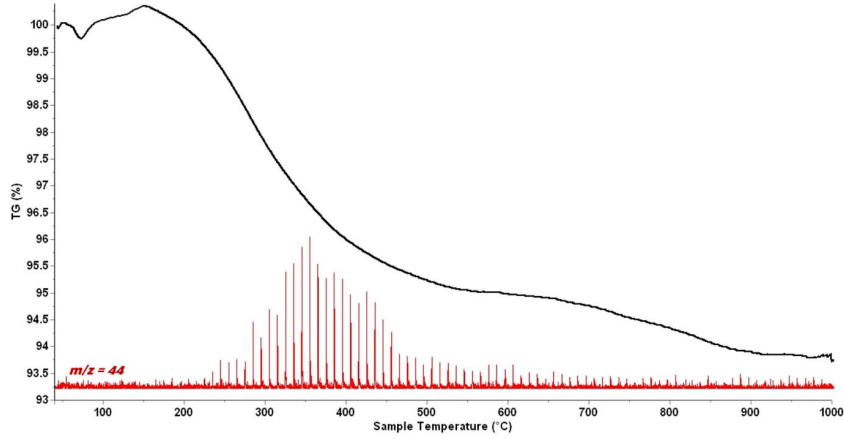
Figure 4.6: TGA analysis for naked nanoparticle. The TGA curve shows that for the naked particles the weight loss over the temperature range from 10 to 800 °C is about 6% of the total weight.

fixed with epoxy resin, to prevent any movement during the measurements; then they were frozen in freezer. Magnetization versus temperature measurements were performed using the zero-field-cooled (ZFC) and field-cooled (FC) methods. Zero field-cooled and field-cooled magnetization measurements were carried out by cooling the sample from 250 K to 5 K in zero magnetic field; then a static magnetic field of 2.5 mT was applied. M_{ZFC} was measured during warming up from 5 to 250 K, whereas M_{FC} was recorded during the subsequent cooling.

The progressive increase of the FC curve for temperatures below T_{max} indicates the absence of relevant dipolar interactions, suggesting that they are largely reduced due to the coating taking the particles apart from each other (Figure (4.8)). We note that, for the coated samples, T_{max} is already well above room temperature, except for bare NPs.

The ZFC-FC curves show high values of the blocking temperature (T_B) for the naked particles, while T_B is around 97 K for all the coated MNPs. The evaluation of blocking temperatures were obtained by subtracting ZFC to FC data and subsequently derivating the resulting curves (fig. (4.9))[77].

The effective magnetic anisotropy energy distribution can be written as:

$$f(T) \propto -\frac{dM_{FC-ZFC}}{dT} \tag{4.2}$$

We can define a temperature T_1 where the thermal energy allows a fraction of particles to overcome the anisotropy energy barrier and have a superparamagnetic behaviour. At that temperature, the ratio between superparamagnetic (unblocked) and blocked particles is [78]:

$$\frac{N_{Unblock}}{N_{Block}} = \frac{\int_{T_1}^{T_{max}} f(T)dT}{\int_{T_{min}}^{T_1} f(T)dT} \tag{4.3}$$
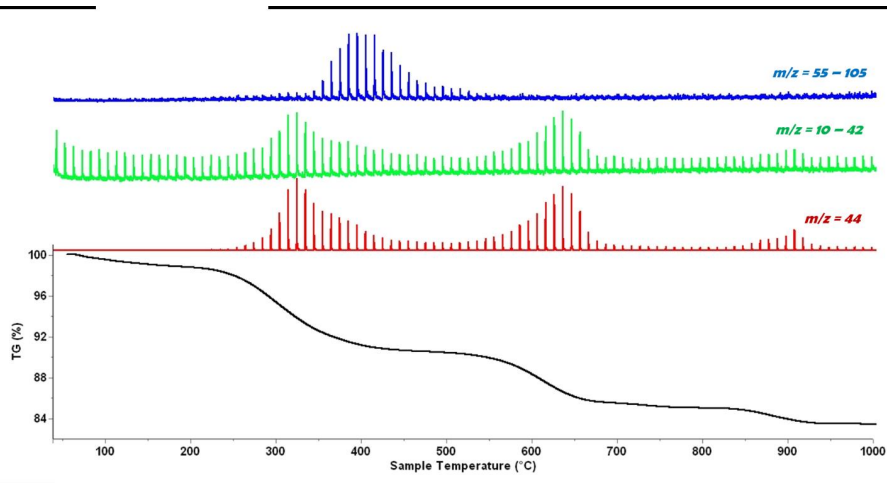
Figure 4.7: TGA analysis for coated nanoparticle. The content of the maghemite particles in the final structures was estimated to be about 84 wt%

where T_{max} and T_{min} are the maximum and minimum temperatures covered during the measure.

According to these two equations, when the ratio is equal to 1 the derivative of the difference FC-ZFC reaches 50% of its maximum; in other words half of the particles are blocked and half not: so we can consider this temperature as the average blocking temperature of the sample.

The associated energy barrier normalized to the Boltzmann constant can be calculated with:

$$\frac{E_B}{k_B} = T_B \ln\left(\frac{\tau_m}{\tau_0}\right) \tag{4.4}$$

where τ_m is the measuring time (10 s) and τ_0 is an attempt time of the order of 10^{-9} s.

As one can see in Fig. (4.9), all the NPs present a "shoulder" for $T < T_{max}$ that reflects the presence of two spin populations with different behaviour. These two populations are independent and can be identified as bulk and surface spins though the fitting by means of a sum of two distributions Fig. (4.10).

This double distributions can be extrapolate by using two different blocking temperatures and two different energy barriers (see Table 4.3).

All samples show different magnetic saturation: for @PEG-OA and @OA-OA M_S is around 60 Am^{2}kg^{-1}, while coated and naked nanoparticles have M_S values close to 72 Am^{2}kg^{-1} (the pure bulk value is 90 Am^{2}kg^{-1}) [79]. The differences in saturation are due to the spin canting caused by coating on a different diameter of magnetic core, and have a fundamental role in hyperthermia results (see next sections).

The coercive fields are similar, meaning that the interaction between nanopar-
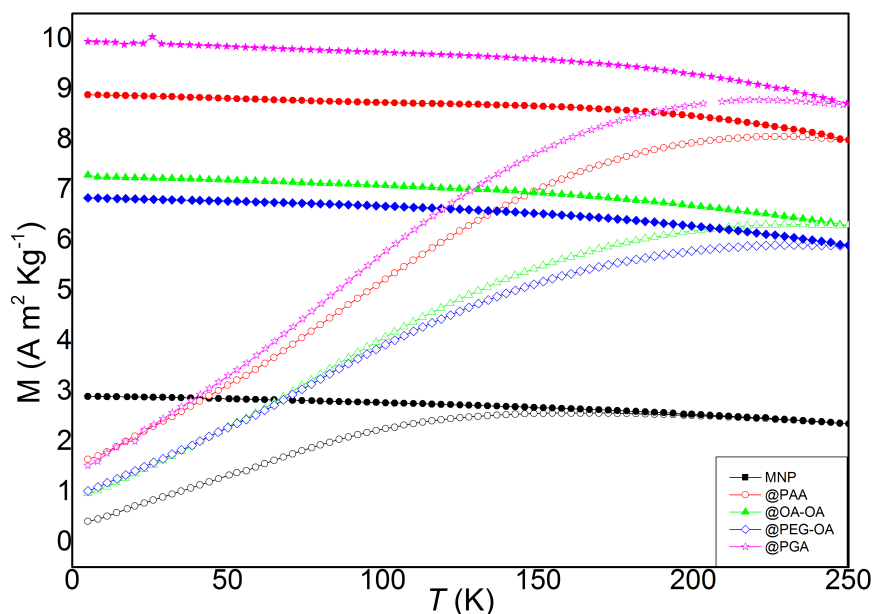
Figure 4.8: ZFC (empty symbols) and FC (full symbols) curves, at an applied field of 50 Oe.

ticles are very similar. The ratio between M_R and M_S indicates a tendency towards a magnetic anisotropy with uniaxial symmetry [80, 81]. In Table (4.4) their values are reported.

4.3.1 Interaction Between MNPs

Other protocols used to study the residual magnetizations are the Isothermal Remanent Magnetization (IRM) and the Direct Current Demagnetization (DCD).

The IRM curves are performed starting from a totally demagnetized state obtained on cooling in zero field at 5 K: after this cooling a small external posi-

Sample	T_{B1} (K)	E_{B1}/k_B (K)	T_{B2} (K)	E_{B2}/k_B (K)
MNP	40	920 ± 18	65	1495 ± 19
$@OA - OA$	22	506 ± 14	79	1817 ± 20
$@PAA$	12	276 ± 10	88	2024 ± 22
$@PEG - OA$	34	782 ± 18	97.8	2249 ± 37
$@PGA$	17	291 ± 12	84	1932 ± 22

Table 4.4: Dimensions of nanoparticles analysed with different technique and the specific temperature obtained from ZFC-FC curves.

Sample	M_S (emu/g)	M_R (emu/g)	H_C (mT)
MNP	72.6 ± 0.2	20.9	32
$@OA - OA$	60.3 ± 0.6	18.3	35.1
$@PAA$	72.5 ± 0.2	22.8	36.1
$@PEG - OA$	57.6 ± 0.2	17.6	33.5
$@PGA$	72.1 ± 0.1	22.9	32.0
Sample	H_K (mT)	M_R/M_S	χ_d ($\cdot 10^{-5}$ emu/g)
MNP	0.19 ± 0.04	0.334	2.0 ± 0.3
$@OA - OA$	0.21 ± 0.07	0.306	8.5 ± 0.2
$@PAA$	0.25 ± 0.01	0.317	3.6 ± 0.2
$@PEG - OA$	0.20 ± 0.09	0.316	7.7 ± 0.2
$@PGA$	0.26 ± 0.05	0.302	2.7 ± 0.3
Sample	K_{eff} ($\cdot 10^4$ J/m^3)	H_{int} (mT)	
MNP	2.87 ± 0.05	-8.5	
$@OA - OA$	3.27 ± 0.06		
$@PAA$	4.72 ± 0.05	-10.9	
$@PEG - OA$	2.88 ± 0.07	-22.6	
$@PGA$	5.04 ± 0.01		

Table 4.5: Magnetic features of nanoparticles: M_S is the magnetic saturation, M_R the residual magnetization, H_C the coercive field, H_K the anisotropy, χ_d the high field susceptibility evaluated for data over 1 T, K_{eff} the anisotropy constant, H_{int} the irreversibility field.
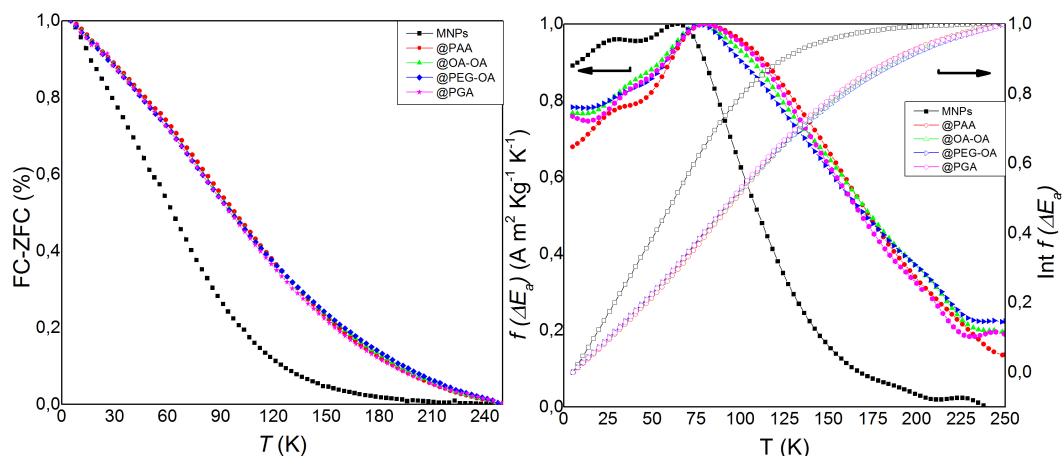
Figure 4.9: Left panel reports the FC-ZFC subtracted data (in percentage) and the right panel reports the derivative (left abscissa) and integral (right abscissa) curves. The blocking temperatures have been extrapolated at 0.5, where half of NPs are in superparamagnetic state and half are blocked.

tive field is applied for a short time (e.g. 10 s) and the remanent magnetization M^{IRM} is measured. The process is repeated increasing the field step by step until the sample reaches the saturation and the remanence has the saturation value.

In DCD measurement the initial state is completely saturated, then a small external field in the opposite direction of magnetization is applied and, after a short time it is switched off and is recorded the M^{DCD}. This is repeated increasing the field until saturation in opposite direction is reached.

Differentiating the M^{DCD} with respect to the field, we obtain the irreversible component of the susceptibility (χ_{irr}): this quantity can be considered as a measure of the distribution of energy barriers which, for the nanoparticles, is associated with the distribution of particles' coercive field and it is called the switching field distribution [82, 80].

For an assembly of single-domain, non-interacting particles with uniaxial anisotropy, the relationship between M^{DCD} and M^{IRM} is known as the Stoner-Wohlfarth relation, given by [83]:

$$m^{DCD}(H) = 1 - 2m^{IRM}(H) \tag{4.5}$$

where $m^{DCD}(H)$ and $m^{IRM}(H)$ denote the reduced terms $M^{DCD}(H)/M^{DCD}(\infty)$ and $M^{IRM}(H)/M^{IRM}(\infty)$, respectively. Instead of this equation we can use another function, called Henkel δm curve, given by:

$$\delta m(H) = m^{DCD}(H) - (1 - m^{IRM}(H)) \tag{4.6}$$

This δm curve clearly shows any deviation from the behavior predicted by the Stoner-Wohlfarth relation for non-interacting particles and hence, it is frequently used to evaluate the existence of interactions among single-domain
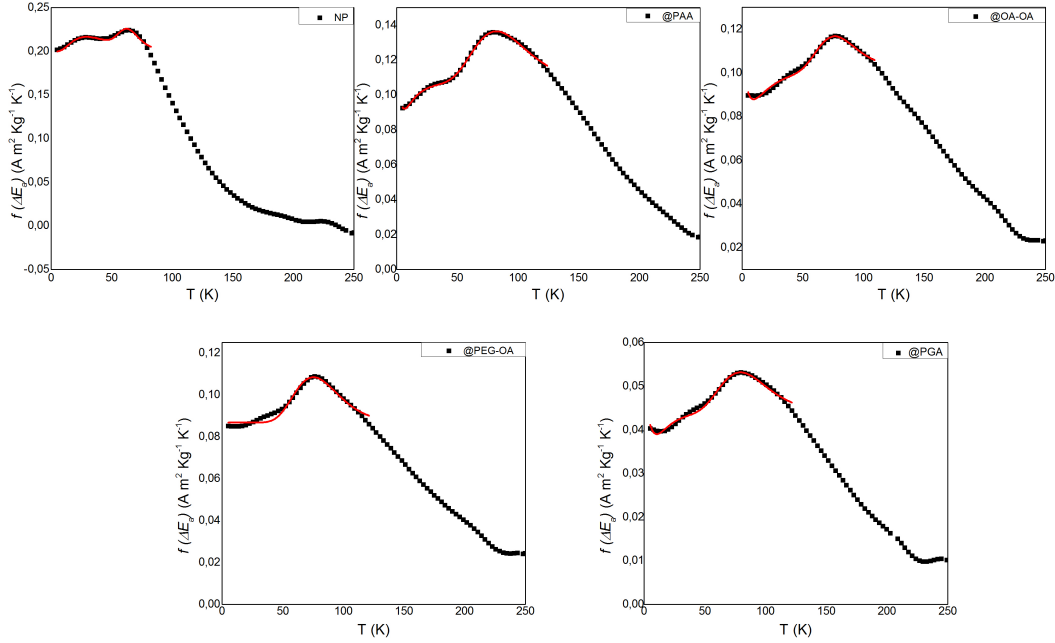
Figure 4.10: Temperature versus derivative of FC-ZFC difference of samples, fitted with a sum of two LogNormal distributions.

and randomly oriented magnetic nanoparticles. Typically, negative δm peaks are associated with demagnetizing magnetostatic (dipolar) interactions and positive peaks are related to exchange interactions [84]. Alternatively, the Wohlfarth relation can be expressed in terms of irreversible susceptibilities as:

$$\left| \frac{dm^{DCD}}{dH} \right| = 2 \frac{dm^{IRM}}{dH} \tag{4.7}$$

From the distance between the δm peaks, we can obtain the mean interaction field. For all samples, H^{DCD} (magnetic field when DCD is equal to zero) is larger than H^{IRM} (magnetic field where IRM have half maximum value), indicating that the dipolar interactions H_{int} have a demagnetizing character. The values of H_{int} is defined by the following expression:

$$H_{int} = \frac{H^{DCD} - H^{IRM}}{2} \tag{4.8}$$

and is reported in Table 4.4 for all samples. It is important to underline that, by this plots analysis, is possible to determine what kind of interaction is predominant and affect the magnetic behaviour of the system. In fact, magnetizing and demagnetizing interactions, are present simultaneously and contribute in an opposite way to the shape of the curve.

The IRM and DCD measurements were performed for naked, @PAA and @PEG-OA (Fig. (4.12)) samples: the interaction field calculated with eq. (4.7) suggests the presence of weak demagnetizing interactions.
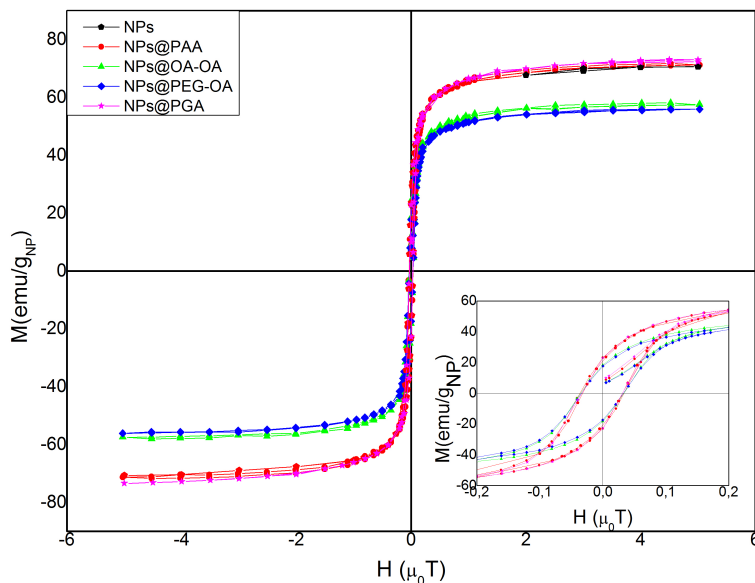
Figure 4.11: Hysteresis loops at 5 K. In the inset are represented the zoom of loops.

The IRM and DCD curves and the related interaction estimations are confirmed by the Henkel plots in Fig. (4.13): the experimental data exhibited a negative deviation originated by the prevalence of dipolar interactions (see the δm plot in Fig. (4.13)). The naked particles present strong interactions compared to the coated ones. In fact the organic shells have a screening effect on the nanoparticles that reduces the dipolar interaction effect.

In a sample containing randomly distributed nanoparticles with an average magnetic moment μ at an average distance d, the energy due to dipole-dipole interactions is evaluated with the relation [85]:

$$E_{dip} \approx \frac{\mu_0}{4\pi} \frac{\mu^2}{d^3} \qquad (4.9)$$

The equation (4.9) is an approximation because it assumes center to center maximum distance (point-dipole model). The mean value of dipolar energy can be calculated using eq. (4.9), defining the magnetic moment μ of a single domain particle as $M_S \times V$.

The energy presents differences between naked and coated particles and also between particles with different coating because the interparticle separation increases with the thickness of the coating.

4.3.2 High Field Susceptibility

In chapter 3 the function to extrapolate the magnetic saturation at high field (eq. (3.4)) was reported. An alternative approach is to consider the contribu-
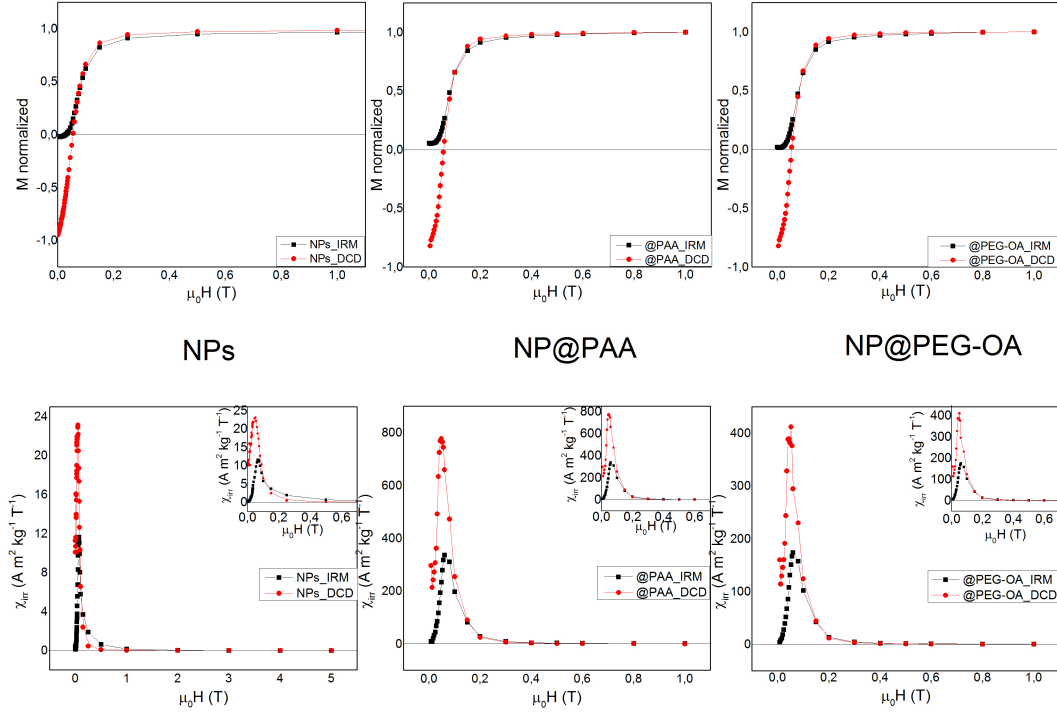
Figure 4.12: IRM and DCD curves for the three samples (above) and the corresponding derivatives curves (below). In the insets a zooms at low fields are shown.

tion of a high field component, which considers the presence of a paramagnetic term [86]:

$$M = M_0 \left(1 - \frac{A}{H} - \frac{B}{H^2} \right) + \chi_d H \tag{4.10}$$

where M_0 represent the spontaneous magnetization and χ_d the susceptibility of spins with paramagnetic behaviour (e.g., canted spins).

In Fig. (4.14) the fits obtained with eq. (4.10) for high field magnetization are shown and the obtained values of χ_d are summarized in table (4.4): the coated NPs having the high saturation magnetization present low value of χ_d susceptibility and, on the other hand, the @OA-OA and @PGA coated NPs show high χ_d. This suggests that the number of canted spins reduces the magnetic moment compared to the bulk structure. These effects indicate that some interactions have been suppressed at the particle surface and consequently the spins near the surface are not collinear, but rather present an angle with the easy magnetization axis.

The presence of canting spins are confirmed by the decrease of the activation volume (see next section).
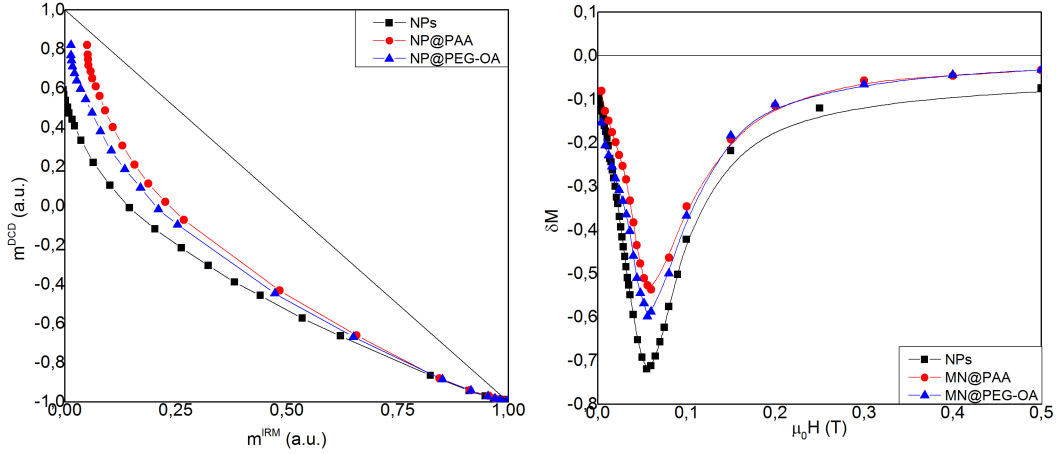
71

Figure 4.13: m_{DCD} and Henkel δM plots. The solid lines are a guide for the eyes.

4.3.3 Activation Volume

A study complementary to IRM and DCD measurements, is the activation volume (V_{act}) analysis. The activation volume is defined as the volume occupied by spins that contributed to overcome the energy barrier (i.e. it is the smallest volume unit able to reverse its magnetization during a switching process)[87].

For a ferrofluid sample, characterized by a distribution of energy barriers, the magnetization as a function of time is characterized by a logarithmic decay:

$$M(t) = M_0 \pm S \ln\left(\frac{t}{t_0}\right) \tag{4.11}$$

where S is the viscosity coefficient and the signs of the second part describe whether M is increasing or decreasing with time. The parameter S depends on temperature and applied field but also on volume of nanoparticles, interaction and anisotropy field. To evaluate S, the measurements were recorded at 5 K in order to avoid superparamagnetic relaxation. The sample is led to a negative saturation field, then a reverse field is applied and the variation of M is measured as a function of time. This experiment is repeated for different reverse fields (close to the coercive value), in order to determine the maximum value of viscosity (S_{max}).

The fluctuation field (H_f), that describes the effects of thermal activation on the magnetization reversal processes, is obtained from the ratio between the magnetic viscosity and the irreversible susceptibility (χ_{irr}) at the same field and extracted from the DCD curve:

$$H_f = \frac{S_{max}}{\chi_{irr}} \tag{4.12}$$

The fluctuation field can be used to extract V_{act} with the formula [83]:
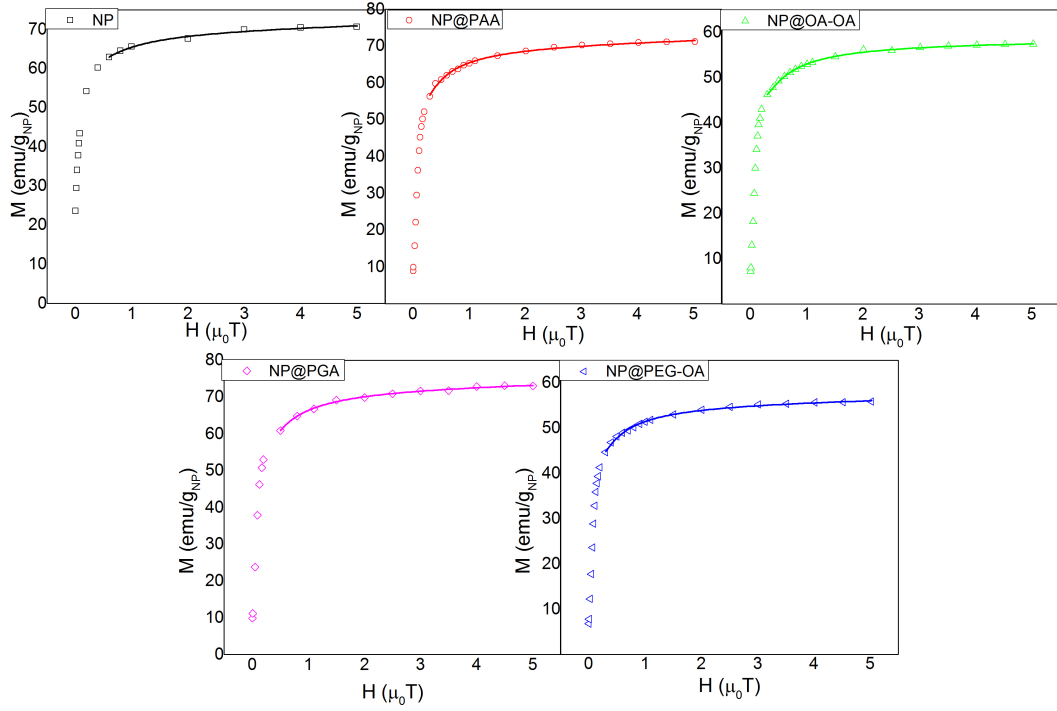
Figure 4.14: Fit of high field magnetization for all samples.

$$V_{act} = \frac{k_B T}{M_S H_f} \tag{4.13}$$

From H_f obtained at 5 K and the magnetic viscosity (S_{max}, Fig. (4.15)), the activation volumes for naked and PGA coated nanoparticles (which are 157(5) and 288(6) nm^3, respectively, corresponding to diameters 3.35 and 4.0 nm), have been obtained.

Comparing the activation diameters with the same quantities obtained from TEM (see Table (4.2)) we can state that for bare NPs all the spins contributed to the barrier overcome (90% of total volume for a single NP) but only 85% of total volume contribute for sample @PGA.

These results and the values of the susceptibility at high field (χ_d),confirm that, for @OA-OA and @PEG-OA, the contributions of spins to reorientation of magnetization is reduced compared to the other coated NPs.

4.4 Effects of Coating on Hyperthermic Efficacy

The hyperthermic data were collected at The Vinca Institute of Nuclear Science in Belgrade with a Nanoscale system, which allows to select a larger number of field-frequency combinations compare to Nanotherics apparatus. A large
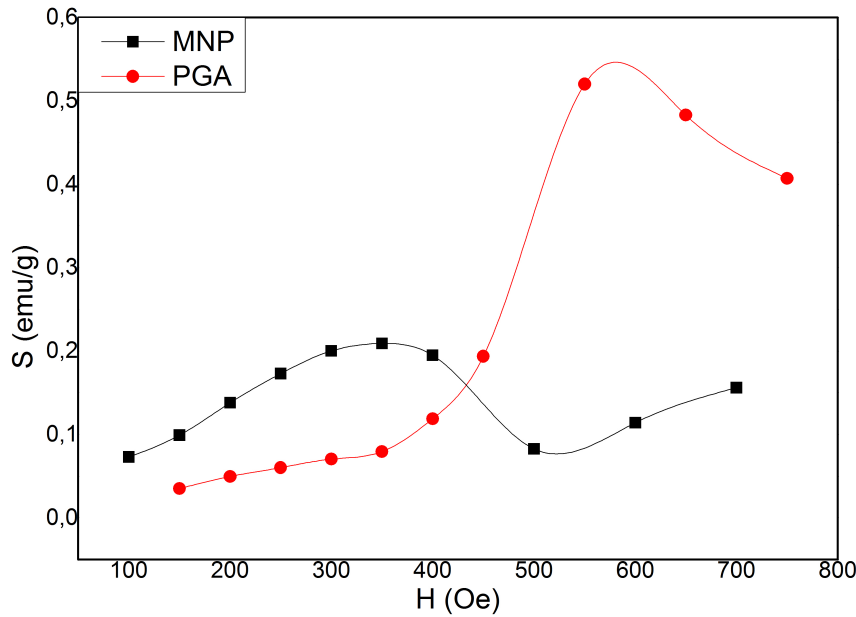
Figure 4.15: Magnetic viscosity coefficient (S) as a function of the reverse field at 5 K.

number of measurements were taken in different conditions, in particular as a function of frequency.

The heating curves of nanoparticles are shown in Fig. (4.16), where the naked nanoparticles show a temperature increase of 2 ℃ in 20 second, very much larger than the coated samples. This is due to the concentration of the samples: 10 mg/mL of solution for bare NPs and 5 mg/mL of solution for all the others. However the different concentrations don't affect the SLP results.

Additionally the graphs in Fig. (4.16) show that the temperature increment is different for the three coated samples, in particular is higher for @PAA and @PGA than for @OA-OA and @PEG-OA. The SLP was analysed as a function of field amplitude from 5 to 25 kA/m, with a 5 kA/m step as shown in Fig. (4.17). The experimental SLP behaviours have a quadratic dependence of the field amplitude as expected in the LRT framework.

In order to evaluate the accuracy of this type of analysis the limit values for field to use LRT are reported in Table (4.5).

The maximum intensity of SLP is obtained for @PAA (220 W/g) and @PGA (217 W/g) whereas the naked particles have an SLP of 196 W/g at 728 kHz: this discrepancy is not significant (within error bars). So in this case we can assert that the coating of the NPs doesn't influence the hyperthermic efficiency. On the other hand the maximum SLP for @OA-OA and @PEG-OA is 142 W/g and 154 W/g, respectively. If we compare the samples with high SLP we note that the limit for the LRT model is about 15 kA/m, while for @OA-OA and @PEG-OA is 18 kA/m. This means that when H_0 is higher than 15 kA/m, for the first group of samples the SLP increase is no more propor-
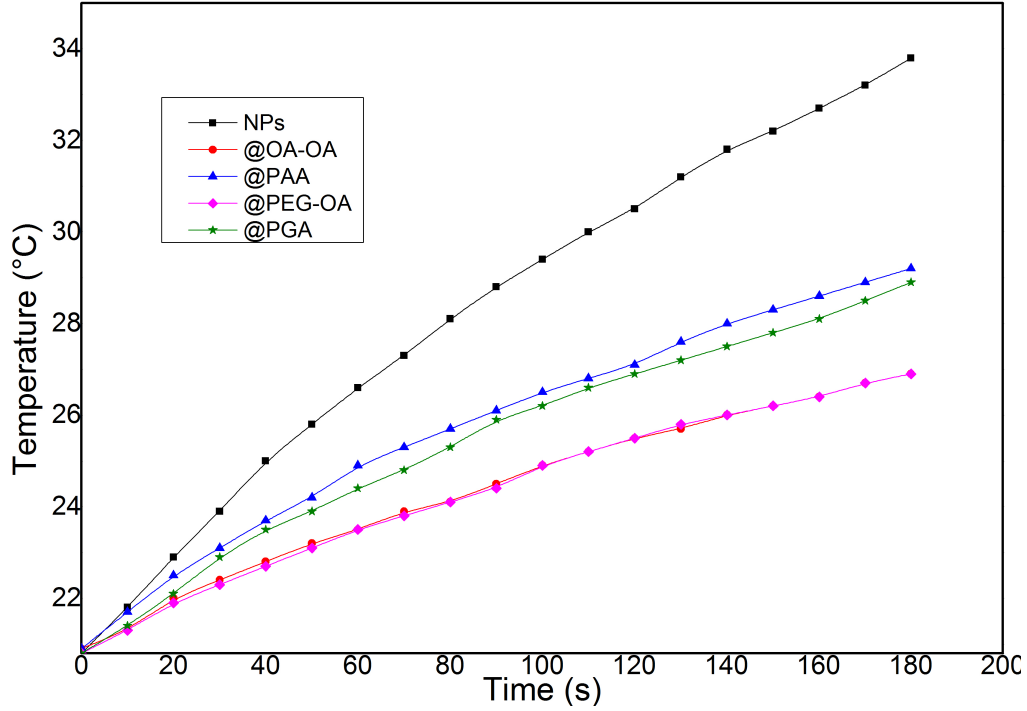
74

Figure 4.16: Heating at 252 kHz and 250 Oe.

tional to H^2 but is proportional at H^x (with x>2) and the increment of SLP is faster than the one observed for @OA-OA and @PEG-OA (SLP proportional to H^2 at 15 kA/m).

For the naked particles, it is important to note that the Néel relaxation is the dominant time; for the coated samples the relaxation times assume values of the same order of magnitude, and $\tau_N << \tau_B$. From fit with LRT function, we have extracted the relaxation times and we can observe that are coherent with the aspect results, so the LRT model used to describe the SLP results is correct.

For the bare NPs the dominant time is pure Néel relaxation time. For the coated samples, the presence of coating gives a big hydrodynamic volume that increases the Brown relaxation time; so in these cases the relaxation time is a combination of τ_N and τ_B (see Table 4.5).

In order to evaluate the relationship between the SLP and the magnetic field another important parameter has been used: the Intrinsic Loss Power (ILP).

The results of ILP are shown in Fig.(4.18). All the samples present, as a function of the magnetic field, a similar behaviour, despite the applied field is low and the systems are in non-adiabatic regime (as in our case) it was not possible to distinguish which contribution to the heating comes from field and which from environment. However the data present good agreement with LRT model ($SLP \propto H^2$). The range of ILP variation is 0.4 nHm^2/kg for all samples.
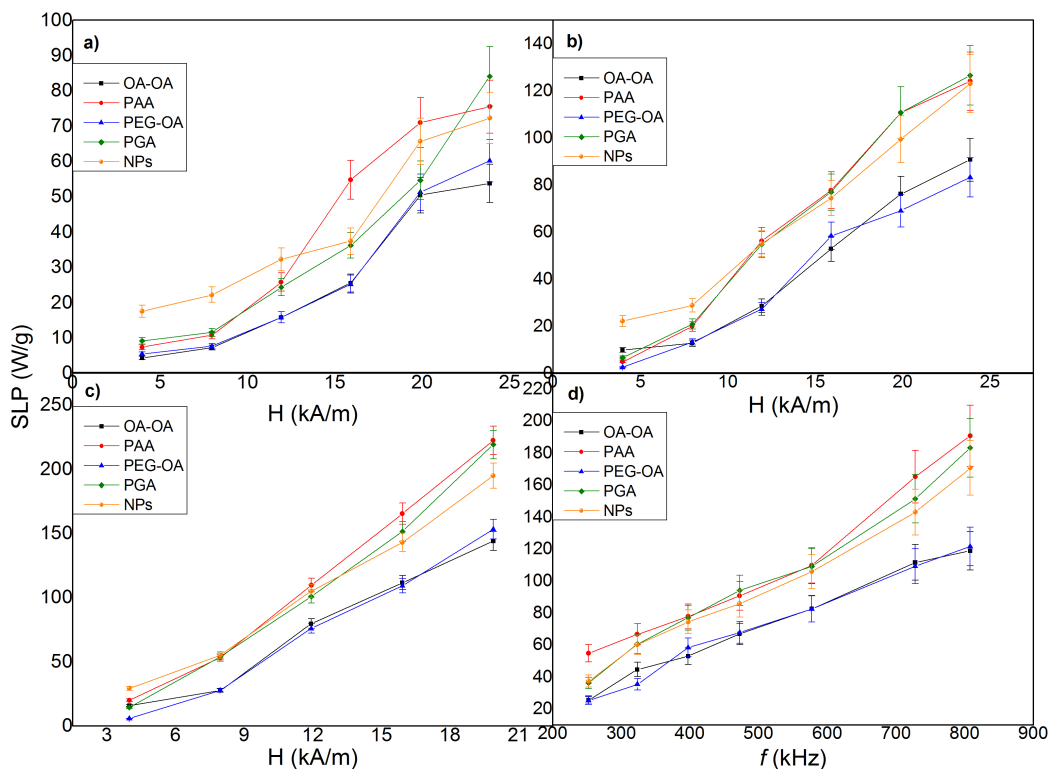
Figure 4.17: SLP as a function of the magnetic field at 252 kHz (a), 397 kHz (b) and 728 kHz (c). SLP at 200 Oe as a function of frequency (d).

From literature, ILP values for commercial ferrofluids have been reported in the range 0.2-3.1 nHm^2/kg [88]. The superparamagnetic features of nanoparticles are confirmed by ILP data as a function of H, see Fig. (4.18): the ILP is approximately constant meaning that it has a squared dependence from field, and a linear dependence from frequency, as expected. In our case the samples (bare and coated) present values in this range and can be used for hyperthermia treatments. Not all measurements were below the safe biomedical limit ($5 * 10^9$ A/m·s) [89]. This limit for our particles is 250 Oe for 252 kHz, 157 Oe for 397 kHz and 86 Oe for 728 kHz. However, under these limits, the samples present a significant increment of temperature and high values of SLP.

4.5 NMR results

With NMR analysis is possible to estimate the effect of the coating on the relaxivity.

As explained in chapter 2, the parameters that can be obtained from NMR data fit are: the minimum approach distance r_D (it is influenced by coating that varies the distance between the center of the ferrite nanoparticles and the closest water molecule), the Néel relaxation time τ_N and the factor P.

For the fit we used the magnetic core size r, fixed by TEM measurements,

Sample	H_{max} (kA/m)	τ_N (ns)	τ_B (ms)	τ_{eff} (ns)
MNP	15	46 ± 2	38 ± 2	46
$@OA-OA$	18.5	60 ± 6	61 ± 1	3900
$@PAA$	14	290 ± 40	1.1 ± 0.3	4600
$@PEG-OA$	18	39 ± 6	77 ± 3	4300
$@PGA$	13	600 ± 70	1.9 ± 0.1	8.5

Table 4.6: Magnetic features of nanoparticles: H_{max} is the limit of validity for LRT model, τ_N is the Néel relaxation time, τ_B is the Brown relaxation time and τ_{eff}, obtained from experimental data, is the combination of the two times.
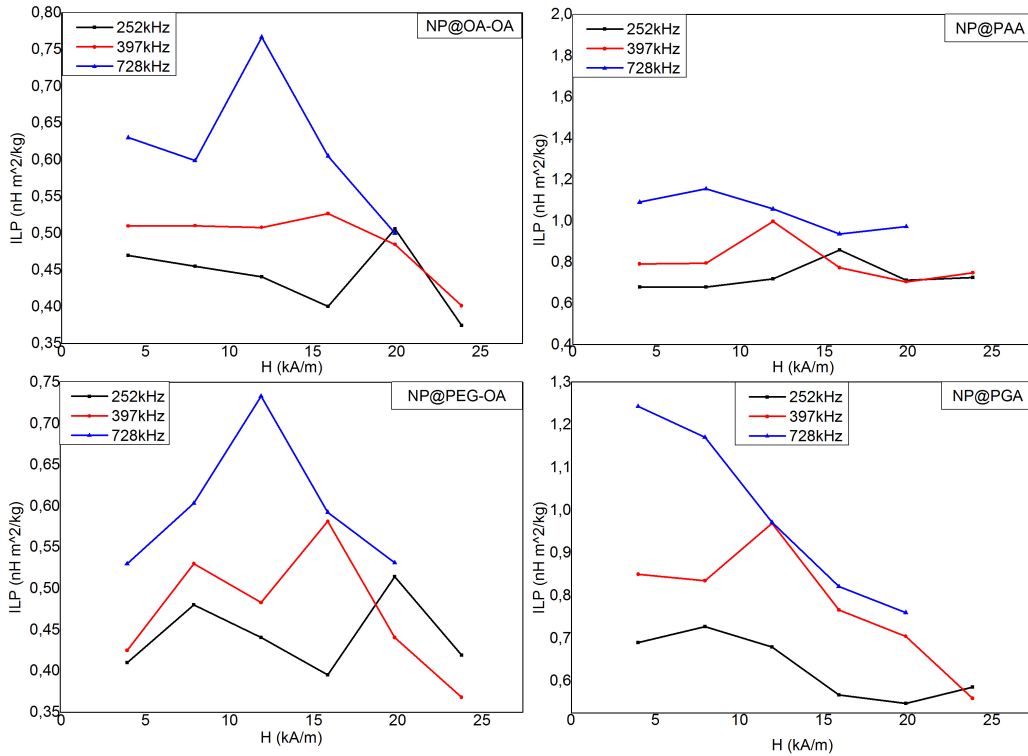

Figure 4.18: ILP results at different frequencies and fields.

Sample	r_{TEM} (nm)	r_{AFM} (nm)	r_D (nm)	τ_N (ns)	P
MNP	3.72 ± 0.09	/	5.1 ± 1.5	29.3 ± 7.1	0.21 ± 0.1
$@OA - OA$	4.13 ± 0.07	5.8 ± 0.05	10.8 ± 0.8	60.8 ± 30	0.68 ± 0.1
$@PAA$	4.35 ± 0.08	4.6 ± 0.3	8.6 ± 0.3	108 ± 68	0.52 ± 0.15
$@PEG - OA$	4.22 ± 0.09	5.2 ± 0.5	10.3 ± 1	39.2 ± 15	0.54 ± 0.06
$@PGA$	4.4 ± 0.11	4.5 ± 0.35	7.1 ± 0.9	262 ± 47	0.51 ± 0.08

Table 4.7: Parameters values used for longitudinal relaxivity: r_{TEM} and r_{AFM} are the radii estimated from TEM and AFM, r_D is the minimum approach radius, τ_N is the Néel relaxation time and P is the relative weight in the linear combination of infinite and zero anisotropy components.

and the magnetic saturation obtained from the hysteresis curves. Another fixed parameter is the characteristic diffusion time of the water $\tau_D = r_D^2/D$, where D is the self diffusion coefficient of the liquid in which the particles are dispersed (for water $D=2.3 \cdot 10^{-9}$ m^2/s at room temperature).

The results of the fit procedure for longitudinal relaxivities of different samples are shown in Fig. (4.19) and the values of the parameters obtained are summarized in Tab. (4.6). The Roch-Muller-Gillis fits well the experimental points, reproducing the relaxometry profile, both when the maximum is well-defined and when there is the typical high anisotropy plateau at low frequency.

The order of magnitude of the Néel relaxation time obtained from the fit is in the typical range of superparamagnetic compounds reversal time (1-1000 ns). These results confirm the superparamagnetic behaviour, previously observed in the SQUID and hyperthermic results.

An interesting result can be noted in the relaxation time: the relaxation is strongly related to the anisotropy energy barrier amplitude. The samples with high anisotropy energy barrier present τ_N slower than the ones having a smaller barrier. In our case the K_{eff} values are very similar, but it is possible to observe that the trend in relaxation times follows the K_{eff} trend (Fig. (4.20)).

P values are very similar for all samples, except for @OA-OA that has a maximum value, in agreement with its low anisotropy energy.

The Roch-Muller-Gillis model is a very good model to study the r_1 fit. The parameters obtained by fitting the longitudinal relaxivity data should fit (within the experimental error) the transverse relaxivity ones.

So the parameters listed in Table (4.6) have been kept constant and the complete transversal relaxivity $r_2(f)$ profile was then superimposed to the experimental data. The @OA-OA sample presents higher value of r_2 than r_1: this is due to the micro-aggregation of nanoparticles (as appears in experimental data) impossible to avoid, even with sonicator. As one can see in Fig. 4.21, the transverse relaxivity model doesn't fit the experimental data, in particular at high frequencies. As already remarked, the Roch model is not adequate to
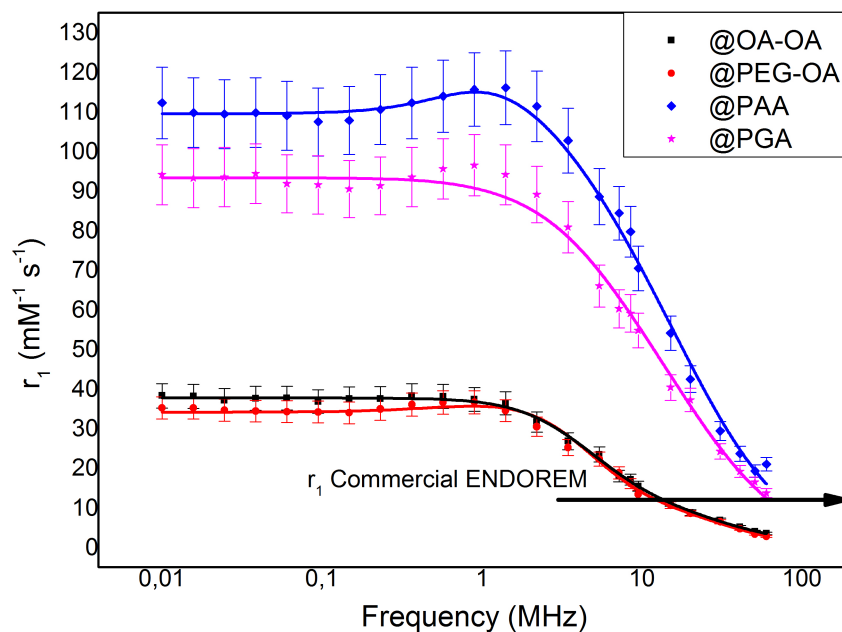
Figure 4.19: r_1 relaxation rate fitted with Roch model. The black arrow represents the relaxivity of the commercial compared ENDOREM.
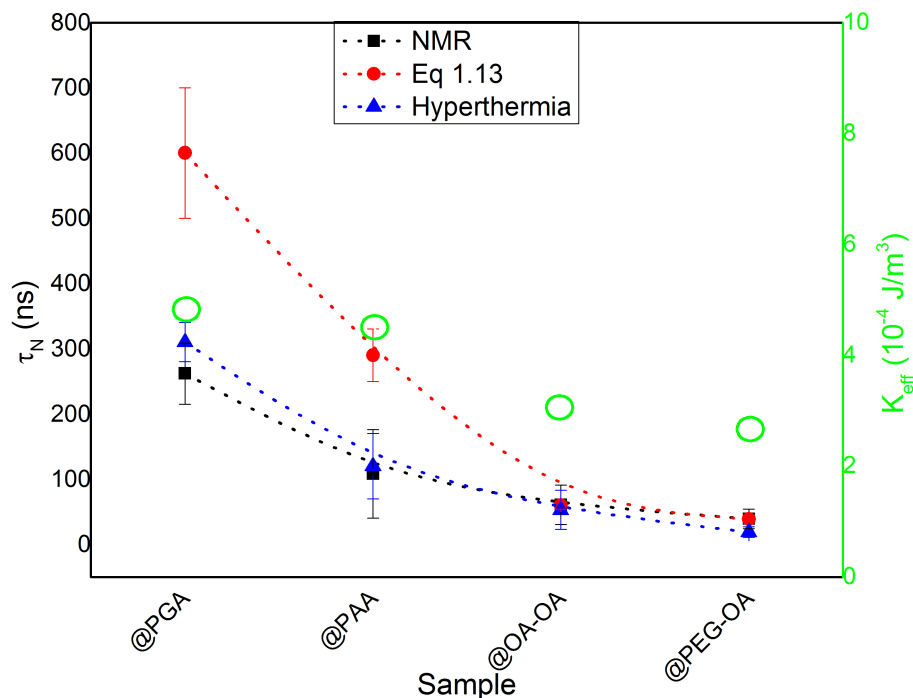

Figure 4.20: Néel relaxation times evaluated from NMR fit, hyperthermic fit with LRT model and eq. (1.13). In the graph the values of K_{eff} evaluated with eq. 3.5 are also reported (green empty circles).

explain completely the r_2 profile (Fig. (4.21)). As explained in the previous chapter, a possibly unknown microscopic mechanism that has an important role in high frequency transverse relaxation process, by introducing a further dephasing term, is present.

Using the model introduced in chapter 2 for r_2, it's possible to state that @PGA and @PAA samples are in the range of MAR model. On the contrary, the @OA-OA and @PEG-OA display a transverse relaxivity lower than the previous samples, probably because their spin dynamics is at the limit of the MAR model validity.
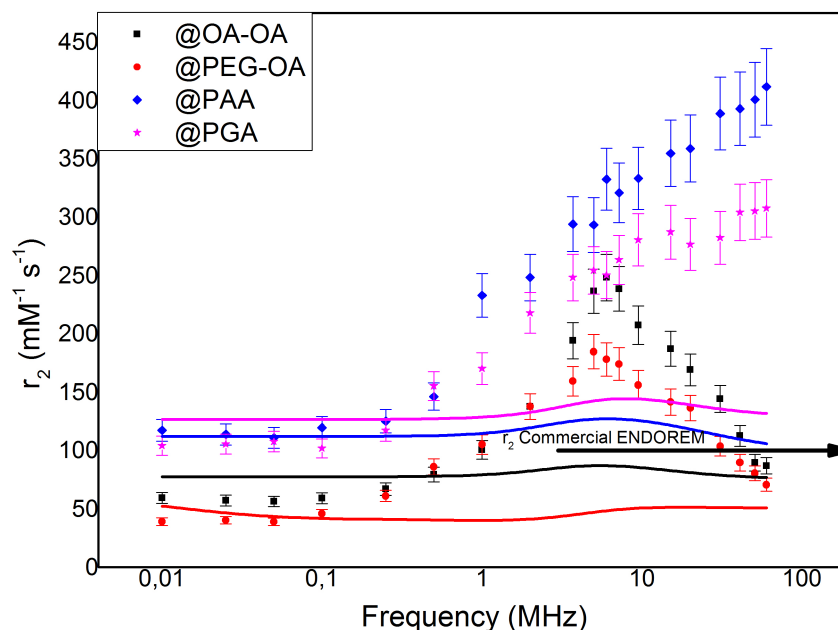

Figure 4.21: r_2 relaxation rate fitted with Roch model. The black arrow represents the relaxivity associated to commercial compared ENDOREM.

4.6 Conclusions

The organic coating is an essential condition to use the magnetic nanoparticles in medical area. Superparamagnetic NPs are perfect candidates due to large magnetization also at low magnetic field, and proper spin dynamics.

DC magnetic measurements as a function of temperature in ZFC and FC conditions confirm the presence of two spin populations in the samples. We ascribed the two blocking temperature distributions to the core and surface spins population: this division plays a fundamental role, because the different population behaviour is responsible of different magnetic properties. The hysteresis loops result completely closed at 2.5 and 260 K, but with two different value of saturation magnetization: over 70 emu/g for naked, @PAA and @PGA samples and about 60 emu/g for particles with oleic acid. From hysteresis, the
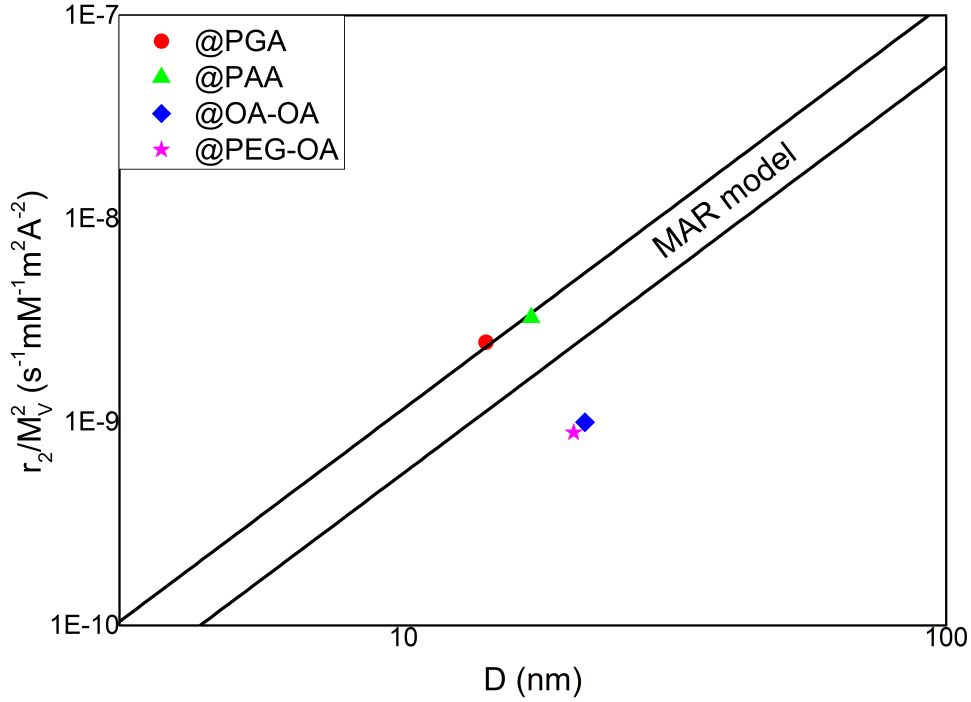
Figure 4.22: Dependence of r_D/M_V^2 from diameter: the area between the two solid lines is the validity zone of MAR model. The coloured points are obtained considering the transverse relaxivity at 60 MHz and the minimum approach distance obtained from NMR data fit.

high field magnetization behaviour confirms the presence of canted spins on the surface of nanoparticles, also found in the activation volume fit, where the effective volume of spin that contribute to the reversal is smaller than the TEM core volume.

As confirmed by the Henkel curves, the dominant interaction is the dipolar interaction, diminished for the coated ones compared to bare MNPs.

The hyperthermic measurements were performed at different frequencies and fields and show differences ascribed to magnetic properties. All the samples have a field limit for LRT model of about 16 kA/m, and thus it was possible to apply the model to evaluate the Néel relaxation time. The highlighted influence of coating on the hyperthermic heating is very important because is not possible to forecast the efficiency simply from the naked nanoparticles.

The data obtained from D-NMR analysis were fitted with the heuristic RMG model, that predicts the longitudinal and transversal relaxation behaviour. Regarding the longitudinal relaxation, the profiles have a typical superparamagnetic shape: at low frequencies they display a plateau and the Néel relaxation process is dominant; at intermediate frequencies, @PGA and @PAA have a bump that identify the situation where there is maximum in the relaxation rate, proportional to the square of magnetic saturation and τ_D; at high frequencies, the relaxation decreases according to the Curie relaxation.

The parameters obtained from the fit of the longitudinal relaxivity provide an information about the permeability of the coating and the Néel relaxation time. The organic coatings create a shell that encapsulates the NPs and increases the total diameter of compound: the samples @OA-OA appear less permeable to water comparable to @PGA and @PAA. The Néel time τ_N is for all samples of the order of magnitude of superparamagnetic iron-based nanoparticles (1-1000 ns), compatible with times obtained from hyperthermia and from base formulas.

The r_2 measurements were interpolated with the parameters obtained from the fit of longitudinal relaxivities: the agreement is good only at low frequency (below 0.1 MHz) while there is a great discrepancy in the high frequencies region, where the calculated r_2 is always lower than the experimental one. The results for @PAA and @PGA are in accordance with the MAR model, but this does not happen for the other two samples.

Chapter 5

Conclusions

In this thesis the physical properties of coated iron-oxide NPs and their possible use in medical area, in particular as hyperthermia mediators and/or contrast agents for MRI were presented. In particular, the attention was focused on two characteristics that can affect their hyperthermic and relaxometric efficiency: the core dimension and the coating.

The static magnetic properties of the samples were deeply investigated by means of DC magnetic measurements, which include the magnetization as a function of temperature (ZFC/FC in the range 2-300 K) and the magnetization as a function of the external static magnetic field (hysteresis) at two different temperatures (2.5 K and 300 K).

As concerns the study of NPs with different sizes, the morphological (XRD, TEM, AFM) characterization displayed a spherical shape with diameter equal to 10 (A), 14 (B) and 19 (C) nm.

The samples present a completely closed hysteresis loop at room temperature while at 2.5 K the loop opens progressively when the core dimension increases. A variation of the saturation magnetization (M_s) value was also observed: for sample A it is 62 emu/g, 65 emu/g for B and 69 emu/g for sample C.

The data have been analysed in order to implement a heuristic model that connect the Specific Loss Power to the applied magnetic field for NPs with different diameters. The results have been compared with the models available in literature: the Linear Response Theory (for superparamagnetic NPs), the Stoner-Wohlfarth (for ferromagnetic NPs) and the Rayleigh (for multi-domain NPs) models.

The theoretical limit for the application of the LRT model is verified only for sample A (confirmed also by τ_N value) while, for the other ones, the LRT is not appropriate to interpret the experimental data, which were fitted with a phenomenological free exponential model $SLP \propto H^x$.

The x values for B and C resulted between 2 and 3, as expected in the limits of the LRT and Rayleigh model, respectively. The exponents increase with magnetic field, in particular for sample C that is in the transition zone

between superparamagnetic and ferromagnetic phase.

The samples were diluted much more in order to perform nuclear relaxivity measurements, to explore the microscopic relaxation mechanisms of water protons. The nuclear relaxation times, both longitudinal (T_1) and transverse (T_2), have been measured over a wide range of frequencies (10 kHz - 60 MHz). The relaxation rates resulted higher than commercial Endorem and the r_1 curves were fitted with the Roch-Muller-Gillis (RMG) model (which works well for ferrite NPs with core diameter d < 20 nm and is commonly used in literature) displaying a behaviour typical of superparamagnetic compounds.

The second aim of this thesis was the study of the coating effect on the SLP. The samples were prepared and tested at The Vinca Institute of Nuclear Sciences in Belgrade. Four different coated samples have been compared with naked one: the core dimension was the same ($\sim 8nm$ of diameter). The derivative of the curve obtained from the subtraction of the ZFC and FC (vs temperature at $\mu_0 H = 5mT$) data, presents a dominant peak at 63 K (naked) and 94 K (coated) but also a second peak at lower temperature, correlated to the surface spin population.

From hyperthermia measurements, the samples present different SLP values. The samples coated with PEG-OA and OA-OA have both a low value of SLP compared to the other samples because the different coatings block the surface spins in different percentage. So the NPs with lower activation volume (@PGA) have fewer spins that participate to the magnetic reversal motion compared to the naked ones. Consequently, the reduced activation volume affects the magnetic saturation and also the SLP.

As concerns the NMR measurements, all the longitudinal relaxometry data were successfully fitted with the 'heuristic' RMG model. On the contrary, the RMG model cannot reproduce the experimental data of the transverse relaxivity. Although the agreement between the model and the experimental r_2 data results quite good in the low frequency region (where $r_1 = r_2$), there is a net discrepancy in the high field region, where the calculated r_2 values are always lower than the experimental ones. This could be possibly due to the fact that the theory does not take into account one (or more) microscopic relaxation mechanism which speeds up the transverse relaxation process.

In conclusion all the particles presented in this thesis have a great possibility of application in medical area. The free exponential model allows to forecast SLP and relaxivity values (hyperthermic efficiency) as a function of the NPs dimensions at difference frequency and field. Moreover, the biocompatible coatings don't reduce significantly the magnetic properties and preserve the hyperthermic and relaxometric features, observed in ferrofluid, also *in vitro* and *in vivo*.

Appendix

Experimental Measurements in Progress

The study of iron-oxide-based NPs for hyperthermia was the topic of this thesis, in particular regarding size and coating effects on heat release efficiency.

An important characteristics that affects the SLP is the presence of magnetic ions that modify the anisotropy of NPs: about this, samples of $Co_xFe_{3-x}O_4$ with different cobalt concentrations were synthesized. Spinel iron oxides were prepared by reverse coprecipitation with various cobalt content (starting from x=0 to 1, i.e. from pure maghemite ending with cobalt ferrite) to evaluate the effect of different degree of cobalt substitution. Since the biocompatibility of cobalt ferrites is questionable because of the cobalt content, three selected nanoparticles (with 0, 25 and 100 % Co content) were coated with a new type of amphiphilic folate-PEG copolymer. The final aim was to show the influence of this copolymer coating on the physical and biological properties of cobalt containing spinel ferrites.

The heat release efficiency results show an interesting trend: the NPs with higher SLP have a concentration of cobalt equal to 50 %. This is possibly linked to the K_{eff}, that reaches the maximum value at intermediate composition. The main contribution to K_{eff} derives from surface anisotropy, which, unlike the magneto-crystalline term, is much less dependent on the cobalt content, due to the weaker crystal field experienced by surface ions. The contributions of surface and magneto-crystalline anisotropy become comparable when the cobalt concentration increases.

Other systems investigated were the nanoclusters of NPs: if the NPs are assembled in cluster the behaviour is different compared to single NPs with the same dimensions. The nanoclusters considered show a peak in SLP for diameter of 75 nm: the hysteresis losses of ferromagnetic nanoclusters can be affected by the anisotropy of the system (surface anisotropy or/and surface spin disorder), the alignment and the size/magnetization of the incorporated particles into the nanoclusters, as well as of the emerged dipolar interactions among them. All the above parameters that affect the hysteresis losses may explain the SLP decrease as the volume fraction increases.

AFM apparatus

The Atomic Force Microscope apparatus (used in collaboration with Dot. Orsini at University of Milan) allows to establish the average coating thickness. The method employed for NPs is the *tapping* modality: it operates in a middle range where the repulsive and attractive forces between sample and probe dominate. The cantilever is positioned at 30 nm from the sample and it is oscillating at resonance frequency so that the tip position and movement are affected by the samples' morphology. The variation of the amplitude of oscillation is converted in a signal which is acquired through the scanner system. It modifies the height of the sample in order to restore the initial oscillation: this information is used to reconstruct the NPs images.

The AFM was used in the *tapping* mode in air. It was analysed a minimum of 25 nanoparticles for each sample and by fitting the histogram plots with LogNormal distribution, the hydrodynamic radius was obtained.
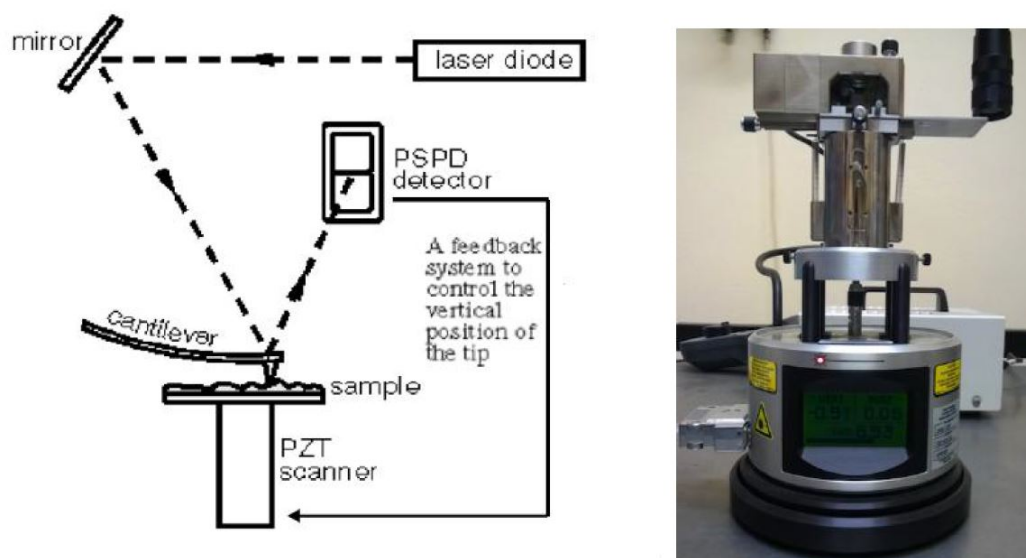

Figure 5.1: Main components of AMF microscope(left) and the instrument used (right).

SQUID Apparatus

The magnetic measurements were performed with a Quantum Design MPMS-XL SQUID magnetometer. The samples were assembled on a rod and inserted in a cavity where a superconducting magnet generates a static field; afterwards, the chamber with the sample was sealed and maintained at low pressure with static helium gas. The measurements were performed by moving the sample with a motor that moves the rod through the superconducting system. The temperature was controlled by heaters and low temperature pumps.

In the standard measurement, the sample moves along the z axis (perpendicular to the ground and parallel to the magnetic field), in order to measures the longitudinal magnetization. The change of magnetic flux produces a current variation in the coils: the SQUID, with a loop inductance L, put in a shielded area, detects it via a mutual coupling of constant $M = \kappa_S \sqrt{L_S L}$ with a secondary inductor L_S. The flux sensed by the SQUID is:

$$\Delta\phi_e = \frac{M}{L_P + L_S} N_P \Delta\Phi \tag{5.1}$$

where L_P is the inductance of the primary coil, N_P the number of primary coil and $\Delta\Phi$ the change of magnetic flux. The SQUID is coupled inductively to a resistive circuit: it allows to acquire the output voltage of the measurements. The resistive circuit is driven by a current oscillating at or near his reasoning frequency ω_0 and has a quality factor $Q = \omega_0 L_T / R_T$ (L_T and R_T are the inductance and the resistance of the third circuit, respectively): the corresponding current that circulates in the induction coupled is $I_T \sin(\omega_{rf} t) = Q I_{rf} \sin(\omega_{rf} t)$ and the equivalent output voltage is $V_T \sin(\omega_{rf} t)$ (Fig. (5.2)).
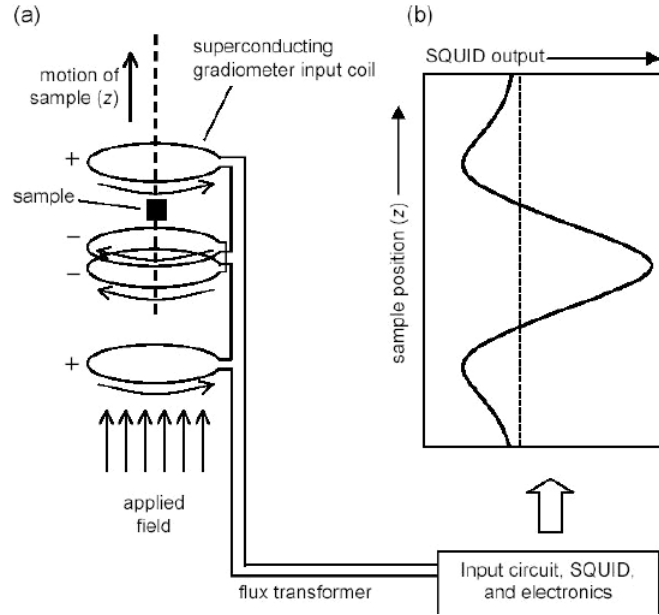

Figure 5.2: SQUID detection system (a) and typical voltage vs position curve (b).

MFH Apparatus

For the hyperthermic measurements the *Magnetherm* system from *NanoTherics* was used: it is composed by two different coils of copper with 9 and 17 turns (50 mm of diameter) and by a set of five different capacitors.

The different combinations between coil and capacitors are obtained varying the value of the DC current while the magnetic field is measured with an Hall probe.

Figure 5.3: Magnetherm apparatus.

The temperature of the samples was extracted with an *Optocon* optical fiber. The fiber is composed by gallium arsenide (GaAs) crystal, a semiconductor characterized by a band gap that changes when the temperature varies. The *Optocon* system allows to measure temperature from -200 °C to 300 °C with 0.1 °C of resolution. The non conductivity of the fiber is useful to measure the temperature in magnetic field.

The samples were studied in a vial containing 1 ml of ferrofluid, surrounded by polystyrene to have major thermal isolation. The sample was left 3 minutes in the system, before turning on the field, in order to have the thermal equilibrium.

NMR Apparatus

The NMR measures were performed with a *Stelar* spectrometer. The spectrometer works at low and high frequency intensity (10 kHz - 60 MHz) and in a pulsed regime.

In the high field (H > 0.1 T) configuration, the NMR signal is easily detected, but when the proton Larmor frequency decrease below 4 MHz the signal to noise ratio has to be increased by means of a fast field cycling (FFC) technique.

The spectrometer presents a classical electromagnet (different for $\nu<10$ MHz and $\nu>10$ MHz) and the RF pulse generator that allows to produce the correct sequences used to measure the longitudinal and transversal relaxation times. In figure 5.4 the blocks diagram of the employed spectrometer and the whole apparatus are shown. The blocks are named by alphabetic letters (A to I) and their function can be described as follow:

- (A): the *synthesizer* generates the resonant radio frequency ω_{RF} with high stability and a precision of few Hz. The *gate* is able to shift the phase of the generated RF pulse in the xy plane (x, -x, y, -y) which results transversal with respect to the external applied field (z).

- (B): the *gate* allows to modulate the pulse by the chosen RF frequency.

- (C): the *pulse programmer* generates and selects the time length and/or the shape of the RF pulse.

- (D): the *pre-amplifier* gives the required amplitude to the transmitted RF pulse.

- (E): the *duplexer* allows a bi-directional communication between the coil containing the sample (F) and the spectrometer. In particular it separates the transmitted exciting pulse from the received signal due to the proton relaxation.

- (F): the two *mixers* multiply the nuclear magnetic relaxation signal coming from the sample by two pure oscillating signals dephased one with respect to each other by $\pi/2$.

- (H): an *analogical to digital converter* (ADC) acquires the signal and send it to a personal computer PC (I) which elaborates the signal and controls the spectrometer's parameters.

The electromagnets imposing the probing frequency, not included in the blocks diagram, offer a spatial homogeneity of 10 ppm (high frequency electromagnet) and of 40-60 ppm (low frequency electromagnet). In resonance condition ($\omega_{RF} = \omega_{Larmor}$) the measured signal is called free induction decay (FID) whose amplitude at t = 0 is proportional to the net nuclear magnetization (M) generated by the electromagnet in the direction of its static magnetic field. The time dependence of the FID contains informations about the longitudinal and transversal nuclear relaxation times. These times (T_1 and T_2) allow to access indirectly the typical correlation times of the investigated system.

Sequences

The longitudinal times T_1 were recorded by means of a saturation recovery (SR) sequence with the possibility to pre-polarize the sample (for frequencies < 4 MHz).

T_2 have been measured by means of a Carr-Purcell-Meiboom-Gill (CPMG, Fig. 5.6) and of a pre-polarized spin echo (PP-SE, Fig. 5.7) for high (i.e. f > 4 MHz) and low (i.e. f < 4 MHz) frequencies respectively.
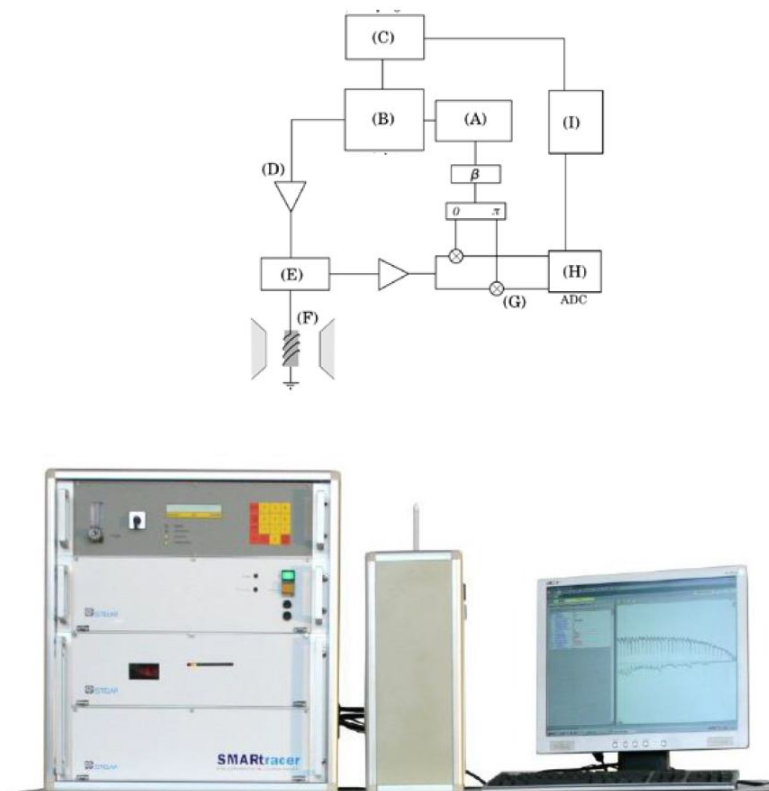
Figure 5.4: Blocks diagram (top) and photograph (bottom) of the employed NMR spectrometer.
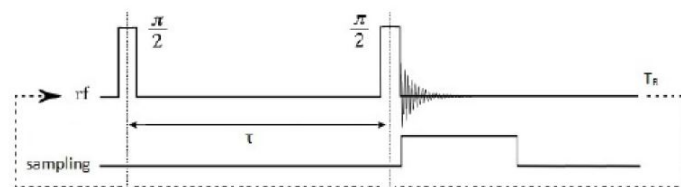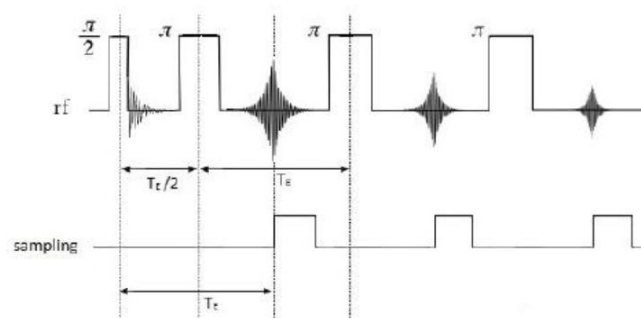

Figure 5.5: Saturation recovery sequence.
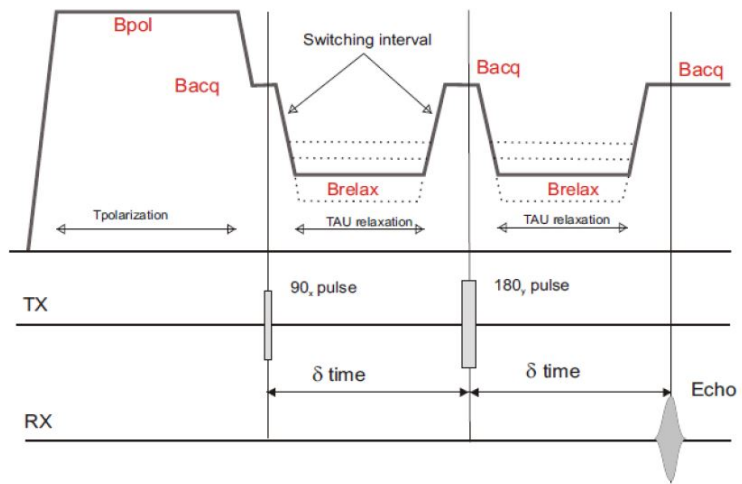

Figure 5.6: CPMG sequence.

90

Figure 5.7: Pre-polarized spin echo sequence.

Publications

M. Cobianchi, A. Guerrini, M. Avolio, C. Innocenti, M. Corti, P. Arosio, F. Orsini, C. Sangregorio, and A. Lascialfari
Experimental determination of the frequency and field dependence of Specific Loss Power in Magnetic Fluid Hyperthermia
Journal of Magnetism and Magnetic Materials 444 (2017) 154-160.

A. Boni, M. Basini, L. Capolupo, C. Innocenti, M. Corti, M. Cobianchi, F. Orsini, C. Sangregorio and A. Lascialfari
Optimized PAMAM coated Magnetic Nanoparticles for simultaneous Hyperthermic treatment and contrast enhanced MRI diagnosis.
RSC Adv., 2017, 7, 44104.

M. Basini, A. Guerrini, M. Cobianchi, F. Orsini, , M. Avolio, C. Innocenti, C. Sangregorio, A. Lascialfari and P. Arosio.
Tailoring the Magnetic core of organically-coated iron oxides nanoparticles to influence their relaxometric properties
(to be submitted).

M. Basini, T. Orlando, M. Mariani, M. Cobianchi, T. Kalaivani, P. Arosio, F. Orsini, S. Sanna, D. Peddis, V. Bonanni and A. Lascialfari
Local Spin Dynamics in $\gamma - Fe_2O_3$ hollow Nanoparticles unravelled by Muon Spin Relaxation
(in preparation).

G. Muscas, M. Cobianchi, A. Lascialfari, C. Cannas, A. Musinu, A. Ardu and D. Peddis
Thermal phase duration influences on size polydispersion of nanoparticles
(to be submitted).

M. Cobianchi, A. Lascialfari, V. Kusigerski, A. Mrakovic, N. Knezevic, D. Peddis and E. Illes
Effects of organic coating on hyperthermia efficiencies

(in preparation).

ELSEVIER

Research articles

Experimental determination of the frequency and field dependence of Specific Loss Power in Magnetic Fluid Hyperthermia

CrossMark

M. Cobianchi [a,*], A. Guerrini [b], M. Avolio [a], C. Innocenti [b], M. Corti [a], P. Arosio [d], F. Orsini [d], C. Sangregorio [c], A. Lascialfari [d,a]

[a] Dipartimento di Fisica and INSTM, Università degli Studi di Pavia, Via Bassi 6, 27100 Pavia, Italy
[b] Dipartimento di Chimica, Università degli studi di Firenze, Via della Lastruccia 3, Sesto F.no (FI), Italy
[c] CNR-ICCOM, Via della Lastruccia 3, Sesto F.no (FI), Italy
[d] Dipartimento di Fisica and INSTM, Università degli Studi di Milano, Via Celoria 16, 20133 Milano, Italy

ABSTRACT

Magnetic nanoparticles are promising systems for biomedical applications and in particular for Magnetic Fluid Hyperthermia, a therapy that utilizes the heat released by such systems to damage tumor cells. We present an experimental study of the physical properties that influences the capability of heat release, i.e. the Specific Loss Power, *SLP*, of three biocompatible ferrofluid samples having a magnetic core of maghemite with different diameter d = 10.2, 14.6 and 19.7 nm. The *SLP* was measured as a function of frequency f and intensity H of the applied alternating magnetic field, and it turned out to depend on the core diameter, as expected. The results allowed us to highlight experimentally that the physical mechanism responsible for the heating is size-dependent and to establish, at applied constant frequency, the phenomenological functional relationship $SLP = c \cdot H^x$, with $2 \leq x < 3$ for all samples. The x-value depends on sample size and field frequency, here chosen in the typical range of operating magnetic hyperthermia devices. For the smallest sample, the effective relaxation time $\tau_{eff} \approx 19.5$ ns obtained from *SLP* data is in agreement with the value estimated from magnetization data, thus confirming the validity of the Linear Response Theory model for this system at properly chosen field intensity and frequency.

© 2017 Elsevier B.V. All rights reserved.

1. Introduction

Magnetic nanoparticles are promising tools in biomedical applications against cancer, and suitable systems for diagnostics by e.g. Magnetic Resonance Imaging and innovative therapies, like drug delivery and Magnetic Fluid Hyperthermia (MFH) [1–11]. The MFH is a recently developed anti-cancer locally acting technique which aims to reduce the side effects of the traditional techniques as chemo- or radio-therapies [12]. This technique makes use of the capability of magnetic nanoparticles (MNPs) to release heat when exposed to an alternating magnetic field (AMF), as a therapeutic treatment to selectively destroy tumor cells within the human body. In MFH treatments, the AMF application is strictly limited to a safety range of frequency f and intensity H due to medical and technical restrictions, as established by the Brezovich criterion which requires $H \cdot f < 4.85 \cdot 10^8$ Am^{-1} s^{-1} [13]. The amount of magnetic field energy converted into heat (and subsequently absorbed by tissues) is given by the energy losses occurring during the MNP

magnetization reversal, according to the dynamic regime determined by the MNPs physico-chemical properties (size, shape, kind of magnetic core, etc.) as well as by the external field and temperature [14–18]. Magnetization reversal can be produced by a rigid rotation of the particles (Brown process) or by a coherent reorientation of the electronic spins inside the particles (Néel process) [19–22]. The characteristic times τ_B and τ_N for Brown and Néel processes, respectively are $\tau_B = 3\eta V_H/k_B T$, where η is the viscosity of the environmental fluid, V_H the hydrodynamic volume of the particle, k_B the Boltzmann constant and T the temperature of the system, and $\tau_N = \tau_0 exp(KV/K_B T)$, where K is the uniaxial magnetic anisotropy constant of the crystalline core, V the volume of the magnetic core and τ_0 the attempt time typically assumed to be 10^{-9} s [3,23,24]. It is noticed that, when a large ac and/or DC magnetic field is applied and the condition $\zeta = (mB/k_B T) \ll 1$ is no more verified, the expressions of τ_B and τ_N assume different analytical forms [25,26].

The parameter that describes the MNPs capacity to release heat to the surrounding environment when exposed to an AMF is the Specific Loss Power (*SLP*). In Fig. 1 the most common empirical models used to evaluate the *SLP* are reported in their intervals of

* Corresponding author.
  E-mail address: marco.cobianchi01@universitadipavia.it (M. Cobianchi).

RSC Advances

PAPER

Check for updates

Optimized PAMAM coated magnetic nanoparticles for simultaneous hyperthermic treatment and contrast enhanced MRI diagnosis†

A. Boni, [ID] *a A. M. Basini,b L. Capolupo,a C. Innocenti,c M. Corti,b M. Cobianchi,d F. Orsini,b A. Guerrini,c C. Sangregorioce and A. Lascialfarib

We report the synthesis and characterization of multi-functional monodisperse superparamagnetic Magnetic NanoParticles, MNPs, able to act as contrast agents for magnetic resonance and Magnetic Fluid Hyperthermia (MFH) mediators. The investigated samples are constituted of a magnetic core of magnetite and a biocompatible PAMAM coating. We studied two samples with the same magnetic volume but different shape, i.e. spherical and faceted. Despite the relatively large size (MNPs of 20 nm diameter) that generally leads to particles' aggregation and instability, the resulting samples were very stable. For faceted MNPs, the efficiency in contrasting Magnetic Resonance images, i.e. the nuclear transverse ^{1}H NMR relaxivity r_2, reached values of about 250/300 mM^{-1} s^{-1} at clinical frequencies $f > 5$ MHz, i.e. 2.5/3 times higher than the commercial compound Endorem, while the Specific Absorption Rate at $H_{ac} \sim 10$ kA m^{-1} and frequency $f < 300$ kHz (i.e. within the physiological limits) reaches 900 W g^{-1}, suggesting this system as a potentially useful mediator for MFH. The experimental data strongly indicate the new synthesized MNP systems as good candidates for theranostic applications.

1. Introduction

Local control of tumors is a major challenge because of the cells' rapid proliferation and the possible diffusion of tumor cells in the whole body with consequent metastases. In the current local treatments of tumors by means of radiotherapy (RT) and chemotherapy (ChT), and related refined techniques (like cyber-knife and gamma-knife), the side-effects are severe. For many tumor sites,[1-3] the effectiveness of RT and ChT is significantly enhanced when combined with hyperthermia (HT), i.e. raising tissue temperature up to 43–45 °C. Indeed, HT has been shown to improve the clinical outcome when added to RT and ChT[4-6] or alone.[7] In addition to a reduction in tumor bulk and analgesia requirements, the thermal treatment as coadjuvant treatment improves quality of life with decreased pain and preserves patient's function and appearance. Further advantages include a reduction in procedural costs, avoidance of complex repetitive surgeries, and the ability to visualize the area during the treatment.

Among various methods of hyperthermia, Magnetic Fluid Hyperthermia (MFH) has drawn considerable attention.[8-10] In MFH, fluids containing magnetic nanoparticles (MNPs) (generally iron oxide based systems) are delivered to the cancer and then heated by on external alternating magnetic field, resulting in hyperthermic treatment of cancer tissue. Magnetic nanoparticles based therapy has been investigated for many types of tumors, including those of the central nervous system.[11,12] Clinical trials (Phase I and II) on glioblastoma multiforme and prostate cancers have already been performed[13] and, at present, Phase III clinical study on the first is going on. Concerning glioblastoma, the survival time of patients has been increased by a factor 1.5/2 after MFH application. This result stimulated a lot of multidisciplinary research all over the world involving physicists, chemists, engineers, biologists and physicians, often starting from basic proprieties of novel nanoparticles to experimental tests on cells cultures and animal models.

MNPs have also been proposed as complimentary or alternative Magnetic Resonance Imaging (MRI) contrast agents with respect to the paramagnetic Gadolinium-Based Contrast Agents (GBCAs), thanks to their ability to increase the transverse relaxation rate (r_2) and bring negative contrast.[14] The general idea about MNPs is to obtain a nanosystem that can work as therapeutic MFH agent due to its heat release capacity, and as diagnostic agent because of the contrast efficiency in the MR

aCenter for Nanotechnology Innovation @NEST, Istituto Italiano di Tecnologia, Piazza San Silvestro, 12 – 56127 Pisa, Italy. E-mail: adriano.boni1@virgilio.it

bDipartimento di Fisica and INSTM, Università degli studi di Milano, Italy

cDepartment of Chemistry "Ugo Shiff", University of Florence and INSTM, via della Lastruccia 3 – 50019 Sesto F. no, Firenze, Italy

dDipartimento di Fisica and INSTM, Università degli studi di Pavia, Italy

eCNR-ICCOM and INSTM, via Madonna del Piano, 50019 Sesto F. no, Firenze, Italy
† Electronic supplementary information (ESI) available. See DOI: 10.1039/c7ra07589h

Ringraziamenti

Ringraziamenti

Ringraziamenti sentiti:

Al Prof. Lascialfari e al Prof. Corti per l'opportunitá che mi hanno offerto nello svolgere questo dottorato, seguendomi lungo questi tre anni.

Al Prof. Santini e alla Prof.ssa Casula per il lavoro di review.

A Paolo, Francesco e Martina, i quali mi hanno aiutato innumerevoli volte in laboratorio con infinita pazienza, insegnandomi e correggendo i (moltissimi) errori compiuti.

Ai due Matteo: per la compagnia in ufficio, la collaborazione in laboratorio e per il bel clima di amicizia creatosi in questi anni , ma, soprattutto, grazie perché se non ci foste stati voi avrei potuto finire in studio con uno juventino.

A mamma e papà, per l' incessante sostegno.

Ad Alessia, con la quale ho condiviso questi anni.

A Vecchie, Gero e Guarna.

A tutte le persone che in qualsiasi modo hanno reso piacevoli questi anni.

Bibliography

[1] T. K. Jain, M. A. Morales, S. K. Sahoo, D. L. Leslie-Pelecky, and V. Labhasetwar. Iron oxide nanoparticles for sustained delivery of anticancer agents. *Molecular pharmaceutics*, 2(3):194–205, 2005.

[2] I. Chourpa, L. Douziech-Eyrolles, L. Ngaboni-Okassa, J. F. Fouquenet, S. Cohen-Jonathan, M. Soucé, H. Marchais, and P. Dubois. Molecular composition of iron oxide nanoparticles, precursors for magnetic drug targeting, as characterized by confocal raman microspectroscopy. *Analyst*, 130(10):1395–1403, 2005.

[3] N. Sanvicens and M. P. Marco. Multifunctional nanoparticles-properties and prospects for their use in human medicine. *Trends in biotechnology*, 26(8):425–433, 2008.

[4] H. Gu, K. Xu, Z.u Yang, C. K. Chang, and B. Xu. Synthesis and cellular uptake of porphyrin decorated iron oxide nanoparticles—a potential candidate for bimodal anticancer therapy. *Chemical communications*, (34):4270–4272, 2005.

[5] J. W. M. Bulte. Intracellular endosomal magnetic labeling of cells. *Magnetic Resonance Imaging: Methods and Biologic Applications*, pages 419–439, 2006.

[6] M. F. Casula, P. Floris, C. Innocenti, A. Lascialfari, M. Marinone, M. Corti, R. A. Sperling, W. J. Parak, and C. Sangregorio. Magnetic resonance imaging contrast agents based on iron oxide superparamagnetic ferrofluids. *Chemistry of Materials*, 22(5):1739–1748, 2010.

[7] Q. A. Pankhurst, J. Connolly, S. K. Jones, and J. J. Dobson. Applications of magnetic nanoparticles in biomedicine. *Journal of physics D: Applied physics*, 36(13):R167, 2003.

[8] P. Reimer and R. Weissleder. Development and experimental use of receptor-specific mr contrast media. *Der Radiologe*, 36(2):153–163, 1996.

[9] D. Proske, M. Blank, R. Buhmann, and A. Resch. Aptamers—basic research, drug development, and clinical applications. *Applied microbiology and biotechnology*, 69(4):367–374, 2005.

[10] M. Colombo, S. Carregal-Romero, M. F. Casula, L. Gutiérrez, M. P. Morales, I. B. Böhm, J. T. Heverhagen, D. Prosperi, and W. J. Parak. Biological applications of magnetic nanoparticles. *Chemical Society Reviews*, 41(11):4306–4334, 2012.

[11] N. Singh, G. J. S. Jenkins, R. Asadi, and S. H. Doak. Potential toxicity of superparamagnetic iron oxide nanoparticles (spion). *Nano reviews*, 1(1):5358, 2010.

[12] P. Cherukuri, E. S. Glazer, and S. A. Curley. Targeted hyperthermia using metal nanoparticles. *Advanced drug delivery reviews*, 62(3):339–345, 2010.

[13] J. L. Phillips. A topical review of magnetic fluid hyperthermia. *Journal of Science and Health at the University of Alabama*, 3:14–18, 2005.

[14] D. H. Kim, K. N. Kim, K. M. Kim, I. B. Shim, and Y. K. Lee. Necrosis of carcinoma cells using co (1-x) ni (x) fe (2) o (4) and ba (1-x) sr (x) fe/12/o/19/ ferrites under alternating magnetic field. *IEEE transactions on magnetics*, 40(4):2985–2987, 2004.

[15] B. Hildebrandt, P. Wust, O. Ahlers, A. Dieing, G. Sreenivasa, T. Kerner, R. Felix, and H. Riess. The cellular and molecular basis of hyperthermia. *Critical reviews in oncology/hematology*, 43(1):33–56, 2002.

[16] K. M. Krishnan. Biomedical nanomagnetics: a spin through possibilities in imaging, diagnostics, and therapy. *IEEE transactions on magnetics*, 46(7):2523–2558, 2010.

[17] R. Yanes, O. Chubykalo-Fesenko, H. Kachkachi, D.A. Garanin, R. Evans, and R.W. Chantrell. Effective anisotropies and energy barriers of magnetic nanoparticles with néel surface anisotropy. *Physical Review B*, 76(6):064416, 2007.

[18] J. M. D. Coey. *Magnetism and magnetic materials*. Cambridge University Press, 2010.

[19] X. Batlle and A. Labarta. Finite-size effects in fine particles: magnetic and transport properties. *Journal of Physics D: Applied Physics*, 35(6):R15–R42, 2002.

[20] F. Burrows. *A Model og Magnetic Hyperthermia*. The University of York, Department of Physics, 2012.

[21] D. Peddis, C. Cannas, A. Musinu, and G. Piccaluga. Coexistence of superparmagnetism and spin-glass like magnetic ordering phenomena in a cofe2o4-sio2 nanocomposite. *The Journal of Physical Chemistry C*, 112(13):5141–5147, 2008.

[22] D. Peddis and other. Spin-canting and magnetic anisotropy in ultra-small cofe2o4 nanoparticles. *The Journal of Physical Chemistry B*, 112(29):8507–8513, 2008.

[23] D. Peddis and other. Spin-glass-like freezing and enhanced magnetization in ultra-small cofe2o4 nanoparticles. *Nanotechnology*, 21(12):125705, 2010.

[24] V. K. Varadan, L. Chen, and L. Xie. *Nanomedicine. Design and Applications of Magnetic Nanomaterials, Nanosensors and Nanosystems*. Wiley.

[25] A. Thiaville. Extensions of the geometric solution of the two dimensional coherent magnetization rotation model. *Journal of Magnetism and Magnetic Materials*, 182(5):5–18, 1998.

[26] A. Thiaville. Coherent rotation of magnetization in three dimensions: A geometrical approach. *Physical Review B*, 61(18):12221, 2000.

[27] S. Laurent, D. Forge, M. Port, A. Roch, C. Robic, L. Vander Elst, and R. N. Muller. Magnetic iron oxide nanoparticles: synthesis, stabilization, vectorization, physicochemical characterizations, and biological applications. *Chemical Reviews*, 108(6):2064–2110, 2008.

[28] K. O'Grady. *Ph.D Thesis*, 1982.

[29] R. E. Rosenweig. Heating magnetic fluid with alternating magnetic field. *Journal of Magnetism and Magnetic Materials*, 252:370–374, 2002.

[30] F. Tournus and E. Bonet. Theoretical model and analytical expressions for a single magnetic anisotropy energy. *Journal of Magnetism and Magnetic Materials*, 323(9):1109–1117, 2011.

[31] S. J. Lee and S. Lee. The spin structure of maghemite investigated by 57fe nmr. *New Journal of Physics*, 8(6):98, 2006.

[32] M. Basini. *Effect of the hollow topology on the spin dynamics in magnetic iron oxide nanoparticles*. Ph. D. Thesis, 2017.

[33] J. Cheon and J. H. Lee. Synergistically integrated nanoparticles as multimodal probes for nanobiotechnology. *Accounts of Chemical Research*, 41(12):1630, 2008.

[34] Q Wang and Liu. J. *Fundamental Biomedical Technologies*. Springer Netherlands, 2011.

[35] L. Lartigue, C. Innocenti, T. Kalaivani, A. Awward, M. D. M. Sanchez Dunque, Y. Guari, J. Larionova, C. Guerin, J. L. Montero, V. Barragan-Montero, P. Arosio, A. Lacialfari, D. Gatteschi, and C. Sangregorio. Water-dispersible sugar-coated iron oxide nanoparticles. an evaluation of their relaxometric and magnetic hyperthermia properties. *Journal of the American Chemical Society*, 133(27):1120–1126, 2011.

[36] C. Cervadoro, C. Giverso, P. Rohit, S. Subhasis, L. Preziosi, J. Wosik, A. Brazdeikis, and P. Decuzzi. Design maps for the hyperthermic treatment of tumors with superparamagnetic nanoparticles. *PLoS One*, 8(2), 2013.

[37] G. E. P. Box and H. L. Lucas. Design of experiments in non-linear situations. *Biometrika*, 46(1):77–90, 1959.

[38] S. Chikazumi and D. Graham. *Physics of erromagnetism, Second editon.* Oxford University Press, 2009.

[39] R. Hergt, S. Dutz, and M. Roder. Effects of size distribution on hysteresis losses of magnetic nanoparticles for hyperthermia. *Journal of Physics: Condensed Matter*, 20(38):385214, 2008.

[40] N. A. Usov and Y. B. Grebenshchikov. Hysteresis loops of an assembly of superparamagnetic nanoparticles with uniaxial anisotropy. *Journal of Applied Physics*, 106(2):023917, 2009.

[41] J. Carrey, B. Mehdaoui, and M. Respaud. Simple models for dynamic hysteresis loop calculations of magnetic single-domain nanoparticles: Application to magnetic hyperthermia optimization. *Journal of Applied Physics*, 11(8):083921, 2009.

[42] E. Snoeck, C. Gatel, L. M. Lacroix, T. Blon, S. Lachaize, J. Carrey, M. Respaud, and B. Chaudret. Magnetic configurations of 30 nm iron nanocubes studied by electron holography. *Nano letters*, 8(12):4293–4298, 2008.

[43] B. D. Cullity and C. D. Graham. *Introduction to Magnetic Materials.* Wiley, Hokoben, 2009, 2009.

[44] S. Dutz and R. Hergt. Magnetic particle hyperthermia - a promising tumor therapy? *Nanotechnology*, 25(45):452001, 2014.

[45] R. Hergt, S. Dutz, and M. Zeisberger. Validity limits of the néel relaxation model of magnetic nanoparticles for hyperthermia. *Nanotechnology*, 21(1):015706, 2010.

[46] F. Bloch, A. C. Graves, M. Packard, and R. W. Spence. Relative moments of h1 and h3. *Physical Review*, 71(8):551, 1947.

[47] R. N. Muller. *Contrast agents in whole body magnetic resonance: operating mechanisms.* Wiley, New York, 1996.

[48] I. Solomon. Relaxation processes in a system of two spins. *Physical Review*, 99(2):55, 1955.

[49] N. Bloemberg. Proton relaxation times in paramagnetic solutions. *The Journal of Chemical Physics*, 27(2):572–573, 1957.

[50] J. H. Freed. Dynamic effects of pair correlation functions on spin relaxation by translational diffusion in liquids. ii. finite jumps and independent t1 processes. *The Journal of Chemical Physics*, 68(9):4034–4037, 1978.

[51] R. B. Lauffer. Paramagnetic metal complexes as water proton relaxation agents for nmr imaging: theory and design. *Chemical Reviews*, 87(5):901–927, 1987.

[52] P. Gillis, A. Roch, and R. A. Brooks. Corrected equations for susceptibility-induced t2-shortening. *Journal of Magnetic Resonance*, 137(2):402–407, 1999.

[53] Q. L. Vuong, J. F. Berret, J. Fresnais, Y. Gossuin, and O. Sandre. A universal scaling law to predict the efficiency of magnetic nanoparticles as mri t2-contrast agents. *Advanced Healthcare Materials*, 1(4):502–512, 2012.

[54] J. W. Chen, R. L. Belford, and R. B. Clarkson. Second-sphere and outer-sphere proton relaxation of paramagnetic complexes: from epr to nmrd. *The Journal of Physical Chemistry A*, 102(12):2117–2130, 1998.

[55] R. A. Brooks, F. Moiny, and P. Gillis. On t2-shortening by weakly magnetized particles: the chemical exchange model. *Magnetic Resonance in Medicine*, 45(6):1014–1020, 2001.

[56] P. Gillis, F. Moiny, and R. A. Brooks. On t2-shortening by weakly magnetized particles: the chemical exchange model. *Magnetic Resonance in Medicine*, 263(2):257–263, 2002.

[57] B. Mehdaoui, A. Meffre, J. Carrey, S. Lachaize, L. M. Lacroix, M. Gougeon, B. Chaudret, and M. Respaud. Optimal size of nanoparticles for magnetic hyperthermia: a combined theoretical and experimental study. *Advanced Functional Materials*, 21(23):4573–4581, 2011.

[58] F. H. Morrish. *The Physical Principles of Magnetism.* Wiley-IEEE Press, 2001.

[59] S. Laurent, S. Dutz, U. O. Hafeli, and M. Mahmoudi. Magnetic fluid hyperthermia: focus on superparamagnetic iron oxide nanoparticles. *Advances in colloid and interface science*, 166(1):8–23, 2011.

[60] J. I. Gittleman, B. Abeles, and S. Bozowsky. Superparamagnetism and relaxation effects in granular ni-sio2 and ni-al2o3 films. *Physical Review B*, 9(9):3891–3897, 1974.

[61] M. S. Hansen and F. Morup. Estimation of blocking temperatures from zfc/fc curves. *Journal of Magnetism and Magnetic Material*, 203(1):214–216, 1999.

[62] M. Sasaki, P. E. Jonsson, H. Takayama, and H. Mamiya. Aging and memory effects in superparamagnets and superspin glasses. *Physical Review B*, 71(10):104405, 2005.

[63] A. Labarta, X. Batlle, and O. Iglesias. From finite size and surface effects to glassy behaviour in ferrimagnetic nanoparticles. *Surface Effects in Magnetic Nanoparticles*, pages 105–140, 2005.

[64] M. Basini, T. Orlando, P. Arosio, M. F. Casula, D. Espa, S. Murgia, C. Sangregorio, C. Innocenti, and A. Lascialfari. Local spin dynamics of iron oxide magnetic nanoparticles dispersed in different solvents with variable size and shape: A 1h nmr study. *The Journal of chemical physics*, 146(3):034703, 2017.

[65] T. Orlando, M. Albino, F. Orsini, C. Innocenti, M. Basini, P. Arosio, C. Sangregorio, M. Corti, and A. Lascialfari. On the magnetic anisotropy and nuclear relaxivity effects of co and ni doping in iron oxide nanoparticles. *Journal of Applied Physics*, 119(13):134301, 2016.

[66] L. D. Huber. Synthesis, properties, and applications of iron nanoparticles. *Small*, 1(5):482–501, 2005.

[67] H. Ittrich, K. Peldschus, N. Raabe, M. Kaul, and G. Adam. Superparamagnetic iron oxide nanoparticles in biomedicine: Applications and developments in diagnostics and therapy. *RoFo Fortschritte auf dem Gebiet der Rontgenstrahlen und der Bildgeb. Verfahren*, 185(12):1149–1166, 2013.

[68] H. Rui, R. Xing, Z. Xu, Y. Hou, S. Goo, and S. Sun. Synthesis, functionalization, and biomedical applications of multifunctional magnetic nanoparticles. *Advanced Materials*, 22(25):2729–2742, 2010.

[69] G. Baldi, D. Bonacchi, M. C. Franchini, D. Gentili, G. Lorenzi, A. Ricci, and C. Ravagli. Synthesis and coating of cobalt ferrite nanoparticles: A first step toward the obtainment of new magnetic nanocarriers. *Langmuir*, 23(7):4026–4028, 2007.

[70] E. Illes, M. Szekeres, E. Kupcsik, I. Y. Toth, K. Farkas, A. Jedlovszky-Hajdu, and E. Tombacz. Pegylation of surfaced magnetite core–shell nanoparticles for biomedical application. *Colloids and Surfaces A: Physicochemical and Engineering Aspects*, 460:429–440, 2014.

[71] E. Tombacz, M. Szekeres, A. Hajdu, I. Y. Toth, R. A. Bauer, D. Nesztor, and L. Vékas. Colloidal stability of carboxylated iron oxide nanomagnets for biomedical use. *Periodica Polytechnica. Chemical Engineering*, 58, 2014.

[72] A. P. Z. Stevenson, D. B. Bea, S. Civit, S. A. Contera, A. I. Cerveto, and S. Trigueros. Three strategies to stabilise nearly monodispersed silver nanoparticles in aqueous solution. *Nanoscale research letters*, 7(1):151, 2012.

[73] I. Römer, A. J. Gavin, T. A. White, R. C. Merrifield, J. K. Chipman, M. R. Viant, and J. R. Lead. The critical importance of defined media conditions in daphnia magna nanotoxicity studies. *Toxicology letters*, 223(1):103–108, 2013.

[74] Y. Hu, X. Jiang, Y. Ding, H. Ge, Y. Yuan, and C. Yang. Synthesis and characterization of chitosan–poly (acrylic acid) nanoparticles.

[75] N. K. Iversen, S. Frische, K. Thomsen, C. Laustsen, M. Pedersen, P. B. L. Hansen, P. Bie, J. Fresnais, J. F. Berret, E. Baatrup, et al. Superparamagnetic iron oxide polyacrylic acid coated γ-fe 2 o 3 nanoparticles do not affect kidney function but cause acute effect on the cardiovascular function in healthy mice. *Toxicology and applied pharmacology*, 266(2):276–288, 2013.

[76] J. Fresnais, M. Yan, J. Courtois, T. Bostelmann, A. Bee, and J. F. Berret. Poly (acrylic acid)-coated iron oxide nanoparticles: Quantitative evaluation of the coating properties and applications for the removal of a pollutant dye. *Journal of colloid and interface science*, 395:24–30, 2013.

[77] D. I. Khomskii. Orbital effects in manganites. *International Journal of Modern Physics B*, 15(19n20):2665–2681, 2001.

[78] A. J. Rondinone, C. Liu, and Z. J. Zhang. Determination of magnetic anisotropy distribution and anisotropy constant of manganese spinel ferrite nanoparticles. *The Journal of Physical Chemistry B*, 105(33):7967–7971, 2001.

[79] R. Valenzuela. *Magnetic ceramics*, volume 4. Cambridge University Press, 2005.

[80] D. Peddis, F. Orru, A. Ardu, C. Cannas, A. Musinu, and G. Piccaluga. Interparticle interactions and magnetic anisotropy in cobalt ferrite nanoparticles: influence of molecular coating. *Chemistry of Materials*, 24(6):1062–1071, 2012.

[81] J. A. De Toro, S. S. Lee, D. Salazar, J. L. Cheong, P. S. Normile, P. Muniz, J. M. Riveiro, M. Hillenkamp, F. Tournus, A. Tamion, et al. A nanoparticle replica of the spin-glass state. *Applied Physics Letters*, 102(18):183104, 2013.

[82] K. O'Grady and R. W. Chantrell. Remanence curves of fine particle system i: experimental studies. *Int. Work. Stud. Magn. Prop. Fine Part. Their Relev. to Mater. Sci.*, pages 93–102, 1991.

[83] E. P. Wohlfarth. Relations between different modes of acquisition of the remanent magnetization of ferromagnetic particles. *Journal of Applied Physics*, 29(3):595–596, 1958.

[84] P. E. Kelly, K. O'Grady, P. I. Mayo, and R. W. Chantrell. Switching mechanisms in cobalt-phosphorus thin films. *IEEE Transactions on Magnetics*, 25(5):3881–3883, 1989.

[85] S. Mørup, M. Fougt Hansen, and C. Frandsen. Magnetic interactions between nanoparticles. *Beilstein journal of nanotechnology*, 1(1):182–190, 2010.

[86] R. Grössinger. A critical examination of the law of approach to saturation. i. fit procedure. *physica status solidi (a)*, 66(2):665–674, 1981.

[87] R. Street and S. D. Brown. Magnetic viscosity, fluctuation fields, and activation energies. *Journal of Applied Physics*, 76(10):6386–6390, 1994.

[88] M. Kallumadil, M. Tada, T. Nakagawa, M. Abe, P. Southern, and Q. A. Pankhurst. Suitability of commercial colloids for magnetic hyperthermia. *Journal of Magnetism and Magnetic Materials*, 321(10):1509–1513, 2009.

[89] R. Hergt and S. Dutz. Magnetic particle hyperthermia—biophysical limitations of a visionary tumour therapy. *Journal of Magnetism and Magnetic Materials*, 311(1):187–192, 2007.